Numerical Prediction of Turbulent Non-Premixed Forced Ignition in Altitude Relight

by

Yihao Tang

A dissertation submitted in partial fulfillment
of the requirements for the degree of
Doctor of Philosophy
(Aerospace Engineering)
in The University of Michigan
2021

Doctoral Committee:

Professor Venkat Raman, Chair
Professor James F. Driscoll
Associate Professor Mirko Gamba
Professor Volker Sick

Yihao Tang
yhtang@umich.edu
ORCID iD: 0000-0003-3476-006X

"No man ever steps in the same river twice, for it is not the same river, and he is not the same man." - Heraclitus

ACKNOWLEDGEMENTS

I would like to express my sincerest thank to my advisor, Prof. Raman, for guiding my Ph.D. study throughout the years with not only rigorous requirements but also great patience, as well as the best platform and resources. After years of Ph.D. training, I may understand the probability of turbulent non-localized forced ignitions using realistic jet fuels, while I am not sure about the probability of someone flying over the Pacific and finding an ideal advisor for his/her research and career, which is why I greatly appreciate having worked in Prof. Raman's lab.

For the same reason, I would like to deeply thank my defense committee member Prof. Driscoll, Prof. Gamba, and Prof. Sick. Their insightful advising has significantly helped improve the quality of the thesis.

I greatly appreciate having all my lab mates accompanying my Ph.D. journey, from whom I can always learn and receive help. Heeseok, Chris, Romain, and Stephen kindly helped me pick up many basic research skills when I first got introduced to combustion simulation. Malik helped me get through numerous technical troubles and from him I better saw how to approach and resolve a research problem. I also greatly respect his upright and altruistic way of treating people and handling issues. Prof. Han is a model scholar to me in combustion research, while I regret being only a freshman when he was in our lab and missed the best opportunity for more in-depth discussions. Despite working on completely different projects, Takuma and I were constantly exchanging ideas, tricks, and info, and, of course, catching up on endless deadlines together (in parallel). Alex is my first collaborator where I am the

second author, who also provided me tons of valuable career advice when I approached graduation. Negin (Maryam) is the only lab mate whose research topic is too advanced for me to grasp, despite that she already tried her best to explain them to me. Supraj impressed me with his problem-solving skills and effectiveness, and meanwhile being mindful helps me save potential troubles more than one time. Shivam always gives me great insights in data-driven analysis during our collaboration, which is one of the best research experiencing as if he (and Malik) just made those data self-tell a research story while all I need is to send the data. Xudong impressed me with his modestness in listening to suggestions/opinions and willingness to learn and try new things. Despite working together for a relatively short time, I've also felt the passions from Caleb and Ral toward combustion research, and I believe all the newly joined lab mates will achieve in their field of study as well. I'd also thank Damien for being a bright lab mate.

I am fortunate to meet many talented collaborators and peers during my Ph.D. study. Brandon is the experimental collaborator of my thesis study, whose professionality and in-depth understandings of multidisciplinary physics appreciably shed into my thesis (I hope). I appreciate the chances of internship at Argonne National Lab offered by Riccardo and Sibendu, and all the friendly colleagues at ANL that made me feel belonged during my short stay. I would particularly thank Riccardo for his patient advisory and being thoughtful and approachable, Joohan for his limitless patience, professionality, and earnestness, and Brandon for the eye-opening tour at APS. For the project of flashback simulation, I greatly appreciate Rakesh Ranjan for always being responsive and patient in answering my trivial queries regarding his experiments. For the project of soot simulation, I would like to first thank Prof. Im for his advisory and then thank Junjun for being so hard-working, resilient, and efficient during our collaborations. Shaowu is my senior schoolmate since I'm an undergrad, who shows great research talent and has provided me many valuable suggestions dur-

ing my study, which I greatly appreciate. I would also thank Adel for co-working on the jet flame project, Prabhu for co-working on the soot project, and Yuan for progressive discussions. Thank my undergraduate mentor Prof. Gao, Prof. Jiang, and Prof. Lee for introducing me to the wonders of CFD.

This thesis is completed in an unsettling year of unexpected events, where my graduation paces have been greatly disrupted. For this, I would like to thank my colleagues at ANSYS for providing me a smooth transition to the industrial position during my graduation season. Especially, thank Shaoping and Genong for allowing me a very flexible schedule so that I can complete my thesis and defense in time, thank Chao, Steven (Yu), and Chenglong for their warm welcome, great hospitality, and career advice, thank Rakesh Yadav, Sibo, and Ashish for their help during the transition period. I am glad that I will still be working in the field related to combustion/reacting flow science - this is something I always enjoy doing.

I would like to thank my roommate Weihui, Renqi, and Bing for being kind and understanding. Thank all my friends in life.

Last, I would thank my parents for raising me, for their unconditional love, support, and understandings - these go beyond words.

TABLE OF CONTENTS

LIST OF FIGURES

Figure

LIST OF TABLES

Table

LIST OF APPENDICES

Appendix

ABSTRACT

Fast and reliable altitude relight performance is one of the end goals of aircraft engine design. Relight involves the use of an external heat source (a kernel, for instance), to ignite a cold mixture of fuel and air in a turbulent flow environment. Due to the variabilities in spark kernel formation, its transport in a turbulent flow environment, and the mixing and chemical reactions that are influenced by turbulent mixing, ignition is described statistically in terms of a probability of success. Currently, full-engine tests remain the most direct approach to evaluating relight probability at relevant conditions. However, this approach is expensive both in terms of time and monetary cost. Computational models that can accurate predict ignition processes in a statistical sense can vastly accelerate engine design, and significantly reduce cost. The objective of the dissertation is to develop a predictive computational framework that addresses this key need.

Forced ignition, due to the nature of turbulent flow, exhibits complex flame structure. To describe the combustion processes, a novel hybrid tabulation approach is formulated. This method combined a conventional flamelet-progress variable tabulation with a homogeneous reaction model to capture the spark transition from a homogeneous volumetric reaction process to a diffusion-controlled flame. Since the success of kernel ignition or failure has to be described statistically, a procedure for introducing uncertainties from spark discharge and the turbulent flow is developed. The resulting computational model involves an ensemble approach, where a large set of realizations of a detailed large eddy simulation (LES) based description of the flow along with the hybrid tabulation model is used to determine ignition probabilities

The proposed framework is thoroughly validated using a stratified forced ignition experiment designed to replicate high altitude relight. The model is found to successfully reproduce the fundamental physics, including the evolution of the spark kernel, and the entrainment of the fuel-air mixture into the hot kernel discharge. A particular experiment using methane as fuel is used to calibrate the spark discharge model, which is then used without modification in the study of alternative jet fuels. It is shown that the prediction framework capture the ignition probability for different fuels and operating conditions. This new computational framework provides the first rigorous approach to modeling high altitude relight.

CHAPTER I

Introduction

1.1 Motivation

The advancement of aircraft gas turbine engines is one of the important drivers of aerospace technologies. In general, the goal is to develop safer, more economical, and cleaner aircraft engines. More specifically, there are several key figures of merits (FOM) that are often interrogated during the design improvement of aircraft gas turbine engines. This includes altitude relight and lean blowout performances that are often used to evaluate operational safety, fuel efficiency and maintenance cost used to evaluate economy of use, and pollutant emissions (greenhouse gases, NOx, and soot) that the determine environmental footprint.

The focus of this thesis is the FOM of altitude relight, which is the forced ignition process of an aircraft gas turbine engine after it experiences a flameout at high altitude. Altitude relight is also a key FOM in the development of alternative jet fuels (AJFs), where the developed AJFs should be used as drop-in replacements of existing conventional jet fuels with minimum to no modifications in their operational capability. Currently, the design of aircraft engine/AJFs relies heavily on large-scale experiments to determine the engine relight characteristics under the tested conditions of combustor layout/fuel composition, which is resource-consuming and time-consuming. To develop numerical capabilities as alternative enabling tools

for predicting altitude relight has become more and more meaningful. As the recent advancement of computational technologies allows for the increase of simulation fidelity, such a goal has also become more reachable than ever. Motivated by these above, this thesis sets goals to numerically predict the fundamental problem of altitude relight - forced ignition. In specific, the target problem here features a turbulent non-premixed forced ignition using realistic jet fuels and an aircraft spark igniter. While focusing on the application of altitude relight, the thesis may also provide insights into other areas that involve forced ignition.

1.2 Problem Overview

While highly unlikely, aircraft gas turbine engines can experience a flameout during operation at high altitudes due to reasons including turbulent disturbances and ingestion of ice [1, 10, 11]. Under such a situation, the engine needs to be relighted within a certain time period. Since the combustor pressure and temperature drop during the engine flameout, the longer it takes to relight the engine, the higher risk of a complete relight failure. Therefore, a fast and reliable altitude relight is always the end goal of the design.

A typical altitude relight procedure goes as follows (Fig. 1.1): Firstly, the engine igniter turns on and creates an electric spark at a certain frequency. With every electric spark fired by the igniter, there is a chance that the spark successfully initiates chemical reactions of the fuel/air mixture that later develops into a stabilized combustion inside the engine. Secondly, the fuel flow is increased, sometimes with selective fuel injection techniques that direct the fuel spray biased towards the igniter location [3], so as to further increase the chances of ignition success; Then, within a specified time period ($5 - 10$ seconds), if the engine is successfully relighted, the relight procedure is ended and the engine resumes normal operation. Otherwise, the fuel flow needs to be cut off for a while allowing the "cleaning" of the engine before

repeating the entire relight procedure.

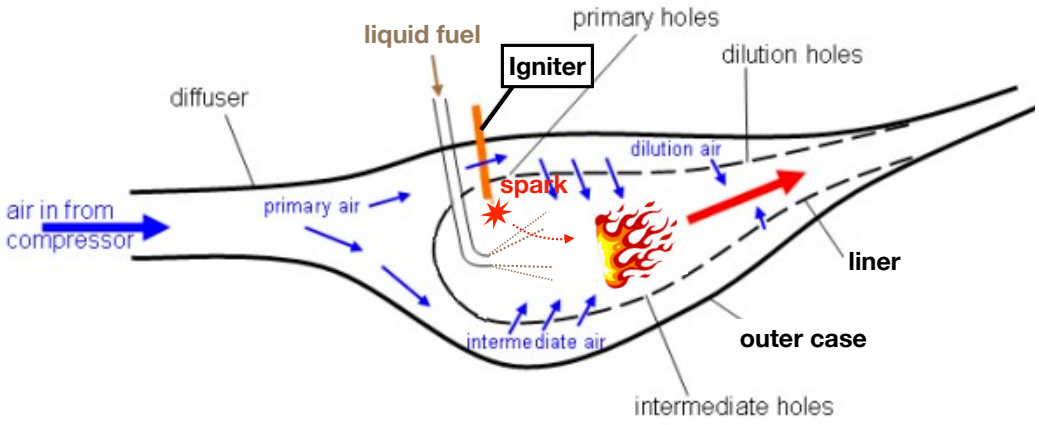

Figure 1.1: Diagram of altitude relight.

The fundamental physics of the altitude relight problem is the forced ignition of combustion following the aircraft igniter discharge. Unlike the forced ignition within a well-organized environment that is quiescent or laminar, the process here features a turbulent non-premixed forced ignition, where the turbulent strain and turbulent fuel-mixing greatly complicate the physics. Besides, the realistic effect of liquid fuel spray introduces another layer of complexity. In the following sections, several important components and concepts related to turbulent non-premixed forced ignition in altitude relight are introduced.

1.2.1 Aircraft Igniter

Modern gas turbine engines mostly apply electrical discharge as the ignition source [1]. The advantages of electrical discharge over other types of ignition sources (e.g. torch igniters [12, 13] or heating surface [14–16]) is its high efficiency of energy conversion which conveniently deposits a considerable amount of energy in a short amount of time [1]. The most widely applied spark igniter in aircraft engines is the surface discharge igniter [1, 17], which mainly consists of a central electrode and an outer

electrode, separated by an insulator. A semiconductor is further attached to the firing end of the insulator to facilitate the ionization of the spark gap. The surface discharged igniter can be categorized into two main types of designs, depending on whether the spark gap is flush or recessed, to be the flush fire igniter, or the sunken fire igniter (similar to the plasma jet igniter [18]). A configuration of the two types of surface discharge igniter is provided in Fig. 1.2. In general, the flush fire igniter converts energy more efficiently, has a longer operating life, but is also more difficult to manufacture, whereas the sunken fire igniter is vice versa [1].

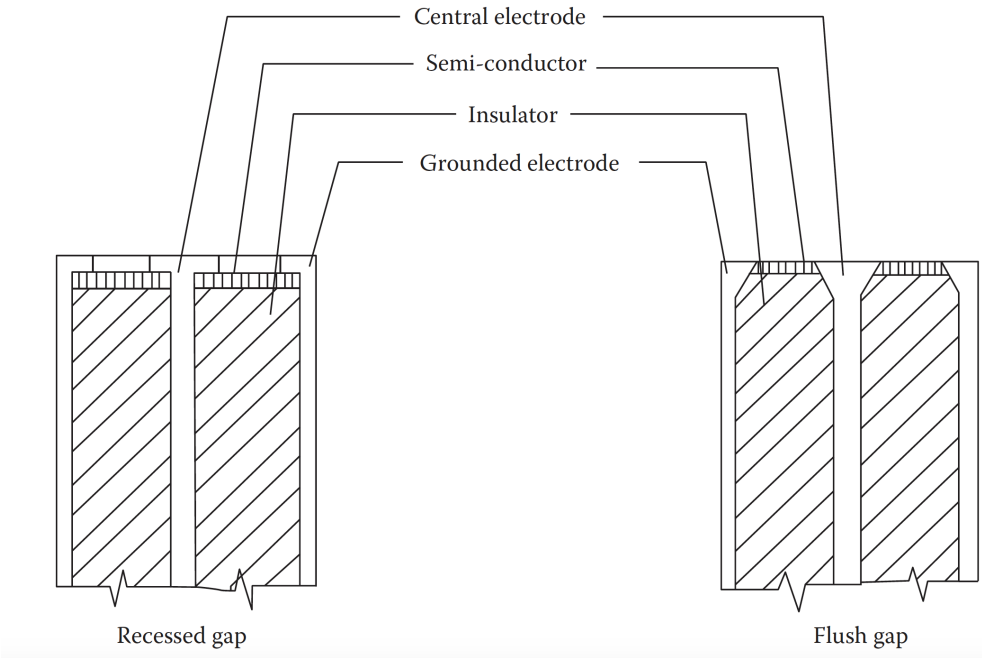

Figure 1.2: Configurations of the sunken fire igniter (left) and the flush fire igniter (right) [1].

The working mechanism of the surface discharged igniter goes as follows. At the beginning of each spark discharge, the voltage generation unit of the aircraft ignition system imposes increasingly high voltage (~ 2 kV) between the central electrode and outer electrode, until the gas near the spark gap is suddenly ionized and becomes conductive (electrical breakdown), producing a discharge in the form of an electric arc. A significant amount of electric energy is then converted into thermal energy

when the electric current runs through the gas field, concentrated near the electric arc. The discharge duration lasts for a very short amount of time ($\mathcal{O}(10^{-5})$ s) before the voltage between the electrodes drops and the ionized gas channel cannot sustain. Depending on the size of the aircraft engine, the corresponding igniter has a spark rate of $60 \sim 250$ sparks per minute and an energy release of $1 \sim 12$ J per discharge.

The main outcome of the spark igniter discharge is the creation of a hot spot in the gas field, here referred to as the "kernel", which is frequently used as the initial condition/starting point in forced ignition studies. Apart from the energy deposition, there are also other physical effects introduced by the spark discharge, such as a blast wave due to drastic density variation, and free radicals/ions due to thermal dissociation/ionization [19]. Each of these effects is featured by a different characteristic time scale and can be more or less important based on the particular configuration of the forced ignition problem. As a starting point, the studies in this thesis mainly consider the spark discharge as a pure energy source (unless otherwise mentioned), which is nonetheless widely applied in the forced ignition modeling community.

Before moving to the next section, one should note that while the aircraft igniter critically affects the forced ignition outcome, the design of the aircraft igniter cannot be made only to guarantee the success of ignitions (e.g., simply by increasing the igniter power). Most of the forced ignitions in an aircraft engine take the form of an engine ground start instead of an altitude relight, where the operating life of the igniter is important, which implies that the design must consider routine reliable operation. Therefore, just like any other design optimization problem, the aircraft igniter design takes a blended consideration of economics and performance. Throughout this thesis, it will be mentioned occasionally that certain difficulties or approach limitations exist for resolving the forced ignition problem, and many of those are related to the aircraft igniter design.

1.2.2 Forced Ignition Process in Altitude Relight

1.2.2.1 General information of forced ignition

To begin with, the concepts of forced ignition vs. autoignition is first introduced. Forced ignition is the ignition process with an external source of thermal energy or radical species. Autoignition is the ignition process that takes place spontaneously, and it happens when the fuel/oxidizer mixture is at a temperature above a threshold value referred to as the autoignition temperature. An interesting case that is worth a brief mention here is the homogeneous charge compression ignition (HCCI) that is widely applied in diesel engines [20]. In practice, the HCCI ignition is due to autoignition, as the fuel/air mixture spontaneously ignites as it reaches autoignition temperature due to compression. However, the thermal energy rise in the HCCI ignition does come from an external source, except that the source is not directly imposed locally to a certain region but instead globally in the form of compression work. In this regard, the HCCI ignition is similar to forced ignition. As will be explained later in Sec. 2.1.1.1, the ignition model developed in this thesis for turbulent non-premixed forced ignition is inspired by a model for HCCI ignition.

In a well-characterized configuration such as a quiescent condition or laminar flow, the forced ignition process is controlled by the competition between chemical heat release within the kernel and the rate of heat loss through the kernel surface. Essentially, as long as the initial kernel energy can sustain the heat loss for a sufficient amount of time before the chemical reactions start releasing energy, the ignition process will be successful. Based on experimental measurements [21–24], analytical modeling [22, 25], and reduced-order modeling [26], the ignition outcome can be predicted to a fairly accurate extent using only a few parameters such as the minimum ignition energy (MIE) [21, 22] of the kernel or the critical radius [25] of the spherical flame developed during the early stage kernel evolution.

In more realistic applications of industrial burners and aircraft combustors, there are more obstacles to overcome before reaching a successful forced ignition. The reaction should not only survive the kernel stage and transform into a propagating flame front but should also survive the flame quenching during flame propagation and reach flame stabilization within the combustor/aircraft engine. More specifically, the forced ignition process must go through the following three phases [2]: phase 1, generation of small flame around the kernel (referred to as the "flame kernel"); phase 2, the transition from the flame kernel into propagating flame; phase 3, long-term flame stabilization within the burner. For aircraft engines, an additional phase can be defined as phase 4, where the flame propagates to multiple combustors especialy in a can-annular arrangment [27]. Due to the complex flow environment in realistic applications, throughout the above processes, the reaction fronts evolve based on the complex interplay between heat dissipation, fuel entrainment/mixing, turbulent strain, and reaction kinetics. As a result, the ignition success/failure will not only be dependent on the initial kernel status but also the evolution history of the kernel trajectory and the later turbulent flame propagation, making it much more difficult to predict the ignition outcome.

1.2.2.2 Turbulent non-premixed forced ignition

For realistic combustors using turbulent non-premixed combustion, the concept of localized ignition vs. non-localized ignition is introduced here. The difference lies in whether the kernel starts reaction immediately at the spark location (localized ignition) or reacts later after it gets transported somewhere else (non-localized ignition). The physical mechanism behind such difference is related to flammability limits and fuel entrainment. As a demonstration, a schematic of the turbulent non-premixed forced ignition process for provided in Fig. 1.3. The figure is reproduced from Ref. [2], which originally only depicts the localized ignition. Here, both local-

ized and non-localized ignitions are plotted, with two kernels initialized at different locations that are inside/outside the regions enclosed by the iso-lines of flammability. Note that even if the kernel initialization is fixed to the same position, as in most applications, the flammability of the initial kernel can still vary between shots due to turbulent disturbances.

For the localized ignition, the ignition sequence (steps) in Fig. 1.3 exhibits a straightforward match-up to the three phases of forced ignition introduced in the last section for single burners (hence, no phase 4). Step 1 corresponds to phase 1, where a small spherical flame is immediately formed around the kernel at the location of the spark discharge. Step 2 corresponds to phase 2, where the flame kernel expands in the nature of a stratified flame, i.e., within the flammable range of equivalence ratio [28]. Step 3 corresponds to phase 3, where the flame propagates upstream following the iso-line of the stoichiometric equivalence ratio. Depending on the mixture fraction gradient, the flame front propagates in the nature of a premixed flame (3A), a triple-flame (3B) [29], and an edge flame (3C) [30], and eventually develops into a stable turbulent jet flame, attached to the nozzle or lifted.

For the non-localized ignition, however, since the kernel is initialized with a local composition outside flammability (usually lean), the kernel would need to first get transported to reach and entrain a flammable mixture before reaction. This step is labeled here as step 0 (kernel transport), prior to step 1 (reaction initiation), and step 0 & 1 should together constitute phase 1. The remaining steps are the same as those in a localized ignition.

In altitude relight, the non-local effect is often very prominent compared to other applications. This is due to the placement of the igniter relative to the fuel injector. Typically, the aircraft igniter is positioned outside of the primary zone, with its tip immersed ± 1 mm from the combustor liner [1], which barely clears the layer of cooling airflow through the sidewall (see Fig. 1.4). This placement design is partially

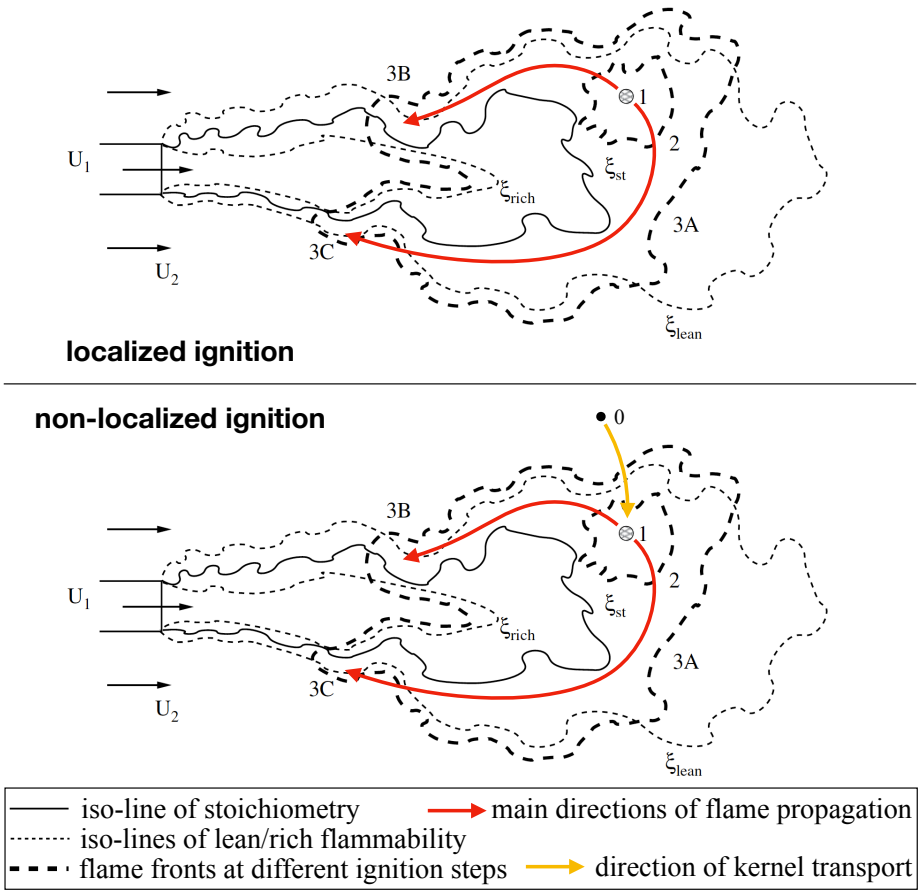

Figure 1.3: Schematic of localized ignition vs. non-localized ignition, reproduced from [2].

for maintenance accessibility purposes and partially for a longer operating life of the igniter. For instance, if the temperature of the igniter tips gets above 900 K, the operating life of the igniter will be reduced rapidly due to overheating of the semiconductor [31]. Therefore, the igniter tip cannot protrude too far into the combustor. In some cases, a film of cooling air is directed to flow over the igniter tip to prevent the overheating [1], where the resulting kernel composition becomes even leaner. Therefore, non-localized ignitions constitute a significant portion of the forced ignitions in altitude relight. However, this feature also poses a modeling challenge, since the transport of the kernel from the igniter to the primary fuel zone is affected by the intervening turbulent flow, which disrupts the otherwise direct relationship between

the initial kernel status and the ignition outcome. Here, an initial kernel status that promotes reaction may be quenched later due to strain, whereas one that prohibits reaction may later ignited due to sustained fuel entrainment. As will be discussed in Sec. 1.3.2.2, many existing forced ignition models based on the local properties of the kernel have difficulties in capturing non-localized ignitions.

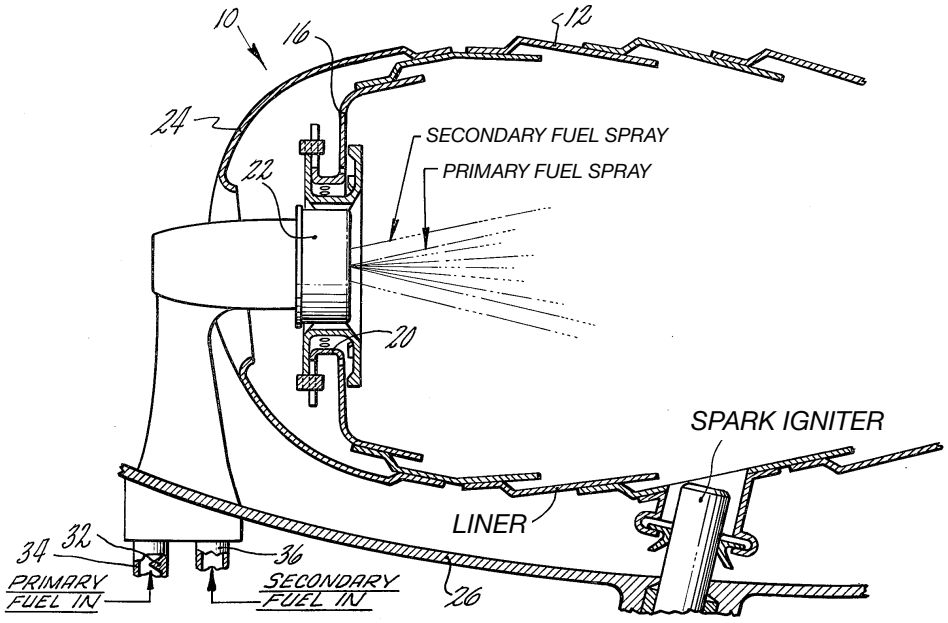

Figure 1.4: Igniter displacement in a typical annular combustor, obtained from [3].

1.2.3 Ignition Probability

Realistic forced ignition problems are chaotic in nature due to multiple factors. Here, the ignition outcome (success/failure) is extremely sensitive to small variations in the initial and boundary conditions and it is almost impossible to predict individual sparking events. The uncertainties associated with the problem are mainly two-fold. Firstly, the ignition process depends on the details of the spark discharge, such as the shape of the electric arc and the amount of energy deposited during the discharge varies between shots, which are chaotic and cannot be accurately predicted. Secondly,

the background turbulence will strongly affect the ignition outcome, which is also a chaotic process with uncertainties propagated from the initial status of the flow field and the domain boundaries. As a result, the ignition probability needs to be introduced to describe the forced ignition performances.

For aircraft engines, the industrial approaches often apply the flight envelope of safe altitude relight (Fig. 1.5), which is essentially the iso-line of a certain threshold success rate of altitude relight, and is obtained by performing large-scale rig tests or even full-scale engine tests [32]. The success rate of the altitude relight can also be evaluated as the probability of ignition success produced by a series of forced ignition trails. For a total number of N_{Spk} spark discharges, this probability is evaluated as

$$P_{Relight} = 1 - (1 - P_I)^{N_{Spk}}, \tag{1.1}$$

assuming that each forced ignition processes followed by the spark discharge is statistically independent. In academic studies, the main goal is often to measure/predict the ignition probability of an individual forced ignition sequence, denoted in this thesis as P_I.

1.2.4 Liquid Fuel Spray

In aircraft engines, fuel is injection in the form of liquid droplets. Essentially, as the fuel would need to first transfer from the liquid phase into the gas phase before reaction, the forced ignition of a fuel mist faces the extra rate-limiting factor of fuel evaporation compared to that of a fully evaporated mixture. The local fuel evaporation rate, however, is dependent on multiple factors including vapor fraction, fuel volatility, and droplet size distribution. The size distribution, resulting from the breakup of a spray jet, is dependent on the atomization techniques, turbulence and the physical properties of the liquid fuel such as viscosity and surface tension. Overall,

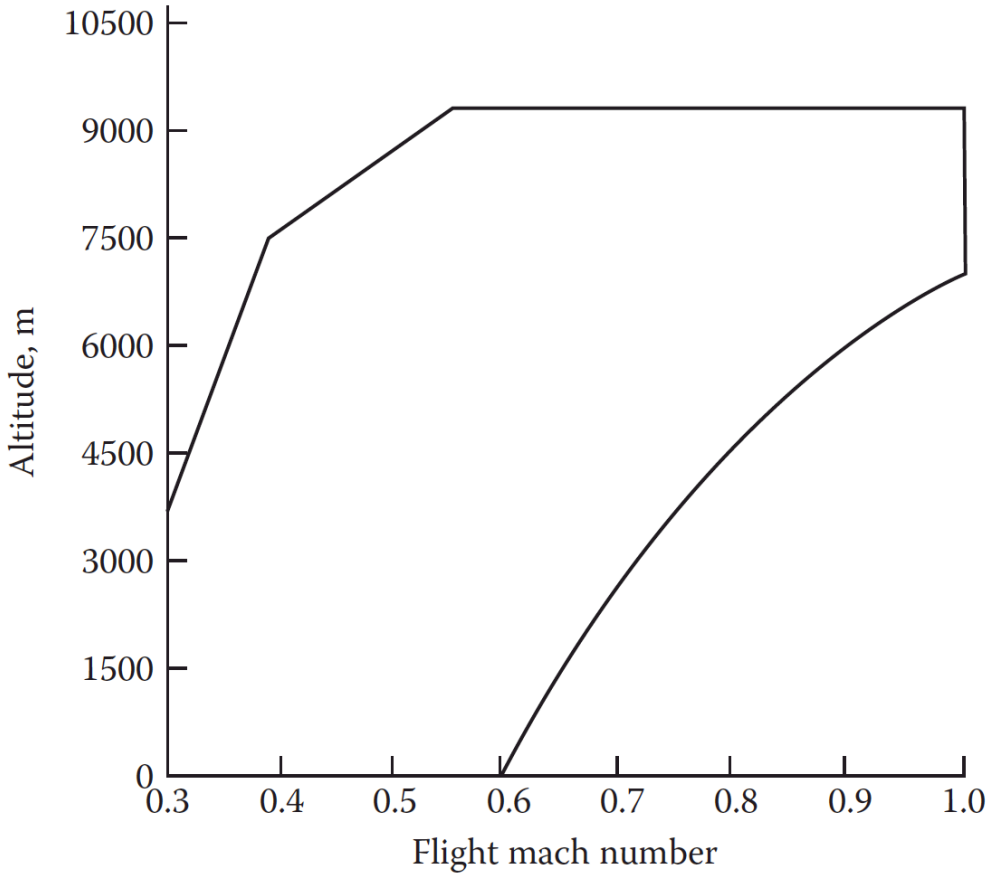

Figure 1.5: Flight envelope of safe altitude relight of a conventional annular combustor, obtained from [1].

the liquid fuel spray introduces an extra set of physical processes in the already complex forced ignition problem. As a result, the dominating physical mechanism and the forced ignition behavior can be vastly different from gas phase combustion. For instance, in a recent research campaign that focuses on developing AJFs [33], it is shown that the dominating factors that affect the ignition performances of the liquid spray combustion are often the density, surface tension, and viscosity of the fuel [34], whereas those in gas-phase combustion are found to be the chemical properties of the fuel [35]. Experimental data also show that ignition behavior variation with operating conditions can be starkly different between gaseous and multiphase combustion [36]. This brief introduction is provided only to note the differences between liquid and

gaseous fuel based forced ignition. The focus of this thesis is on the latter, for which existing literature is reviewed first.

1.3 Literature Review

Due to the breadth of this topic, the review here is mainly focused on turbulent non-premixed forced ignition, aircraft spark igniter, gas-phase combustion, and numerical studies. In particular, the numerical modeling approaches are discussed. A comprehensive review of the turbulent non-premixed forced ignition problem is provided by in [2], which forms the basis for this analysis.

1.3.1 Experimental Studies

Due to the relevance for internal combustion (IC) engines, premixed forced ignition has been extensively studied [37–40]. However, such studies are often conducted in a quiescent environment [41, 42]. The MIE-type theory (Sec. 1.2.2.1) has been successfully applied to explain the governing mechanism of the forced ignition process. Apart from MIE models based on a spherical kernel governed by diffusive processes, there are other empirical models that incorporate the entrainment and vortex dynamics of the kernel [43, 44], which have been validated against experimental observations [45].

Compared to premixed forced ignition, non-premixed ignition has been less extensively studied, especially for turbulent combustion. Ahmed and Mastorakos [46] studied the spark ignition sequence of a lifted turbulent non-premixed jet flame, focusing on the growth rate of the initial flame kernel (flow pocket of high concentration of reaction product) and the follow-up edge flame propagation. To understand the ignition probability of turbulent non-premixed forced ignition, the pioneering studies of Birch *et al.* [47] and Smith *et al.* [48] measured the ignition probability of a turbulent non-premixed jet flame at different sparking locations, and introduced the flammability factor as an estimation of the probability of establishing a stable flame

at a certain sparking location. The flammability factor is calculated as the probability of having a mixture fraction that is in between the lean and rich flammability limits, i.e.,

$$F = \int_{Z_{lean}}^{Z_{rich}} f(Z)\, dZ. \tag{1.2}$$

Equation 1.2 is formulated at a local point within the physical domain, with F being the flammability factor and f being the probability density function (PDF) of the mixture fraction Z.

More recently, Ahmed and Mastorakos [49] carried out a similar experiment to measure the ignition probability and evaluated its relationship between the flammability factor. They found that the ignition outcome is not necessarily monotonic to the local equivalence ratio being inside/outside the flammability limits. The reason behind this phenomenon is mainly due to turbulent quenching and non-localized ignition as introduced in Sec. 1.2.2.2.

While those previous experiments have addressed the issue of non-localized ignition in turbulent non-premixed forced ignition, a systematic experimental study that provides control over the mixture fraction or the duration between spark kernel creation and the interaction of the spark kernel with a flammable mixture has not become available until the recent thesis study by Sforzo [5], where a facility is designed for this particular purpose. In this configuration, the spark discharge is initialized within a non-reactive flow before the hot kernel later mixes with flammable fluid, making it possible to control the kernel transport process in the non-localized ignition. The facility not only closely replicates the ignition process of aircraft engines altitude relight, but also provide abundant measurements of the ignition probabilities of multiple jet fuels, as well as other important properties such as the area growth of the flame kernel [6, 50]. While the main experiment was performed for gas-phase combustion, companion studies using liquid fuel spray have also become available [36, 51].

In this thesis, this facility is chosen as the main target configuration.

1.3.2 Numerical Studies

The focus of this thesis is in the use of large eddy simulation (LES) for modeling ignition. It is now well-established that LES is better suited for modeling turbulent combustion than Reynolds-averaged Navier–Stokes (RANS) simulations [52, 53]. The main reason is the ability to capture unsteady effects of turbulence on the combustion process more accurately. The discussion below only summarizes LES-based modeling of ignition.

Similar to the experimental studies, simulations of the forced ignition process in premixed combustion are also largely focused on IC engines, where multiple premixed combustion models are already available to track the flame propagation, including the time scale model [54], the flame surface density (FSD) model [55], and the level set/G-equation combustion model [56]. The remaining problem is to model the initial transition from a kernel (high-energy fluid pocket) into a spatially distributed flame front. In many cases, this transition is triggered until the small flame around the kernel can expand and reach a certain size [56], which could be the critical radius (introduced in Sec. 1.2.2.1). The growth of the kernel is further tracked by Lagrangian particles transported by an effective kernel growth velocity calculated as a function of properties of the spark discharge and the premixed combustion (e.g., spark energy and turbulent flame speed) [57], where the Lagrangian particles are used to overcome the lack of grid resolution relative to the initial kernel size. Once the transition is triggered, the flame propagation model is enabled by initializing the flow field with imposed flame surfaces.

Based on the research objective and methodology, previous numerical studies of turbulent non-premixed forced ignition mainly fall into two categories. Category 1 is to investigate flame extinction and stabilization process after the kernel has successful

transit into a propagating flame, i.e., phase 3 and phase 4 of a realistic forced ignition process (introduced in Sec. 1.2.2.1), and is usually performed by analyzing individual time sequence of the flame evolution obtained from the simulated ignition events [27, 58–63]. Category 2, conversely, is to investigate the overall statistical behavior of the ignition, i.e., the ignition probability, and the analysis is usually based on the ensemble results from multiple simulated ignition events [4, 64, 65]. Often, vastly different modeling methods are applied in the two categories of studies, as summarized in the two following subsections.

1.3.2.1 Methods for flame propagation and stabilization study

For Category 1 studies, high fidelity reacting flow simulations are mostly used, since the computational cost is affordable to perform a single simulation. Moreover, since the study focus is on the later stage flame propagation instead of the initial evolution of the kernel, there is no extra modeling requirement to include the underlying physics of forced ignition. In many cases, existing turbulent combustion models are directly applied to the forced ignition simulations with imposed initial condition method (i.e., flow field patching). For instance, Triantafyllidis *et al.* [58] used a conditional moment closure (CMC) approach to study the ignition of a bluff-body flame, with the kernel initialized as a pocket of the reaction product of the 1-D flamelet. Subramanian *et al.* [59] and Pillai [60] have applied energy deposition (ED) to represent the kernel. The initial evolution of the kernel is tracked by monitoring the local gas-phase temperature, and when the local post-ED temperature drops to the level of chemical equilibrium, and the reaction is then initiated by patching the flow field with chemical equilibrium conditions. The advantage of the imposed initial condition approach is its simplicity. However, the disadvantage is the strong modeling assumption of an already-existed flame front, which holds for the studies of Category 1, but not for studies of Category 2 as will be soon discussed, and, especially, not for

non-localized ignitions. Apart from applying field initialization to existing turbulent combustion models, directly solving for the finite-rate chemistry and applying ED to represent the kernel is another commonly applied modeling approach. The advantage of finite rate chemistry is the inclusion of fundamental reaction kinetics without relying on the modeling assumptions of any canonical flows (e.g., the flamelet-based model), and is, therefore, applicable to general combustion problems (e.g., auto ignition, forced ignition, and flame propagation) regardless of the governing physics. The disadvantage, however, is the potential high computational cost of finite chemistry when detailed modeling of chemical reactions is required. As a result, previous forced ignition simulations with finite rate chemistry are mostly limited to simple fuels with global reactions [61, 62, 66], where the ignition process can be adequately captured by the simplified chemical mechanism or by using detailed chemistry mechanisms but limited to simple configurations [63]. For forced ignitions in altitude relight, however, due to the complicated heat release process of the realistic jet fuels and the scale of the flow domain, finite rate chemistry has difficulties in balancing between modeling fidelity and computational cost.

1.3.2.2 Methods for ignition probability study

For Category 2 studies, most numerical predictions of ignition probability are based on cold flow simulations due to the prohibiting computational cost of simulating a large number of flow realizations. There are mainly two types of such cold-flow-based ignition probability models. One is by using the local flow properties, here referred to as the "local flow property models", and the other is based on flame propagation tracking, here referred to as the "flame particle models". The local flow property models assume the forced ignition success or failure depends entirely on the cold flow properties at the spark discharge location. For instance, Lacaze *et al.* [67] estimated ignition probability based on the local flow statistics provided by a cold

flow LES simulation, where the ignition outcome is modelled as a function of local flow statistics taking into the account of flammability and turbulent stretching. A similar method has been applied to study the ignition of two-phase flow by Eyssartier *et al.* [68]. The flame particle models [69], however, define the forced ignition to be successful until a certain portion of the domain is light up by the flame propagation and track the propagation using mass-less Lagrangian particles referred to as the "flame particles". This method is explained in more detail below as it is widely used in previous studies [4, 64, 69–72].

A schematic of the general flame particle models is provided in Fig. 1.6. In prior to the main simulation, a cold flow LES is performed to provide information on the turbulent velocity field. During the main simulations, a mesh that is much coarser than the cold-flow LES simulation is applied, where the flame particles are released from the cells that present the initial position and shape of the kernel. The flame particles then move according to a stochastic model using the statistics of the cold flow velocity as inputs. As the particles move and traverse to new cells, they can ignite a cell that was initially cold and release a new particle (to mimic the flame propagation). A particle can also be quenched and taken out of the simulation if the cold flow statistics of the new cell prohibit combustion, measured by a quench criterion (for instance, the local Karlovitz number being above a critical value). The simulation is repeated multiple times to obtain the ignition probability. The final ignition outcome determined is based on the ratio of the total number of cells that is ignited by the particles to the total number of cells in the domain.

As the flame particle models apply weaker modeling assumptions than the local flow property models while maintaining a relatively low computational cost, they have been extensively used to estimate ignition probability [4, 64, 69] with multiple variations now available [70–72]. However, ensuring computational feasibility requires a suite of assumptions, especially about the interaction of a hot kernel with the sur-

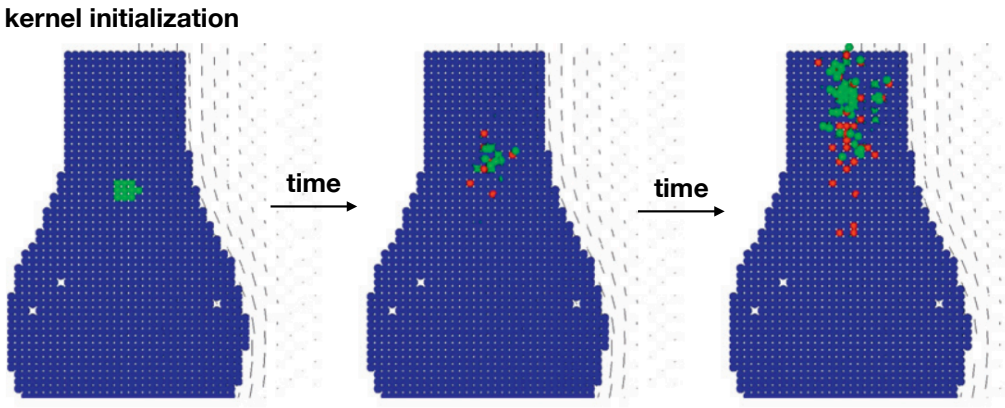

Figure 1.6: Schematic of the flame particle models, reproduced from [4]. The blue dots indicates grid cells, green dots indicates flame particles that are active, and red dots indicates flame particles that are quenched.

rounding flow field, which prevents such models from being directly compared to reacting-flow experiments. Moreover, the fluid particle models often do not include the notion of non-localized ignition. Here, the models tend to predict a failed ignition as the flame particles will be taken out at the moment of their release by the quench criterion (e.g., local Karlovitz number goes to infinity when the flame speed is measured outside flammability). While such difficulties can be partially overcome by providing the flame particles with a thermal memory [55], this introduces additional modeling components along with the corresponding modeling assumptions and complexities. Another common issue with flame particle models is the lack of inclusion of the uncertainties associated with the spark discharge. By releasing flame particles from the initial kernel location to track the reaction propagation, the model essentially assumes a propagating flame front has been formed immediately following the spark discharge, and the only uncertainty that can lead to a failed ignition is for the flame front to be later quenched during its propagation. This is not necessarily true, as a "weaker" spark discharge is more likely to generate an insufficient amount of propagating flame area, if any (non-localized ignition), during its early post-discharge

evolution and therefore more likely to lead to a failed ignition. Often, it is unclear how previous studies of flame particle models address this issue. An exception is the thesis study of Esclapez [70], which applies a continuous field variable to describe the initial size and the probability of the presence of the kernel (instead of directly using the flame particles). Nonetheless, the evolution of such field variable is based on macroscopic properties of the cold flow turbulence (i.e, turbulent dissipation rate) and is less likely to accurately capture the complex fuel entrainment in a non-localized ignition.

Fully reacting flow simulations are relatively sparse, with the study by Esclapez *et al.* [65] being the exception. While the estimation is based on a few numbers of simulation realizations and lacks a rigorous comparison with experimental data in terms of presenting the statistical uncertainties, this study has shown promising accuracy for capturing the ignition probability. This demonstrates the usefulness of using high-fidelity hot-flow simulations to provide a numerical estimation of ignition probability. However, there are still many modeling challenges to overcome before such numerical capabilities are ready to use, as will be discussed in Chapter. II.

Lastly, apart from cold-flow and hot-flow LES studies, there are other numerical efforts that predict forced ignition based on reduced-dimension modeling [73] and semi-empirical relations [74] that are also worth noting.

1.4 Scope of the Thesis

Given the limitations of existing numerical capabilities in predicting turbulent non-premixed forced ignition in altitude relight, the goal of this thesis is to develop a computational framework that enables such predictions. In specific, the thesis will try to achieve the following goals.

- Focusing on gas-phase combustion, develop a computational framework for

predicting the turbulent non-premixed forced ignitions in altitude relight, which enables

  - high fidelity and computationally efficient LES simulations of the forced ignition problems;
  - estimation of ignition probability based on LES simulation results.

- Provide rigorous validation of the developed computational framework for predicting turbulent non-premixed forced ignition.
- Demonstrate the use of the developed framework for identifying important physics in a target forced ignition problem.

The thesis is organized as follows:

Chapter II: The developed computational framework for predicting turbulent non-premixed forced ignition in altitude relight is introduced. The modeling theory of the combustion model is first introduced, along with its incorporation into the LES simulation platform and other technical details. The modeling procedure for ignition probability estimation is then discussed.

Chapter III: This section provides a validation of the developed computational framework. The target configuration is introduced first, and the comparison studies between the numerical simulations and experiments are then carried out.

Chapter IV: Two supplemental studies are carried out. The first is a demonstration study that uses the developed computational framework to understand key mechanisms in the target forced ignition problems. The second study is to evaluate the performance of existing numerical capabilities in providing a forward prediction of the sunken fire igniter discharge by simulating the gas expansion process immediately following the high-energy spark discharge.

Chapter V: A summary of this thesis is provided along with suggestions for future work.

CHAPTER II

Computational Framework

This chapter describes the computational model developed to predict forced ignition. This framework provides two main capabilities. One is the reacting flow LES simulation of the turbulent non-premixed forced ignition problem. This is a forward modeling that provides a deterministic ignition outcome given certain simulation inputs (e.g., spark deposit energy and initial background turbulence). The other is the comprehensive method of ignition probability predictions. This is a Monte-Carlo-based modeling procedure that propagates the uncertainties associated with the forced ignition problem from the hot-flow simulation inputs into the simulation results, and then reconstructs the ignition probability from the ensemble of results.

2.1 Forced Ignition LES Simulation Platform

The developed LES simulation platform consists of three main components, (a) a tabulated detailed chemistry model that includes the fundamental physics of forced ignition, (b) an LES solver that incorporates the turbulent combustion model and enables the simulation of flame development from a kernel; (c) coupling between the kernel and the turbulent flow.

2.1.1 Tabulated Detailed Chemistry Model

One of the modeling challenges for the turbulent non-premixed forced ignition problem here is balancing between fidelity and computational cost. One the one hand, the inclusion of detailed reaction is required for the application of realistic jet fuels. One the other hand, the computational cost must maintain a similar level as cold flow LES simulations to be applicable for ignition probability estimation. In this regard, the tabulated detailed chemistry model is the ideal modeling option.

A schematic of the ignition process along with the corresponding modeling strategy of the tabulated detailed chemistry model is summarized in Fig. 2.1. The turbulent non-premixed forced ignition in altitude relight is modeled as a process that goes through two main stages, each one corresponding to a different physical process. The model describes the initial kernel mixing and ignition as a homogeneous reaction process where chemical reactions alone dominate the thermodynamic state (stage 1), while the flame development and stabilization as a diffusion-controlled process where flow and chemical timescales interact, denoted (stage 2). As can be seen, this two-stage definition is a physics-based simplification of the localized/non-localized ignition steps summarized in Sec. 1.2.2.2. Specifically, step 0-1 is governed by a quasi-homogeneous reaction (stage 1), step 3-4 are governed by diffusion-reaction balance (stage 2), whereas step 2 is in the intermediate reaction mode between stage 1 and 2. The model developed here uses a tabulated detailed chemistry approach, constructed by blending solutions from different canonical combustion configurations that best represent each one of the two stages. Two types of canonical solutions are applied to construct the look-up table: (a) a constant pressure homogeneous reaction (HR) for stage 1; (b) a flamelet progress variable approach (FPVA) for stage 2. An additional type (c) is introduced as the blend between (a) and (b). As a result, the model should in theory be capable of capturing the entire physical process of the turbulent non-premixed forced ignition problem, along with the effects of non-localized ignition

and strain quenching.

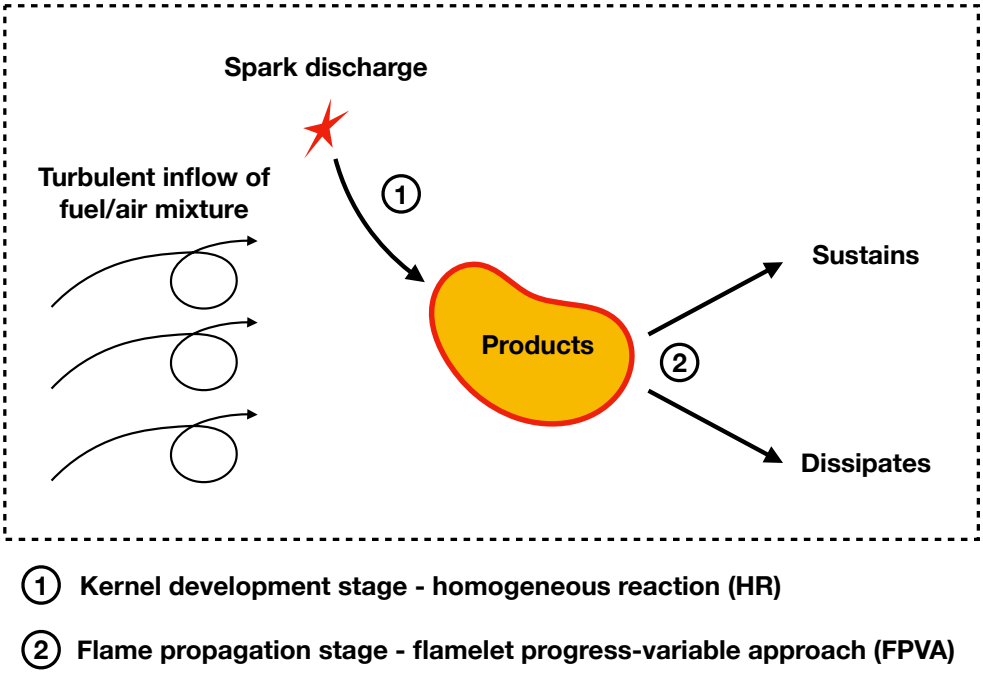

Figure 2.1: Schematic of forced ignition in an aircraft engine and the proposed model decomposition.

Since the total enthalpy of a representative kernel monotonically decreases due to mixing and diffusion, the total enthalpy H can be applied as a good marker to track the ignition process. As the flow evolves, the switch from HR to FPVA must occur when the total enthalpy H drops below a certain threshold (explained in the following sections). Therefore, the chemistry is tabulated as a function of H. To track the fuel–air mixing and the advancement of the reaction in the HR and FPVA model, the chemistry is also tabulated with respect to mixture fraction Z and progress variable C. Here, C is defined as the linear combination of the mass fraction of major species of the combustion product (i.e., H_2O, CO_2, CO, and H_2) and Z applies the definition of Bilger [75].

The two tabulation strategies (HR and FPVA) cover different phase space regions of the look-up table. In specific, HR is used for the high enthalpy space and FPVA for

the low enthalpy space. Further, an overlap region is tabulated as a weighted average of the two individual maps. When the tabulation is implemented in simulations, a kernel is initialized as a pocket hot fluid, which falls into the HR tabulation region in the tabulation phase space. If the local flow properties described by $\{Z, H\}$ are favorable to ignition, the high chemical source from the HR tabulation allows C to increase and initiate the reaction. As the flow field evolves, the kernel entrains the cold outerflow and eventually dissipates out, and the corresponding phase space positions (i.e., composition space positions) shift toward lower enthalpy regions and eventually fall into the FPVA tabulation region. Hence, flame propagation or dissipation is automatically captured. The HR and FPVA tabulation strategies are explained in detail in the following two subsections.

2.1.1.1 HR Tabulation

The HR tabulation is inspired by the study of Pera *et al.* [76], which uses a tabulation model built from HR for HCCI ignition. As has been discussed in Sec. 1.2.2.1, the ignition process there is driven by compression-based energy rise that brings the mixture temperature to be above the autoignition temperature. Inspired by this idea, here, the modeling strategy treats the forced ignition process locally as a homogeneous reaction caused by energy increase due to the spark source. The fundamental idea here is to assume the local reaction time scale in a forced ignition event is much smaller than the transport time scales, so that the ignition core can be treated as reaction-dominant. Stratification effects can also be included in the tabulation by combining different HR solutions for a range of equivalence ratios and unburnt temperatures. Specifically, each HR solution provides information of reaction process versus time which can be mapped on the C space at a constant $\{Z, H\}$; a series of HR solutions at different Z values provides information of stratification effects on reaction, and HR solutions with different unburnt temperatures allow a mapping in

the total enthalpy space H. The entire set of HR solutions can then be tabulated as a function of $\{C, Z, H\}$.

The HR calculations are performed using the open-source solver CANTERA [77]. The time history of species was stored for each HR calculation. To keep a smooth ignition trajectory in time and progress variable phase space, the HR solutions are stored whenever one of the following three criteria is met: (a) the temperature increment exceeds a certain value last output (in this thesis, 5 K); (b) the progress variable percentage increment exceeds a certain percentage since last output (in this thesis, 5%); (c) the time increment exceeds certain value since last output (in this thesis, 1 s). The HR calculation is terminated after it can be safely considered that the time exceeds the largest possible flow time scale (in this thesis, 7.5 s). A total number of about 3500 HR calculations were performed for about 100 levels of initial temperatures in the range of about 1000 K to 3000 K, and about 40 levels of equivalence ratios spanning within the flammability limits clustered near stoichiometric condition. The exact values of the enforced boundaries of the HR operating conditions are determined by the following criteria: (a) outside the lower temperature limit (i.e, autoignition temperature T_a), or the fuel-lean/rich limit, ignition delay will be longer than the largest flow time scales; (b) outside the upper-temperature limit, the burnt temperature will breach the upper bound of the thermodynamic model (e.g., the upper limit of the NASA polynomial fitting of enthalpy-temperature relation).

While the HR solutions contain all the necessary information on the ignition history profiles, the tabulation of these values for use in the CFD solution can lead to some numerical issues. In the CFD approach, a transport equation is solved for the three variables used to map the solution space (H, Z, and C). Of these, the progress variable equation contains a chemical source term, which is obtained from the table.

The exact integrated progress variable source term is defined as

$$S_C = \frac{1}{\Delta t_{Sim}} \int_{t=t_0}^{t=t_0+\Delta t_{Sim}} \dot{\omega}_C \, dt, \tag{2.1}$$

where $\dot{\omega}_C$ is the instantaneous progress variable source term, t_0 is the start time of the current CFD time iteration, and Δt_{Sim} is the CFD simulation timestep. In conventional tabulations, the integrated source term (denoted as $S_{C,t}$) is often obtained by assuming a constant progress variable source term over a timestep [78], as:

$$S_{C,t} = \overline{\dot{\omega}_C}(t = t_0 + \Delta t_{Sim}/2) \tag{2.2}$$

where $\overline{\dot{\omega}_C}$ is the progress variable source term that is interpolated from the discrete tabulation points on the table. This is based on the mid-point rule for integration and is accurate in conventional simulations to capture flame propagation, as long as the time-step is not large. However, for the purpose here, this approach may be erroneous. In the above formulation, two levels of approximation are made: (a) the reaction source term is assumed constant over the timestep and (b) the reaction source term is interpolated to $C(t = \Delta t_{Sim}/2)$ since it is only tabulated at discrete values of C. Since the ignition delay is of primary importance here, it is crucial to correctly capture the early stages of the HR calculation (say between $C = 0$ and $C = 0.01$). There, the chemical source term is low enough such that approximating the source term constant over the simulation timestep (dictated by the flow) is reasonable. However, the source term interpolation can introduce an error that is large compared to the instantaneous value of the progress variable source. Moreover, because the progress variable source term follows a convex profile with respect to the progress variable during the onset of ignition, and the resulting interpolation error always overestimates the integrated source term S_C. This is illustrated in Fig. 2.2, where the simulation time step Δt_{Sim}

is small compared to the interval between two HR tabulation points (black dots), and the overestimation of interpolated reaction source (red dash arrow) is contributed from the higher reaction source at the next tabulation point (yellow dash arrow). This issue can be resolved by sufficiently refining the table, but this could become quickly intractable in terms of memory requirements.

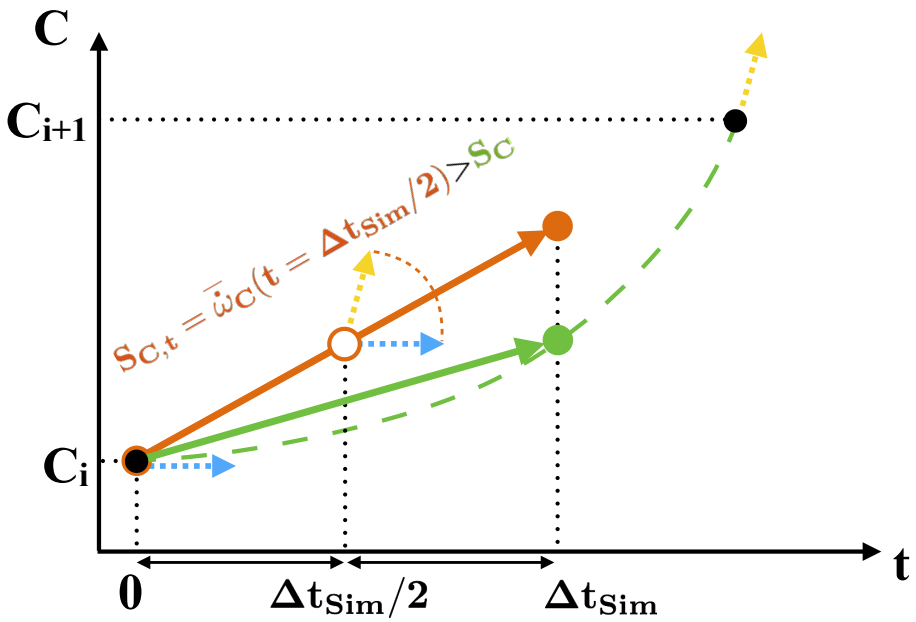

Figure 2.2: Demonstration of interpolation error in conventional tabulation strategy during ignition. The time history profile (green dash line) and the tabulation C-axis (black dots) are created artificially for demonstration purposes. The integrated reaction source $S_{C,t}$ is indicated by the slope of the red slid line whereas the exact reaction source is indicated by the slope of the green solid line. t_0 is set to 0.

A different tabulation/table look-up strategy is developed to resolve this issue. Here, the progress variable source term is no longer directly tabulated but instead reconstructed on-the-fly. The time information of the HR solution is tabulated, which serves as a target ignition time history profile, and the reaction source is reconstructed based on this tabulated time information. The purpose here is to avoid the interpolation error mentioned above, and, obtain from the tabulation, the progress variable

source term integrated over the simulation timestep. This can be achieved by taking the advantage that, under the HR modeling assumption, the linearization of the chemical source in the CFD partial differential equation (PDE) is equivalent to the chemical integration of the HR ordinary differential equations (ODE). In specific, the reconstructed reaction source (denoted as $S_{C,r}$) is written as

$$S_{C,r}(C(t_0), \Delta t_{Sim}) = \frac{C_{target} - C(t_0)}{\Delta t_{Sim}}, \tag{2.3}$$

where $S_{C,r}$ depends on the initial progress variable $C(t_0)$, the current simulation step size Δt_{Sim} and C_{target}, which is the theoretical final value of progress variable. Here, this theoretical value should be on the time history profile of the progress variable along the HR profile (denoted as C_{HR}). As $C(t_0)$ and Δt_{Sim} are already available at the current time step, the goal is to find $C_{target} = C_{HR}(t_0 + \Delta t_{Sim})$.

The following numerical procedure is applied to obtain C_{target} (illustrated in Fig. 2.3): the time history of the original HR solution is referred to as $t_{HR} = t_{HR}(C)$, or conversely $C_{HR} = C_{HR}(t)$. All tabulated properties are labeled by subscript "Tab", and their value at the i-th point of C-axis of the table is labeled by subscript i. At the tabulation stage, $t_{HR}(C)$ (green line) is first mapped onto the table C-axis, and is discretized in the table as $t_{HR,Tab}(C)$ (black line marked by dots). The time interval between two consecutive points of the tabulated HR time history is then stored at the former point, as $\Delta t_{HR,Tab}(C_i) = t_{HR,Tab}(C_{i+1}) - t_{HR,Tab}(C_i)$; at the table look-up stage, C_{target} is determined inversely from the equation

$$\Delta t_{Sim} = \sum_{C_i = C(t_0)}^{C_{target}} \Delta t_{HR,Tab}(C_i). \tag{2.4}$$

Note that C_{target} is the upper limit of the above summation, and the equality can be tested by incrementally adding the term $\Delta t_{HR,Tab}(C_i)$ into the summation until the desired value of C_{target} is found. Therefore, the numerical implementation of the

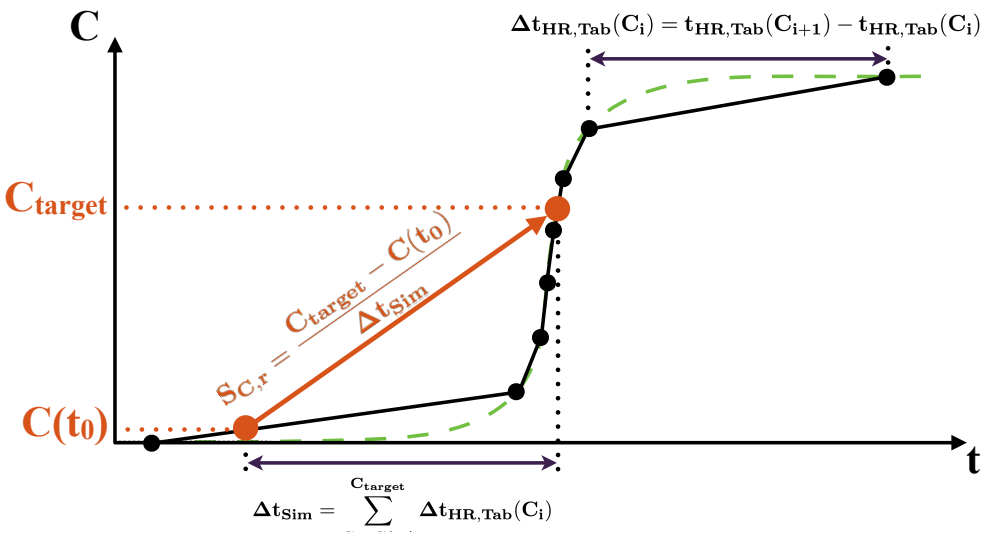

Figure 2.3: Tabulation and look-up strategy of $S_{C,r}$. The time history profile and the tabulation C-axis are created artificially for demonstration purposes.

above procedure is about the same time complexity as finding the reference points adjacent to $\overline{C}(t_0 + \Delta t_{Sim}/2)$ and interpolating the looked-up value (i.e., conventional source term look-up strategy of Eq. 2.2).

The performance of this tabulation/table look-up strategy of reaction source is tested using homogeneous reaction simulation. Three different types of simulations are carried out: (a) ignition profile is obtained using the tabulated source term and considering it constant over each timestep, (b) integration is performed using the aforementioned strategy that uses the modified tabulation approach, and (c) integration is performed without tabulation but instead by directly integrating ODE obtained from the chemical mechanism. Figure 2.4 shows the temperature profile as a function of time. A consistent trend is observed: the direct tabulation of reaction source tends to under-predict ignition delay compared to detailed chemistry calculations. This discrepancy can be mitigated by refining the tabulation grid, but even with 500 points in the progress variable space, the results are still not accurate. On the other hand, the tabulation/table look-up strategy reproduces the detailed chemistry calculation

with only 75 points, which is comparable to conventional requirements for tabulated chemistry [79]. This validates the developed strategy of the direct tabulation of time information instead of the reaction rate for ignition simulations.

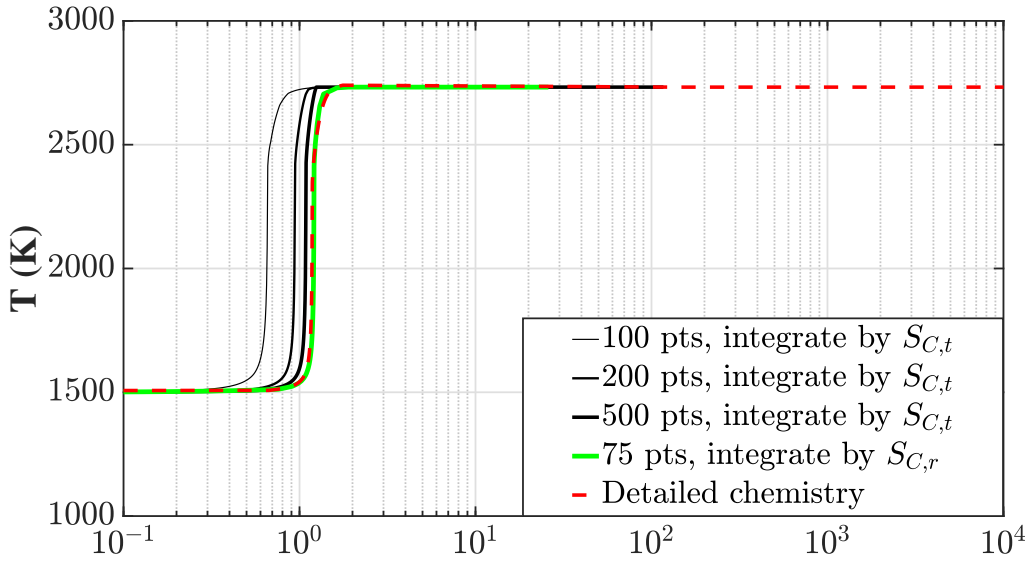

Figure 2.4: Ignition time history obtained from time integration of directly tabulated reaction source with different resolutions of C-axis (black), the new tabulation/table lookup strategy (green), and detailed chemistry calculation of homogeneous reaction (dashed red). The operating conditions are set to 1 atm and stoichiometry.

2.1.1.2 FPVA tabulation

The FPVA tabulation [80] is the flamelet-based method applied here for the description of flame front propagation. The method assumes what the structure of the flame is, and uses a tabulation approach to impose it in the CFD computation. Specifically, conventional FPVA tabulation solves a family of steady diffusion flamelets along the "Z-shaped curve"(or S-shaped when the maximum flamelet temperature is plotted against the inversion of scalar dissipation rate) and then maps the resulting solutions onto a lookup table of $\{Z, C\}$ [78]. Here, the FPVA tabulation requires an extra mapping variable (total enthalpy H) to account for the enthalpy rise due to

spark discharge. The modeling strategy of enthalpy variation here is similar to that of Ihme [81] and Mueller [82], which combines flamelets solved at different enthalpy levels. Counterflow diffusion flamelets are solved here with the boundary temperature of the oxidizer side ranging from room temperature (300 K) to higher levels (exact range is discussed later) with a fixed incremental step of 50 K. The exact method of how the enthalpy rise should be introduced into the diffusion flamelet (e.g., from the oxidizer boundary, from the fuel boundary, or from an external source within the domain) remains an open question, while previous studies of non-adiabatic premixed flamelets have concluded that the flamelet solution is insensitive to this factor [83, 84]. In this thesis, the oxidizer inlet temperature is varied, since in the target problem the igniter tip is immersed in an air stream (see Section 3.1.1). The flamelet solutions are then mapped onto the phase space of $H - Z - C$.

The remaining question is to determine to what extent can the temperature boundary be raised until the diffusion flamelet solutions can no longer be considered suitable for describing the turbulent flame structure here. Again, diffusion flamelets at elevated enthalpy not commonly encountered in FPVA tabulation and there is little existing tabulation strategy that can be referred to. However, a previous study of hydrogen-air counterflow diffusion flamelet [85] found that boundary temperature rise leads to partial extinction, which is a concept adopted here from studies of counterflow premixed flamelet to describe the extinction behavior of the counterflow flamelet [86–88]. During partial extinction, the flamelet shows a smooth response of temperature drop to strain rate increments. A demonstration is provided here for methane/air reaction in Fig. 2.5. It can be seen the temperature that leads to partial extinction is found to be about 2250 K for the shown test case. Above this temperature, the turning point on the Z-shaped curve disappears since the flame is more resistant to strain at higher inflow temperatures. This temperature, here, referred to as the partial extinction temperature T_p, is used as the upper limit of the diffusion flamelet

calculations. The reaction at a higher enthalpy level will therefore be modeled by HR calculations. The modeling assumptions of this treatment are provided as follows: (a) the boundary temperature that causes partial extinction in the diffusion flamelets is an indication of strong reaction, which supports the approximation of HR. (b) Diffusion flamelet solutions with partial extinction need to be obtained under a very large strain rate ($a_s = \mathcal{O}(10^6)$ 1/s) to get into the extinction region (low progress variable), which does not characterize the flow dynamics of the altitude relight problem. Reference [85] suggests flamelets under such operating conditions should be applied in combustion under very high strain, e.g., supersonic combustion. In this thesis, the phase space region of a high H-value and a low C-value should represent a kernel developing towards ignition, instead of a propagating flame front being quenched. In Section 3.3.1.1, a sensitivity study of the FPVA upper-temperature boundary is performed, where statistical results show that the ignition outcome is insensitive to this boundary.

Last, recall that in the HR tabulation, a time property $\Delta t_{HR,Tab}$ has been introduced for source term reconstruction. Here, to make the tabulation format consistent, an similar property is introduced into the FPVA tabulation. Firstly, the progress variable source $\dot{\omega}_C$ of the diffusion flamelet solutions can be directly mapped onto $H - Z - C$ space, denoted as $\dot{\omega}_{C,Tab}$. Then, along each iso-line of $\{H, Z\}$, $\Delta t_{FPVA,Tab}$ can be tabulated using the formula

$$\Delta t_{FPVA,Tab}(C_i) = \frac{C_{i+1} - C_i}{\dot{\omega}_{C,Tab}(C_i)}. \tag{2.5}$$

This time property can later be applied to the same source term look-up procedure (Eq. 2.4-2.3) and returns the correct source term value of the diffusion flamelets.

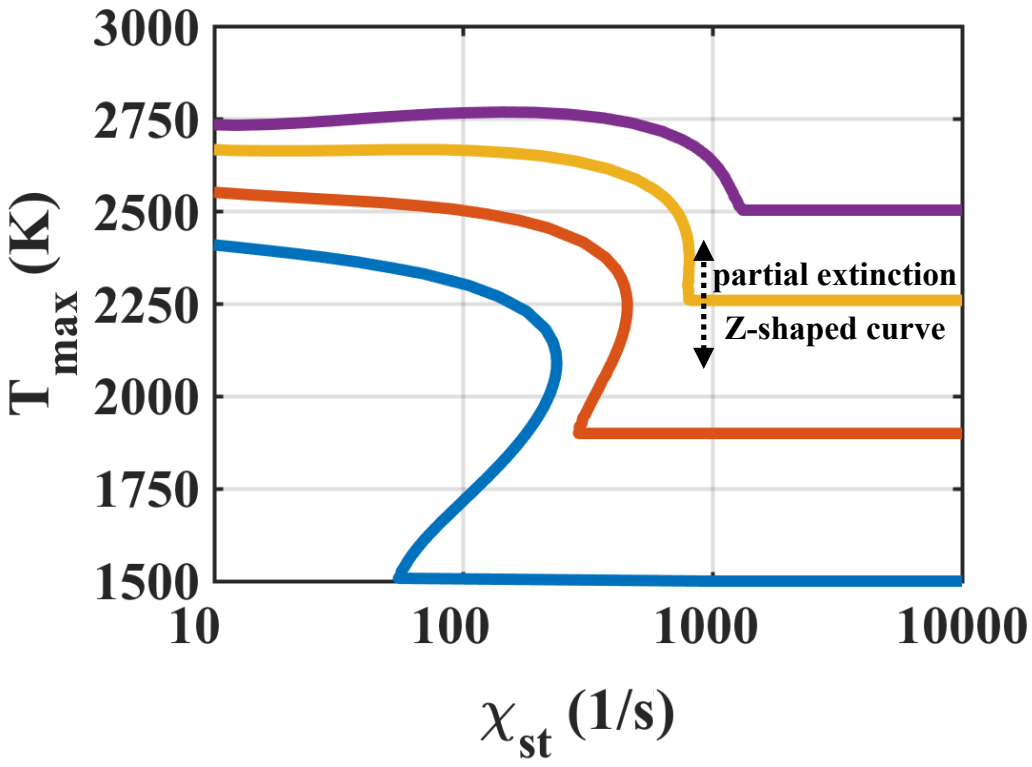

Figure 2.5: Maximum temperature vs. sthiochiometric scalar dissipation rate of methane/air counterflow diffusion flamelets obtained at different air stream temperatures. Fuel stream temperature is fixed at 600 K. Operating pressure is 1 atm.

2.1.1.3 Unified HR/FPVA Tabulation

For a convenient implementation in the CFD simulations, the two tabulation strategies (HR/FPVA) are unified into a single look-up table. For that, the two tabulations are built to carry the same thermochemical properties. As have been early introduced, the HR and FPVA tabulation are used to construct the look-up table for the high and low enthalpy phase space, respectively. Further, a blended tabulation is needed in the middle enthalpy region, to model the transition region between HR and FPVA. Here, the properties in the HR tabulation and the FVPA tabulation are denoted by the subscript "HR" and "FPVA", respectively, and the tabulated properties in the blended region are denoted by the subscript "Blended".

Note that the enthalpy bounds that separate the HR, Blended, and FPVA tabulations are not explicitly specified, but instead transformed from the temperature bounds applied to populate the HR and the diffusion flamelet solutions. Those temperature bounds, as defined in the last two sections, lead to an overlap of enthalpy between the lower bound of HR tabulation and the upper bound of FPVA tabulation (i.e., $H_{HR,min} < H_{FPVA,max}$, as shown by the dash lines in Fig. 2.6). In the unified table, the tabulated thermochemical properties in the blended region are calculated as a weighted average of the HR and FPVA tabulation, as

$$\phi_{Blended} = \frac{H - H_{HR,min}}{H_{FPVA,max} - H_{HR,min}}\phi_{HR} + \frac{H_{FPVA,max} - H}{H_{FPVA,max} - H_{HR,min}}\phi_{FPVA}, \tag{2.6}$$

where ϕ denotes a tabulated thermochemical property. The weighing factor in the above averaging simply follows a linear variation in between the two bounds of the blended region, so that $\phi_{Blended}$ degenerates to ϕ_{HR}/ϕ_{FPVA} at upper/lower bound.

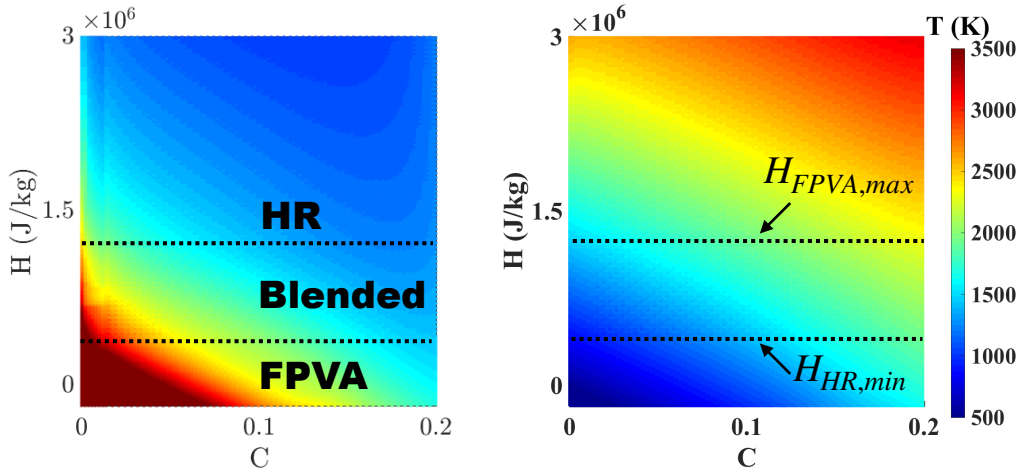

Figure 2.6: Unified FPVA/HR tabulation of Δt_{Tab} (left) and temperature (right) plotted in $\{H, C\}$-space, plotted at iso-plane of stoichiometric mixture fraction.

An example of the unified table is shown in Fig 2.6 and demonstrates the role of Δt_{Tab}, which is inversely proportional to the progress variable source. As the total

enthalpy H decreases, this ignition time increases as expected. In the FPVA region, the ignition time is very long ($> 10^2$ s) when C is close to zero, which indicates that a non-burning flamelet cannot be ignited without an external source of enthalpy. Note that the transition between the HR and FPVA regions is smooth, especially for thermophysical properties such as the temperature plotted here, which is important for the stability of the CFD simulation.

2.1.2 LES Simulation & CFD Solver

The turbulent flow is described using the large eddy simulation (LES) framework. In the LES approach, the governing equations of the fluid flow (i.e., mass, momentum, energy, and scalar transport) are filtered using a low-pass filter to obtain the LES transport equations, formulated as below.

Continuity equation:

$$\frac{\partial \overline{\rho}}{\partial t} + \frac{\partial \overline{\rho}\tilde{u}_j}{\partial x_j} = 0. \tag{2.7}$$

Momentum equation:

$$\frac{\partial \overline{\rho}\tilde{u}_i}{\partial t} + \frac{\partial \overline{\rho}\tilde{u}_j\tilde{u}_i}{\partial x_j} = -\frac{\partial \tilde{p}}{\partial x_i} + \frac{\partial \widetilde{\overline{\sigma}_{ij}}}{\partial x_j} + \frac{\partial \overline{\rho}(\tilde{u}_i\tilde{u}_j - \widetilde{u_i u_j})}{\partial x_j}. \tag{2.8}$$

Scalar transport equation:

$$\frac{\partial \overline{\rho}\widetilde{\Psi}}{\partial t} + \frac{\overline{\rho}\tilde{u}_j\widetilde{\Psi}}{\partial x_j} = \frac{\partial}{\partial x_j}\left(\widetilde{D}_\Psi \frac{\partial \widetilde{\Psi}}{\partial x_j}\right) + \frac{\partial \overline{\rho}(\widetilde{\Psi}\tilde{u}_j - \widetilde{\Psi u_j})}{\partial x_j} + \overline{\rho}\widetilde{\dot{\omega}}_\Psi. \tag{2.9}$$

In the above equations, $\overline{\rho}$ denotes the fluid density, $\tilde{u}_i$ is the i^{th} component of the velocity vector, $\tilde{p}$ is the hydrodynamic pressure, $\widetilde{\overline{\sigma}}$ is the viscous stress tensor that's further calculated as

$$\begin{cases} \widetilde{\sigma_{ij}} & = 2\mu\widetilde{S_{ij}} - \frac{2}{3}\tilde{\mu}\delta_{ij}\widetilde{S_{kk}}; \\ \widetilde{S_{ij}} & = \frac{1}{2}\left(\frac{\partial \widetilde{u_i}}{\partial x_j} + \frac{\partial \widetilde{u_j}}{\partial x_i}\right), \end{cases} \tag{2.10}$$

with $\tilde{\mu}$ being dynamic viscosity and δ being the Kronecker delta, Ψ denotes a transported scalar (i.e., H, Z, and C) with $\widetilde{D}_{\Psi}$ being its the molecular diffusivity. The non-linear closure terms for sub-filter transport are modeled using the gradient diffusion hypothesis. A dynamic subgrid-scale model [89] is used to obtain the turbulent viscosity. The turbulent diffusivity is obtained using a constant turbulent Schmidt number $Sc_t = 0.72$. A constant turbulent Prandtl number $Pr_t = 0.7$ is used for the energy equation. Besides, the filtered mixture fraction variance $\widetilde{Z}_v$ is evaluated in the LES simulation, which is obtained by assuming a local equilibrium among production and dissipation rate [90], as

$$\widetilde{Z}_v = C_v \Delta^2 |\nabla \tilde{Z}|^2, \tag{2.11}$$

where Δ is the filter width (i.e., here, the grid size), and C_v is a constant that can be either specified or obtained dynamically. Here, the value $C_v = 0.1$ is applied [91].

The thermochemical properties are obtained based on the tabulation procedure described in Sec. 2.1.1. For molar diffusivity, while the unity Lewis number assumption is widely applied in the turbulent combustion modeling community, differential diffusion effects are not always negligible. In this thesis, differential diffusion effects are neglected in the LES equations for C and H, but not for Z. Such a blended treatment is justified for the altitude relight problem as followings. For C, the concentration of highly diffusive species (e.g., H_2) are generally low. For H, the strong energy diffusion presents only at locations of low concentrations of the jet fuel species (igniter are often displaced at fuel-lean locations) that feature non-diffusive large molecules. For Z, however, the unity Lewis number assumption is less reasonable, mainly due to the presence of the non-diffusive jet fuels that are actively involved in the fuel-mixing. The modeling of differential diffusion effects in tabulated chemistry remains to be an open topic [92, 93]. Here, as an alternative compromise to partially capture the high Lewis number effect of the realistic jet fuels, the molar diffusivity of Z is modeled by that of the lumped fuel species [94]. Similar methods have been ap-

plied in the soot modeling community to model the diffusion of PAH species [95, 96], which are also non-diffusive large molecules.

A presumed-PDF approach is used for modeling turbulence-chemistry-interactions. The laminar table is convolved with the joint-PDF of the input variables (i.e., Z, C and H) that describe the subfilter variations [52, 80], as

$$\widetilde{\phi} = \iiint f(H, Z, C)\phi(H, Z, C)\, dH\, dZ\, dC, \tag{2.12}$$

Following prior work [97], the subfilter variations of each variable are assumed independent of each other and the joint-PDF of the input variables becomes the product of three marginal PDF. The marginal PDF of mixture fraction is described by a β-function, characterized by the filtered mixture fraction mean and variance. The marginal PDFs of C and H are assumed to be described by δ-functions, expressed in terms of the filtered variables. The resulting table contains four input variables (filtered mixture fraction mean and variance, filtered progress variable, and filtered enthalpy), as

$$\widetilde{\phi}(\widetilde{Z}, \widetilde{Z_v}, \widetilde{C}, \widetilde{H}) = \iiint \beta(Z; \widetilde{Z}, \widetilde{Z_v})\delta(C - \widetilde{C})\delta(H - \widetilde{H})\, dZ\, dC\, dH, \tag{2.13}$$

The LES models are implemented in the OpenFOAM open-source code base, which has been specifically modified to minimize kinetic energy dissipation [98]. Supported by the scale separation between the shock and kernel penetration speed (Sec. 4.2.4.1), a low-Mach number assumption is used to solve the gas phase, i.e., the energy equation is decoupled from the momentum equation and the pressure-velocity coupling is achieved using the pressure-implicit with splitting of operator (PISO) algorithm [99] with an incompressible pressure correction equation. A time-staggering approach along with second-order discretization schemes for the convection and diffusion terms are used, and the governing equations are solved using a semi-implicit

Euler method that is second-order in time.

2.1.3 Coupling between the Kernel and the Turbulent Flow

Spark initiation results in a soup of free radicals, ionized species, and rapidly expanding shock waves. Since these events occur at time scales much shorter than that for turbulence or ignition processes, their net effect can be modeled as a volumetric source term in the form of energy deposition that affects the local enthalpy of the fluid. The discussion below describes the formulation of this energy source model. The justification for the assumption of fast time scales is provided in Sec. 4.2.4.1.

2.1.3.1 Challenges in modeling aircraft spark igniter discharge

Previous ED strategies mainly apply a volumetric source that follows certain spatio-temporal distributions [61, 62, 66]. In IC engine spark ignitions, the shape, and movement of the electric arc are further tracked using Lagrangian particles [100] which nonetheless involves applying a volumetric source to the finite control volume. These strategies are suitable when the igniter electrode is directly exposed to the outer flow and the amount of deposited energy is relatively low [62, 101]. When applying a volumetric energy source, the parameters of the enforced profiles are often set to values that do not necessarily reflect the actual physics. For instance, the kernel size is set to the value of the post-discharge high energy fluid pocket after it has expanded until a much later stage where the local enthalpy spike is relaxed to below the upper temperature limit of the thermodynamic database (3000 $\sim$ 5000 K for typical chemical mechanisms). Alternatively, the duration of the volumetric source enforcement is relaxed by a certain factor from the actual electrical breakdown period to avoid the temperature beach. In fact, such adjustments are almost inevitable, as most combustion mechanisms are not designed to handle the thermodynamic inclusion of the high-energy gas at the early post-discharge time, which involves thermal

non-equilibrium and plasma physics. In the end, as long as the effective amount of energy is deposited into the gas phase, those treatments should serve as a reasonable approximation. In this study, the applied coupling method follows the same principle but is formulated quite differently from conventional volumetric sources to properly represent the aircraft igniter discharge.

To facilitate the discussion, a schematic of the target igniter applied in this thesis is plotted in Fig. 2.7. The igniter is a commercial aircraft igniter designed by original equipment manufacture (OEM). As has been introduced in Sec. 1.2.1, there are mainly two types of configurations of the aircraft surface discharged spark igniter, i.e., the flush fire igniter and the sunken fire igniter. The target igniter applied here belongs to the second type - the sunken fire igniter. The feature of the sunken fire igniter is that the spark gap in between the igniter central and outer electrodes are recessed from the igniter outer surface, forming a confined spatial region referred to as the "igniter cavity". In contrary to the flush fire igniter where the kernel is allowed to expand freely, here, the spark discharge takes place within this relatively confined environment. This introduces a pulsing effect of the kernel following its early stage post-discharge expansion. The pulsing effect provides the kernel a prominent momentum, and the kernel dynamics will strongly affect its downstream fuel entrainment (Section. 3.2.1) and reaction (Section. 3.2.2.2). Therefore, the applied ED here should not only introduce the proper amount of energy but should also reproduce this pulsing effect. In theory, the pulsing effect can be captured by detailed simulations of the gas expansion within the igniter cavity during and following the spark discharge (i.e., using a volumetric energy source displaced within the igniter cavity). However, as will be later demonstrated (Section. 4.2), existing numerical capabilities cannot accurately capture the kernel geometry, velocity, nor the effective deposited energy of this sunken fire igniter.

The challenges here are mainly two-fold. The first one is the above-mentioned,

that existing thermodynamic database (at least for most of those available for combustion simulations) rarely provides the modeling inclusion of high-energy gas. Here, for the aircraft igniter, such challenge becomes much more prominent compared to conventional application of spark igniter such as an IC engine spark plug, as the energy release is by orders of magnitude higher. For instance, the nominal spark energy of an IC engine spark plug is about 50 mJ, whereas that of a surface discharged aircraft igniter is about $1 - 10$ J. The other challenge is a practical issue, that the inner dimensions of the target igniter are not available as the igniter is an intellectual property (IP), making it impossible to perform accurate simulation of the gas expansion within the igniter cavity. Later, in Chapter IV, a supplemental study is carried out to address these challenges. Here, a "shortcut" is taken with an alternative approach of ED to achieve the coupling between the kernel and flow field, which is shown on the r.h.s. of Fig. 2.7. Instead of using volumetric energy source, the ED here is intro-

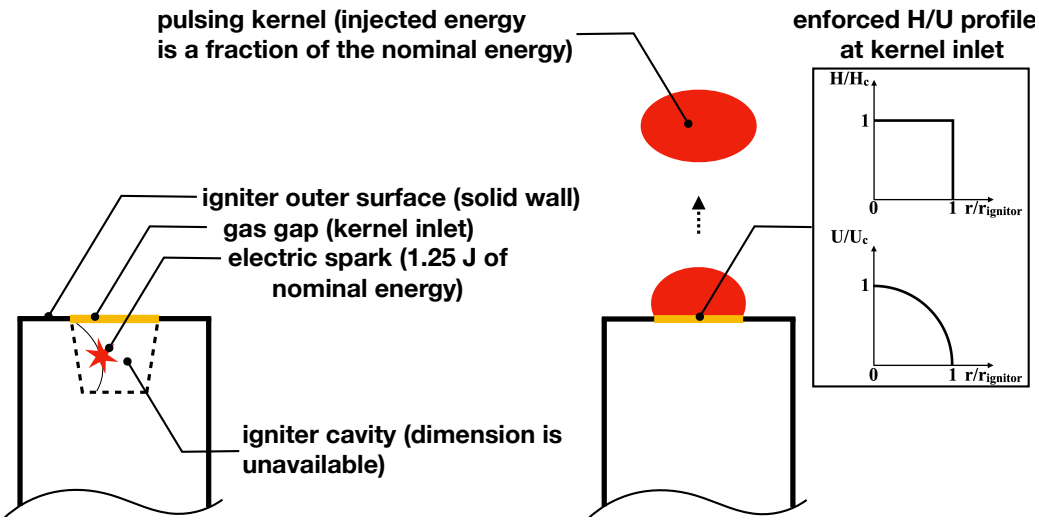

Figure 2.7: Schematic of the coupling of the kernel and flow field.

duced from a boundary surface that represents the opening spark gap on the igniter top outer surface, referred to as the "kernel inlet" (yellow lines in Fig 2.7). Similar approaches have been applied by Jaravel *et al.* [102] and Rieth *et al.* [8] for simulating

the same igniter. The gas phase properties of the injected kernel are estimated using a 0-D analysis of the kernel expansion process, whereas the dynamic properties are calibrated against experimental data of the kernel shape and trajectory. The details are presented below.

2.1.3.2 Energy deposition introduced from simulation boundary

At the kernel injection boundary, velocity and enthalpy are specified using time-dependent Dirichlet conditions. Note that the kernel is made of air at an elevated temperature and does not contain fuel (Sec. 3.1.1), and therefore the mixture fraction field requires no special treatment here. The applied temporal and spatial profiles are summarized in Fig. 2.8 where H_{ker} and U_{ker} are respectively the characteristic value of the kernel enthalpy and velocity, t_{init} is the time at which the enthalpy and velocity boundary enforcement start, t_{term} is the time at which the enthalpy boundary enforcement ends, τ_{ker} is the duration of the velocity boundary enforcement, and $r_{igniter}$ is the radius of the igniter top surface. This functional form for boundary conditions is adopted so that the trajectory of individual kernels reasonably approximates the experimental observations. More details are provided below.

A uniform spatial profile is used for the kernel enthalpy boundary, where the characteristic value H_{ker} is linearly related to the spark deposit energy E_d by 0-D energy conservation as

$$H_{ker} = H_0 + \frac{E_d}{\rho_0 V_{cav}}. \tag{2.14}$$

E_d measures the energy deposited into the gas phase during the spark discharge. This value cannot be exactly controlled and is considered a random variable for the uncertainty quantification (described in the next section). E_d is related to E_n which is the nominal electrical energy of the discharge arc. In this case $E_n = 1.25$ J [5]. The deposition efficiency which is the ratio of E_d to E_n was assumed to be 90–95% due to the short discharge duration [101]. However, note that the high deposition efficiency

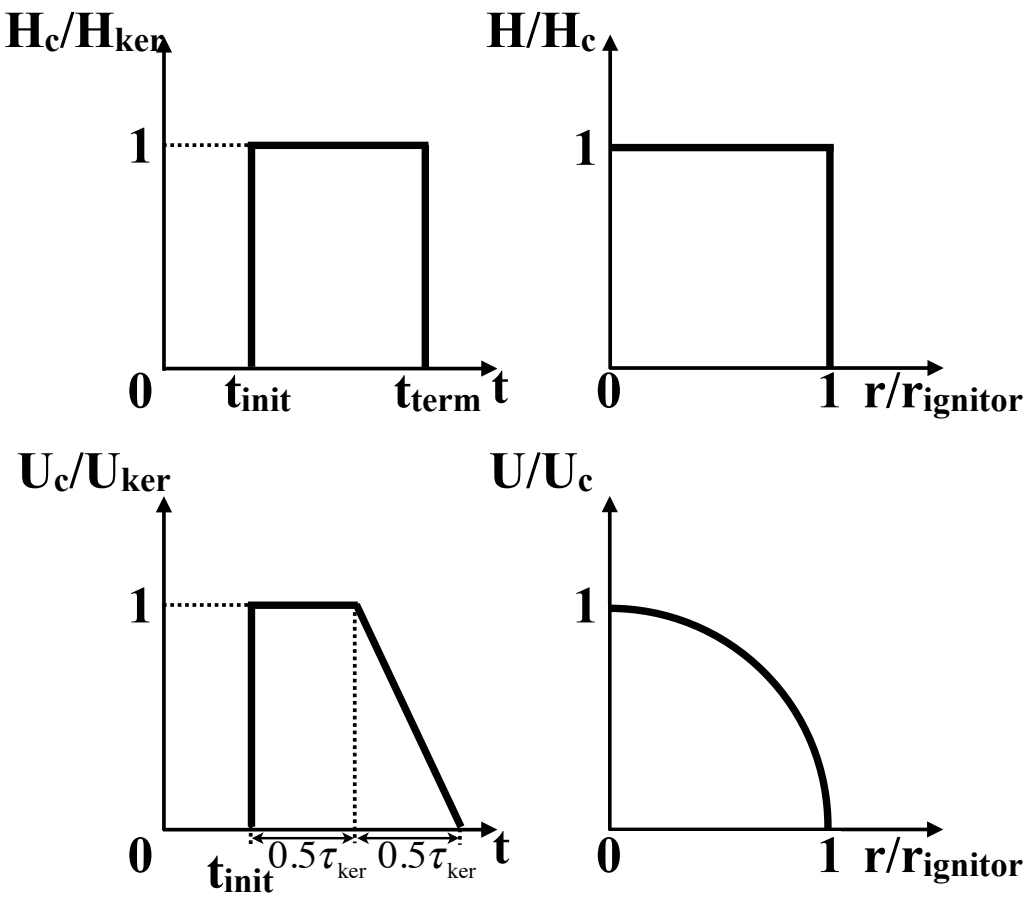

Figure 2.8: Temporal (left) and spatial (right) profiles of total enthalpy (top) and normal velocity (bottom) applied at the kernel boundary. Subscript 'c' denotes value at the boundary center, and 'ker' denotes the bulk value.

here is not a direct measure for the final efficiency, as eventually only a fraction of E_d enters the domain. H_0 and ρ_0 are the pre-discharge flow properties. The volume of the igniter cavity V_{cav} is 0.2 cm^3 (Sheng, personal communication, October 2017). Essentially, the 0-D approximation of H_{ker} at the kernel inlet boundary allows the local enthalpy spike at early post-discharge within the igniter cavity to relax towards thermodynamic homogeneity, and the resulting H_{ker} is dropped to the same orders of magnitude of upper enthalpy limit of the thermodynamic model (H_{max}), although some necessary clipping is still needed during the following calculation of thermodynamic properties (see Fig. 2.9). By applying V_{cav} in Eq. 2.14, it is assumed that the

cold flow within the entire igniter cavity is entrained into the kernel during the initial post-discharge kernel expansion before the kernel enters the flow domain. A more accurate calculation by Sforzo using 0-D perfectly stirred reactor (PSR) modeling [5] also confirms that the entrained volume of cold flow during the initial kernel expansion is $\mathcal{O}(0.1)$ cm^3 to obtain a reasonable initial thermodynamic state of the injected kernel, which is close to V_{cav} here. The kernel enthalpy boundary follows a step profile, which is initiated when a spark discharge is triggered. The profile is terminated at t_{term}, which is triggered during simulation run-time as soon as a prescribed volume of kernel enters the domain, denoted by V_{ker}. This volume quantity is also difficult to control in the experiments, and only estimates are available [5, 6]. Here, the order of $\mathcal{O}(0.25)$ cm^3 is applied for V_{ker}, which was found to best reproduce the initial kernel diameter compared to Schlieren measurements [5].

Since a number of parameters of similar physical meanings are involved in the above kernel enthalpy boundary condition, a diagram is provided in Fig. 2.9 to clarify the relationships between them. The parameters in the green boxes are inputs used to control the kernel enthalpy boundary setup, whereas those in the red boxes are explicitly enforced at the kernel inlet boundary during the simulation. As summarized in the bottom of Fig. 2.9, the final amount of energy introduced into the domain is an implicit function of E_d and V_{ker}. Besides, as $\rho_{ker}V_{ker} < \rho_0 V_{cav}$ (mainly due to the density ratio), the final energy rise introduced into the domain is only a fraction of E_d. This "rule of fraction" has been followed in other previous studies [5, 102], and is further confirmed by a more recent experimental study that provides accurate measurements on the pulsing kernel generated the target igniter [9]. Here, based on the particular simulation case setups (H_{max} is thermal-model-dependent), the equivalent fraction of the actual energy introduced into the CFD domain to the kernel boundary characteristic energy (E_d) is about $20 - 30\%$.

Apart from relaxing the initial high enthalpy gas, another purpose of introducing

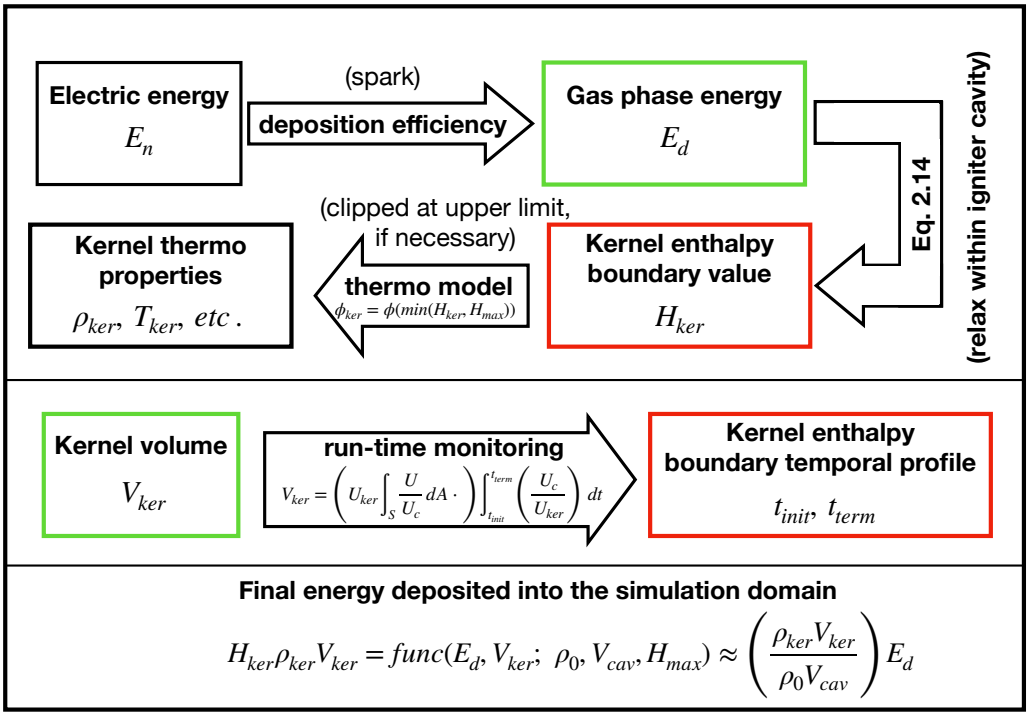

Figure 2.9: Diagram of relationships between parameters involved in enthalpy boundary conditions at the kernel inlet. Green boxes indicate controlling parameters of the boundary setups. Red boxes indicate parameters explicitly enforced at the boundary (i.e., profiles in Fig. 2.8).

ED from the kernel inlet is to reproduce the pulsing effect, for which a spatio-temporal velocity profile is also enforced at kernel inlet. The velocity boundary condition consists of two parts (see Fig. 2.8). Here, the velocity at the center of the injector U_c is obtained from a trapezoidal profile that depends on a nominal kernel velocity U_{ker}. A spatial parabolic profile is then applied across the injector diameter. The kernel injection duration τ_{ker} and velocities are again subject to uncertainty but are $\mathcal{O}(50)$ μs and $\mathcal{O}(300)$ m/s, respectively, in order to reproduce the observed kernel shapes and trajectories.

In summary, the kernel coupling strategy developed above is fully specified by four parameters $K = \{E_d, V_{ker}, U_{ker}, \tau_{ker}\}$. The uncertainty of the initial spark discharge can therefore be represented as uncertainties for these parameters. The approach for

treating these uncertainties will be discussed separately in the next section. In order to demonstrate the validity of the chosen set of parameters, a nominal simulation has been performed in Sec. 3.2.1, which reproduced the time sequence of kernel shape and locations reasonably well. In the following discussions about ignition probability estimation, this coupling method as well as the flow and combustion models described above will be used.

2.2 Ignition Probability Estimation

As has been introduced in Sec. 1.2.3, ignition is heavily influenced by inherent variabilities in the spark deposition process and the turbulent flow. It is then natural to consider ignition probability, which is essentially the probability that ignition success will occur for a set of macroscopic nominal conditions. In this thesis, the interested macroscopic variables include the global equivalence ratio of the main flow, the main flow temperature, and the applied fuel type. In general, the estimation of such ignition probability is carried out using uncertainty quantification (UQ) approaches [103, 104].

Very simply, these approaches use a Monte-Carlo type method that treats the variabilities as arising from a known probability distribution, and conducting an ensemble of computations with parameter values sampled from this distribution. A diagram of the modeling procedure applied here for ignition probability is shown in Fig. 2.10. The main components are on the forced ignition simulation (Sec. 2.1) and the sampling procedure, which together allow variability of macroscopic variables to be included. Since the underlying LES calculations are computationally intensive, it is necessary to determine the most important sources of variability so as to limit the size of the ensemble. In this section, these issues and the resulting UQ procedure is described.

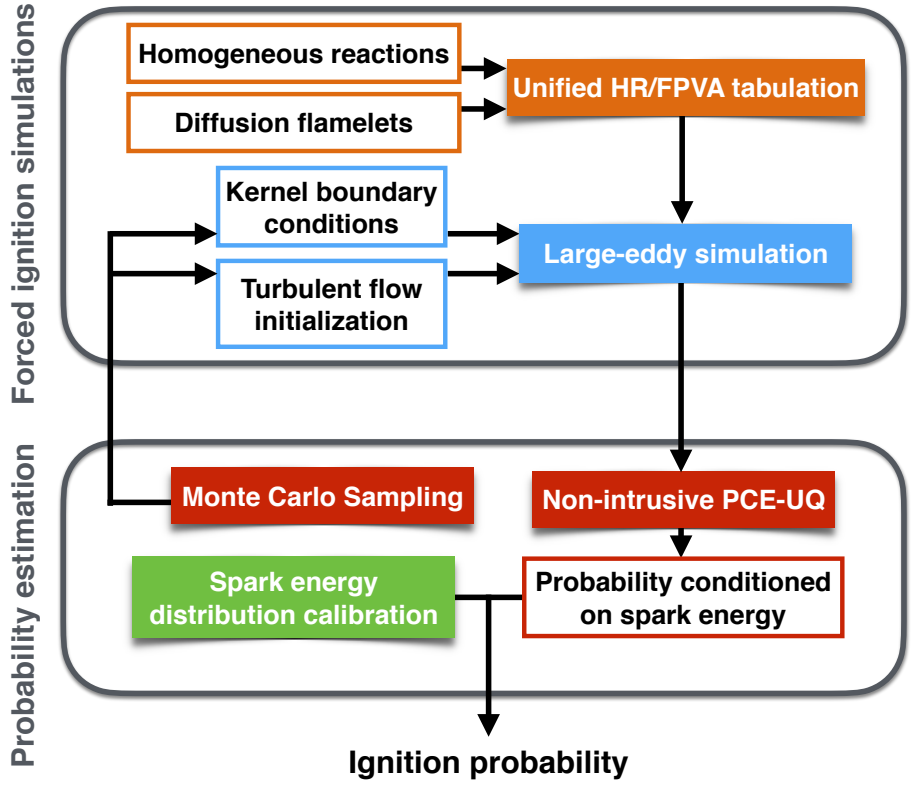

Figure 2.10: Diagram of the modeling procedure for ignition probability estimation.

2.2.1 Formulation of Uncertainty Problem

The uncertainty in ignition comes from the kernel parameters K and the state of the initial turbulent flow field ξ. The latter quantity is a high-dimensional vector that describes the initial velocity and scalar fields at the M grid points used to solve the LES fields. The approximation of these parameters is later made. Without losing generosity, the probability of ignition is formally expressed by these parameters, as

$$P_I(O) \triangleq E(I(K,\xi;O)) = \iint I(K,\xi;O) f_{K,\xi}(K,\xi;O)\, dK\, d\xi. \tag{2.15}$$

Here, I is the ignition indicator function which is binary in between 0 (failed ignition) and 1 (successful ignition), $E(.)$ is the expectation operator (average over statistical

distribution), $f_{K,\xi}$ is the joint probability density function of K and ξ, and O denotes the parameters that define the operating conditions (e.g., main flow temperature T). In Eq. 2.15, K and ξ are vectors of random variables, while O is treated as a non-random parameter should affect the shape of the joint-PDF and, of course, the ignition indicator function. The inner integration of the joint PDF in Eq. 2.15 can be further replaced by the following conditional ignition probability

$$P_{I|K}(K, O) = \int I(K, \xi; O) f_{\xi|K}(\xi; O)\, d\xi, \tag{2.16}$$

where $f_{\xi|K}$ is the conditional probability density function of ξ. Eq. 2.16 measures the ignition probability conditioned on a specific kernel parameters. By plugging Eq. 2.16 into Eq. 2.15, the ignition probability can be re-expressed as

$$P_I(O) = \int P_{I|K}(K, O) f_K(O)\, dK. \tag{2.17}$$

$f_K(K)$ is the PDF of K that is assumed to be known and independent of the operating conditions and the local turbulence properties.

In short, the computational strategy applied here (Eq. 2.17) is to first determine the conditional ignition probability due to the impact of turbulence on a particular choice of kernel parameters K, and then compute final ignition probability by convolving the resulting conditional probability with the PDF of kernel parameters K. The conditional ignition probability $P_{I|K}$ accounts for the uncertainty associated with the turbulence and is approximated using an empirical mean of the ignition indicator obtained from multiple simulations. The PDF f_K accounts for the uncertainty associated with the spark discharge, and it can be obtained either directly from prior knowledge of the igniter discharge characteristics, if such direct information is available, or indirectly from other experimental information (e.g., experiment measured ignition probability) using a calibration procedure developed in this thesis (explained

in Sec. 2.2.3).

The above approach provides a convenient path to evaluating the effect of the high-dimensional turbulent flow field while providing a functionally smooth probability function ($P_{I|K}$ in Eq. 2.17) rather than a binary indicator function (I in Eq. 2.15). This latter feature is especially useful as the conditional ignition probability can be determined as a continuous function of K and O (response surface) using the polynomial chaos expansion (PCE) approach, which further enables the implementation of probability density integration and distribution calibration. Details of evaluating each of the two components of $P_{I|K}$ and f_K are explained in the following sections.

2.2.2 Evaluation of Conditional Ignition Probability

The conditional ignition probability $P_{I|K}$ as a function of kernel parameters K and operating condition O is first estimated by Monte-Carlo sampling at discrete phase space locations. Then, a continuous response surface of the conditional ignition probability is constructed based on the sampling results using the PCE approach.

2.2.2.1 Monte-Carlo sampling

The conditional ignition probability $P_{I|K}$ in Eq. 2.16 is here evaluated by the empirical mean value $P_{I|K,Spl}$, as

$$P_{I|K}(K,O) = P_{I|K,Spl}(K;O) + \varepsilon_{Spl}(K,O), \tag{2.18}$$

where the r.h.s. first and second terms are respectively the statistical estimator and the statistical error. In specific, $P_{I|K,Spl}$ is obtained from Monte-Carlo simulation, as

$$P_{I|K,Spl}(K,O) = \frac{1}{N}\sum_{\xi\in\Xi} I_{Spl}(\xi,K;O), \tag{2.19}$$

where N is the number of samples, Ξ is the ensemble of N turbulent flow fields used in the empirical mean, and I_{Spl} is the ignition indicator value (1 or 0) obtained from each LES simulation (not exactly true, to be explained soon).

The sampling of turbulence to represent the correct probability density function is a computationally expensive problem. To be precise, the statistically stationary flow without the kernel discharge subscribes to an attractor in high-dimensional space [105, 106]. To obtain the correct density of initial conditions, points on this attractor need to be sampled. It is known that even for low Reynolds number flows, the dimension of this attractor can be sufficiently large that such a direct sampling will be expensive [52, 105, 106]. In this study, it is assumed that the fully developed main and kernel flow (the crossflow) moves on an attractor, which is valid for ergodic systems [107]. Therefore, starting the ignition calculations at different initial times is equivalent to sampling the attractor.

In practice, initial turbulent flow fields are first obtained by sampling a cold flow simulation for every specific time interval Δt_{Spl}, which constitutes a database of initial turbulent flow fields in the phase space of cold flow time-space t_{cold}. Then, by initialization the forced ignition simulations with different snapshots in this database and trigger the spark discharge at the beginning of each hot flow simulation ($t_{hot} = 0$), it is equivalent to starting the ignition calculations at different initial times in the cold flow time-space, denoted here as $t_{Spl,i}$ with i being the sample index. A diagram is provided in Fig. 2.11 to demonstrate this strategy. The sampling interval is chosen such that the initial turbulent flow field between samples can be considered as statistically independent, as

$$\Delta t_{Spl} > l_{int}/U_{bulk}, \tag{2.20}$$

where l_{int} is the integral length scale estimated as the ensemble and spatial average

of $\frac{k^{3/2}}{\varepsilon}$, k is the turbulent kinetic energy, ε is the turbulent dissipation rate estimated from the filtered strain rate tensor, and U_{bulk} is the bulk streamwise velocity in the target configuration. For the validation studies to be presented in Chapter III, $\Delta t_{Spl} >$ 5 ms and $N = 15$ was found to be adequate. The cold flow LES database can be reused for the sampling of K, assuming the initial status of turbulence is independent of the kernel parameters, but needs to be regenerated for every sampled level of O, as the gas phase thermodynamic properties are dependent on O.

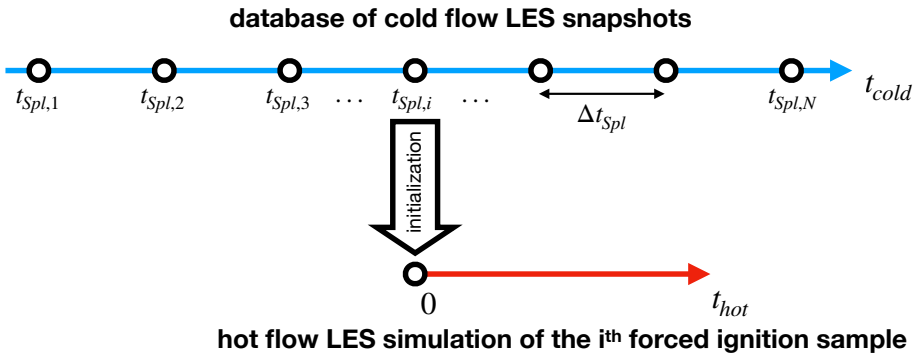

Figure 2.11: Schematic of the turbulent flow field initialization strategy.

With this above strategy, the sampling of Eq. 2.19 is to re-formulated as

$$P_{I|K,Spl}(K,O) = \frac{1}{N}\sum_{i=1}^{N} I_{Sim}(t_{Spl,i},K;O), \tag{2.21}$$

which needs to be evaluated at prescribed locations in the phase space of $K-O$, denoted as $\{K_{Spl,j=1\sim M}, O_{Spl,k=1\sim L}\}$, with M and L being respectively the total number of sampling levels in K and O directions. As K and O are high-dimension vectors, dimensionality reduction is inevitable in order to scale down the problem and is implemented based on the particular configuration and study objective. In the later validation studies, for the macroscopic operating conditions O, the three components of global equivalence ratio ϕ, main flow temperature T_{in}, and fuel type Ft are chosen to be sampled, each component being varied at a time, i.e., at sparse locations

in the 3-D phase spaced of $\phi - T_{in} - Ft$. For the kernel parameters K, the degree of freedom has already been limited to 4 in Sec. 2.1.3, as $K = \{E_d, V_{ker}, U_{ker}, \tau_{ker}\}$, which is further simplified to 1 as will be discussed in the next chapter. Moreover, if the ignition outcome exhibits a monotonic relationship with K, then it provides a feature that can be taken advantage of to effectively reduce the computational cost of the sampling procedure, as explained below.

To facilitate the discussion, assume the kernel parameter K is a scalar variable and the ignition indicator function monotonically increases with K. For each sampled level of O, the above sampling procedure is equivalent to the evaluation of $I(t_{Spl}, K; O)$ at the 2-D structured grid points of $\{t_{Spk,i=1\sim N}, K_{Spl,j=1\sim M}\}$ (see Fig. 2.12). At the beginning of this section, it is suggested that each I_{Spl} should be obtained from an LES simulation, which is only necessary when no prior knowledge of the distribution of I_{Spl} in the phase space of $t_{Spl} - K_{Spl}$ is given. However, the with the monotonic relation between I and K being assumed, the evaluation in the K_{Spl}-direction can be performed in a bisectional manner until the two adjacent grid points that bifurcate failure/success is found (highlighted by blue dash boxes), and therefore skipping the LES simulation on a lot of sampling points. With this strategy, the number of LES simulations can be reduced by a factor of $\mathcal{O}(M/log_2 M)$, which should be exploited whenever possible. From the aspect of the forced ignition physics, such a scalar variable K can often be defined in some forms related to the kernel energy (e.g., in Sec. 3.2.2.2, $K = E_d$). Namely, if two successive realizations produce successful ignition, then the LES simulation of higher kernel energy need not be considered since they will produce successful ignition as well, and vice versa for the failed ignition case.

2.2.2.2 Response surface reconstruction with PCE

One of the challenges with the sampling approach described above is that the numerical results are discrete in nature, providing outcomes for discrete values of

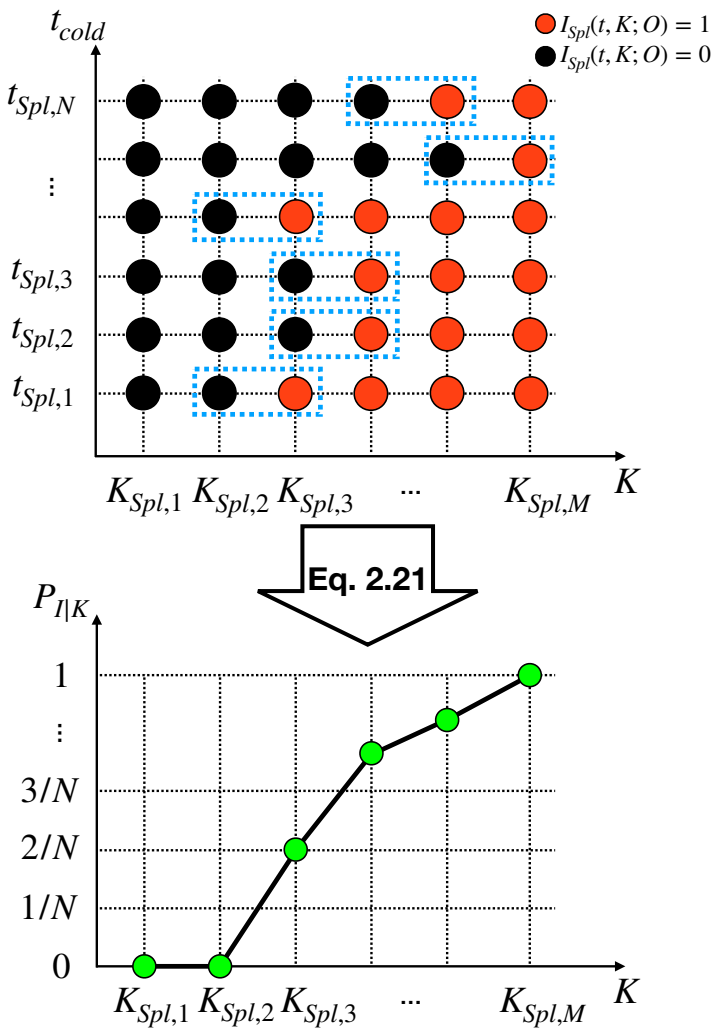

Figure 2.12: Schematic of the sampling procedure provided I varies monotonically with K.

kernel parameters and operating conditions. However, to convolve the conditional ignition probability $P_{I|K}$ with the probability of the kernel properties $f(k)$, and to calibrate the distribution of $f(K)$ against experimental data measured at arbitrary levels of O, the output of the model should be made continuous in the phase space of $K - O$. For this purpose, so-called response surfaces are constructed, which provides a continuous surrogate of the discretely sampled $P_{I|K,Spl}$. The response surfaces are constructed using polynomial chaos expansion (PCE) [103, 108], which traditionally

is used to represent a random variable as a linear combination of polynomials of other random variables. Here, it is used to represent a random variable (the probability of ignition) as a function of one random variable (K) and one deterministic variable (O), as

$$P_{I|K,Spl}(K,O) = P_{I|K,PCE}(K,O) + \mathcal{R}_{PCE}(K,O), \tag{2.22}$$

where the PCE output is denoted by subscript "PCE", and $\mathcal{R}_{PCE}$ is the residual of the expansion.

The reconstruction details are as follows. Firstly, the PCE takes the form

$$P_{I|K,PCE}(K,O) = \sum_{n=0}^{\infty} \alpha_n \Psi_n \left(K,O\right), \tag{2.23}$$

where Ψ_n are the elements of basis in which the ignition probabilities are expressed, and α_n are the coefficients representing the projection of $P_{I|K,Spl}$ onto each basis function. Here, the Wiener-Hermite polynomials are used ($\Psi_n = H_n$), through which the infinite sum can be represented using a truncated sum [103]. Then, Eq. 2.22 can be expressed as:

$$\begin{aligned} P_{I|K,Spl}(K,O) &= P_{I|K,PCE}(K,O) + \mathcal{R}_{PCE}\left(K,O\right) \\ &= \sum_{n=0}^{q} \alpha_n H_n \left(K,O\right) + \mathcal{R}_{PCE}\left(K,O\right), \end{aligned} \tag{2.24}$$

where q is the order of the truncation and $\mathcal{R}^T_{PCE}$ is the residual of the expansion. Obtaining the PCE approximation of $P_{I|K,Spl}$ is then equivalent to obtaining estimates of α_n, which is done here using non-intrusive methods [109]. The non-intrusive PCE requires the evaluation of the deterministic model output for various model inputs. Here, $x = \{K, O\}$, with necessary re-scaling as the PCE are describable with Hermite polynomials only for random variables following a standard normal distribution [110].

The PCE coefficients α_n are computed by formulating the following linear system

$$\begin{bmatrix} H_0(x_0) & H_1(x_0) & \dots & H_Q(x_0) \\ H_0(x_1) & H_1(x_1) & \dots & H_Q(x_1) \\ \vdots & \vdots & \vdots & \vdots \\ H_0(x_m) & H_1(x_m) & \dots & H_Q(x_m) \end{bmatrix} \begin{bmatrix} \alpha_0 \\ \alpha_1 \\ \vdots \\ \alpha_Q \end{bmatrix} = \begin{bmatrix} P_{I|K,Spl}(x_0) \\ P_{I|K,Spl}(x_1) \\ \vdots \\ P_{I|K,Spl}(x_m) \end{bmatrix}, \tag{2.25}$$

where m is the number of data points $\{K_{Spl,j=1\sim M}, O_{Spl,k=1\sim L}\}$ (i.e., $m = M \cdot L$), and $Q = \frac{(r+q)!}{r!q!} - 1$, with q being the truncation order. The applied truncation order here is $q = 6$. Note that the total number of data points m does not need to be equal to Q. In fact, it was found to yield a better approximation of the model output statistics when $m \geq 2(Q+1)$ [111, 112], and the coefficients are then obtained in a least-square sense.

Theoretically, the above method is able to reconstruct the response surface with the same dimensionality of the fully-expanded phase space of $K - O$. In practice, the target problem is always constrained to a limited number of dimensions. Following the dimensionality reduction explained in the last section, in the validation studies to be presented in Chapter III, K is reduced to a scalar variable, and multiple 2-D response surfaces ($r = 2$) are constructed for each investigated component of O. In specific, for the study of the global equivalence ratio ($O = \phi$), the surface is created in the phase space of $K - \phi$; for that of the main flow temperature ($O = T_{in}$), the surface is created in the phase of $K - T_{in}$; for that of the fuel type Ft, the investigated O are two-dimensional ($O = \{\phi, Ft\}$), and response surfaces are reconstructed in the phase space of $K - \phi$ for each sampled Ft.

2.2.3 Evaluation of the Statistical Distribution of the Kernel Parameter

The conditional ignition probability has taken into consideration variabilities in turbulent flow and provided a function that only depends on one random variable - the

kernel parameter. This parameter is not precisely known, the probability of ignition is obtained by convolving the conditional ignition probability with the statistical distribution of the kernel parameters, which provides a measure of ignition odds for a given set of operating conditions. Of course, the primary challenge here is to specify the kernel parameter distribution. In some cases, this distribution can be approximated based on experimental measurements [101]. More often, such quantities are unknown, including in this thesis. The challenge is mainly due to the limited measuring capabilities from the experiment. Firstly, the spark-induced kernel exhibits variabilities for its initial energy, size, shape, momentum, and etc., which cannot be fully measured. Secondly, even when the dimensionality of K is reduced to the few most important properties, e.g., the kernel energy and velocity, such quantity is still difficult to be accurately measured. In particular, note that the kernel parameters here are the gas phase properties (e.g., energy deposited into the gas phase), and they should not be confused with nominal properties of the spark igniter discharge (e.g., electric energy during spark discharge), which are relatively easy to measure.

To overcome this difficulty, the statistical distribution of the kernel parameters is evaluated here using a calibration procedure, similar to the Bayesian technique [52, 103, 104]. Here, instead of using a full-blown Bayesian formulation, the kernel parameters K is assumed to be normally distributed with a mean and variance. Further, the likelihood function is also assumed to be Gaussian which leads to a posterior that is normally distributed as well. Since only a single uncertain variable is involved, linear regression estimates are sufficient to determine the posterior distribution. The regression-based estimation is obtained with subsets of experimental data ($P_{I,exp}$): that is, the uncertainty is determined based on one set of the experiments where a specific component of O is varying, e.g., ϕ or T_{in}.

The specific distribution calibration procedure is explained as below. The 2-D phase space of the mean and standard variation of the presumed distribution $\mu_K - \sigma_K$

is considered to be explored. At each of point in this phase space, the ignition probability $P_I(O)$ can be calculated as the convolution in Eq. 2.17, using the local normal distribution as a trail of $f(K)$ and the PCE response surface of $P_{I|K,PCE}$ as the approximation of $P_{I|K}$. The convolution calculation leads to the final ignition probability, denoted as $P_{I|E_d,Conv}$. Due to the nature of the PCE response surface, $P_{I|E_d,Conv}$ is a continuous function in the phase space of O, and its $L2$-norm error compared against the experimental dataset can be readily calculated, as

$$\delta_{Cali}(\mathcal{N}(\mu_K, \sigma_K^2)) = \frac{1}{N_{exp}} \sum_{i=1}^{N_{exp}} \sqrt{(P_{I|E_d,Conv}(O_{exp,i}; \mathcal{N}(\mu_K, \sigma_K^2)) - P_{I,exp}(O_{exp,i}))^2}, \tag{2.26}$$

where $P_{I,exp}$ is the experimental ignition probability, $O_{exp,i}$ is the operating condition where the i-th experimental measurement is conducted under, and N_{exp} is the total number of points in the subset of experimental data applied to the distribution calibration. The calibrated mean and standard variation of the presumed normal distribution is obtained as the pair of parameters that minimizes the below target function, as

$$\{\mu_{K,Cali}, \sigma_{K,Cali}^2\} = \text{argmin}(\delta_{Cali}(\mathcal{N}(\mu, \sigma^2))), \tag{2.27}$$

which can be solved numerically simply using brute force algorithms as the evaluation of $P_{I|K,conv}$ and δ_{Cali} is computationally inexpensive.

Lastly, note that the distribution calibration essentially applies the outcomes (ignition probability measurements) to determine the parameters related to energy deposition. In this sense, there is uncertainty in both the experiments and the spark igniter discharge process itself. The calibration exercise seeks the best set of parameters that "explains" the measurements, and the above optimization procedure is used to determine this set of parameters. In this context, the mean and standard deviation of spark deposit energy is not determined only by the uncertainty in the ignition estimation process, but also in the uncertainty of measurements of

ignition probability. Namely, the result of the distribution calibration is dependent on the experimental dataset applied, and so is the resulting final ignition probability. The performance of the distribution calibration can be evaluated by performing a cross-validation study, i.e., performing multiple calibration procedures using different subsets of the experimental data, and compare the resulting distributions as well the final ignition probabilities against each other. If the results are only weakly dependent on the exact experimental data set applied in the calibration, then it is validated that the uncertainties associated with the experimental measurements are low and any one of the calibrated distributions should work as a reasonable approximation of the true distribution.

2.2.4 Uncertainty Quantification

Based on the response surface constructed using the sampled data and the PCE approach, a modeled conditional ignition probability $P_{I|K,PCE}$ can be obtained. Since this quantity is subject to both sampling error (due to finite number of samples) and the PCE truncation (due to finite number of polynomials), the true conditional ignition probability can be written as

$$P_{I|K}(K,O) = P_{I|K,PCE} + \mathcal{R}_{PCE}(K,O) + \varepsilon_{Spl}(K,O), \tag{2.28}$$

which is obtained by combining Eq. 2.18 and Eq. 2.24. One may notice that Eq. 2.18 is defined at discrete positions in the phase space that have been sampled.

In Eq. 2.28, the sampling error ε_{Spl} is extended from the original term in Eq. 2.18 and becomes the continuous statistical convergence error in the continuous phase space of $K - O$. For those phase space locations that are not sampled, the physical meaning of this ε_{Spl} serves as an estimation of the sampling error if the same turbulence sampling procedure is to be performed there. Using the central limit theorem,

ε_{Spl} can be assumed normally distributed with zero mean and a variance $\sigma^2_{\varepsilon_{Spl}}$ that can be approximated as:

$$\sigma^2_{\varepsilon_{Spl}}(K,O) = \frac{P_{I|K,PCE}(K,O)(1 - P_{I|K,PCE}(K,O))}{N}, \tag{2.29}$$

where N is the number of samples used to estimate the conditional ignition probability for a given kernel energy density. In this study, this sampling error is only due to the turbulence sampling, and N denotes the number of initial turbulence flow fields used as described in Sec. 2.2.2.1.

The residual error term from the PCE expansion is of a fundamentally different nature than the statistical sampling error, in that it arises from the finite-term truncation of the polynomials. generally, the errors in the truncation reduce exponentially with the order of truncation. Typically, q between 4 and 6 is sufficient to obtain accurate results [109, 112, 113]. Here, an estimation of $\mathcal{R}_{PCE}(K,O)$ is achieved by a convergence test, i.e., by comparing the error between 2 PCE response surfaces obtained with different PCE truncation orders. The method details and results are presented in Section 3.3.1.2. Here, a result is directly provided, that in this thesis, the PCE truncation error $\mathcal{R}_{PCE}$ is by an order of magnitude lower than the sampling error ε_{Spl}.

For the convolved final ignition probability $P_{I,Conv}$, the uncertainties are evaluated for the contributions from the sampling error in the conditional ignition probability $P_{I|K}$, whereas those from the PCE truncation error are neglected, and is calculated as

$$\varepsilon_{Conv}(O) = \int \varepsilon_{Spl}(K,O) f(K)\, dK. \tag{2.30}$$

In an ideal situation, if the number of turbulence sampling, the number of PCE basis functions, and the number of experimental sampling measurements all go to infinity, then the uncertainties associated with the final ignition probability should

go to zero for both numerical modeling and experimental samplings. Under such a case, any discrepancy between the numerical and experimental data is purely due to modeling error, including both the LES forced ignition simulation and the presumed distribution of kernel parameters. In reality, none of those conditions can be achieved, and the experimental and numerical results can only be "roughly" compared by their confidence intervals. The above uncertainty quantification method is therefore important as it made such comparison available. Otherwise, comparisons made only between mean values make poor statistical sense.

2.3 Distinction between Prediction and Calibration

In the last two sections, the modeling of individual forced ignition sequences (as deterministic procedures given the initial and boundary conditions) and the ignition probability were proposed. As part of this modeling, many of the physical processes as well as quantities are evaluated (or estimated). In this regard, a first-principles calculation of relight is not feasible since this will require complete resolution of the inflow conditions as well as the spark discharge process. In order to keep the modeling tractable, certain aspects of the problem are directly modeled, while other components are treated as uncertain variables.

The following distinctions are made

- An individual LES realization consists of injection of a spark kernel and its evolution in turbulent flow, with the end result of either a stable flame or extinction. The associated LES models, including the tabulation approach, constitute physics-based models that may be individually validated against experiments.

- The spark kernel energy is taken to an uncertain parameter, in that the total energy deposited into the spark is variable from one shot to the next. This kernel energy is assumed to have a distribution, with a mean and variance, and

characterized by a normal process. It is also assumed that this distribution is independent of the operating parameters, including turbulence levels, equivalence ratio, and other flow related parameters. Since the energy deposition occurs in a region that is outside of the main flow, this assumption is valid. As a result, the distribution of spark energy is calibrated using methane/air system, and is re-used for alternative jet fuels.

- The inflow turbulence is a high-dimensional process, and cannot be fully described by the filtered velocity field imposed at the inlet boundary. As a result, there is variability in the flow field, induced through initial conditions that exist at the time of spark discharge. For this reason, the initial state of the fluid is treated as an irreducible uncertainty. The LES calculations are carried out in such a way that an ensemble of simulations represents the various initial states present in the flow.

- The prediction of ignition probability then combines the individual LES realization and associated models, spark energy calibration, and the variability introduced by initial conditions.

A detailed list of modeling setup is also later provided in Tab. 3.1.2, where the consistency can be directly evaluated among different cases.

2.4 Summary

In this chapter, the developed computational platform for predicting turbulent non-premixed forced ignition in altitude relight is described in full detail. The modeling procedure is comprehensive and covers all common topics/challenges are potentially encountered in the numerical prediction of such type of problems, providing an understanding of the forced ignition physics from a modeling aspect. The main highlights are as follows. (a) In Sec. 2.1.1, for turbulent non-premixed forced ignition

modeling, capturing the entire process from reaction initiation to flame stabilization is important, the early-stage reaction initiation is often not included in previous combustion models, and therefore cannot properly handle the effects such as non-localized ignitions. Here, by applying HR calculations to model the early stage kernel stabilization and FPVA approach to model the later stage flame propagation, the complete forced ignition process is included in the combustion model. (b) In Sec. 2.2, when estimating ignition probability, the stochasticity contributed from both turbulence and the spark discharged should be quantified, while previous estimations mostly predict ignition success and failure only due to turbulence disturbances, the probability estimation strategy developed here takes both factors into account and also provides a rigorous quantification of the modeling uncertainty. (c) The computational framework development is formulated in the most generic format possible. The only configuration-specific treatment is the coupling between the kernel and turbulent flow field (Sec. 2.1.3), which is nonetheless based on a popular configuration of aircraft spark igniter and can also be easily adapted to simulate other igniter configurations.

CHAPTER III

Model Validation

In this chapter, the computational framework developed in Chap. II is validated using a model forced ignition rig that represents turbulent non-premixed forced ignition in altitude relight. The validation is performed for both the LES simulation of individual forced ignition process and the numerical prediction of ignition probability, each carried out in the two forms of (a) sensitivity test or cross-validation of the applied modeling parameters; (b) comparison with DNS or experimental data. Most of the results presented in this chapter are collected from the early studies of Ref. [35, 114–116].

3.1 Target Configuration

3.1.1 Stratified Forced Ignition Rig

The flow configuration used here is based on the stratified forced ignition rig at the Georgia Institute of Technology [5], as schematically shown in Fig. 3.1. On the left plane, the inflow is split into two streams by a splitter plate: the kernel flow (lower) and the main flow (upper). The pre-vaporized fuel is injected from three fuel bars fabricated from perforated steel tubing into the main flow, whereas kernel flow is isolated from fuel mixing and remains as pure air. The configuration can also be separated into two sections in the streamwise direction by the location of the splitter

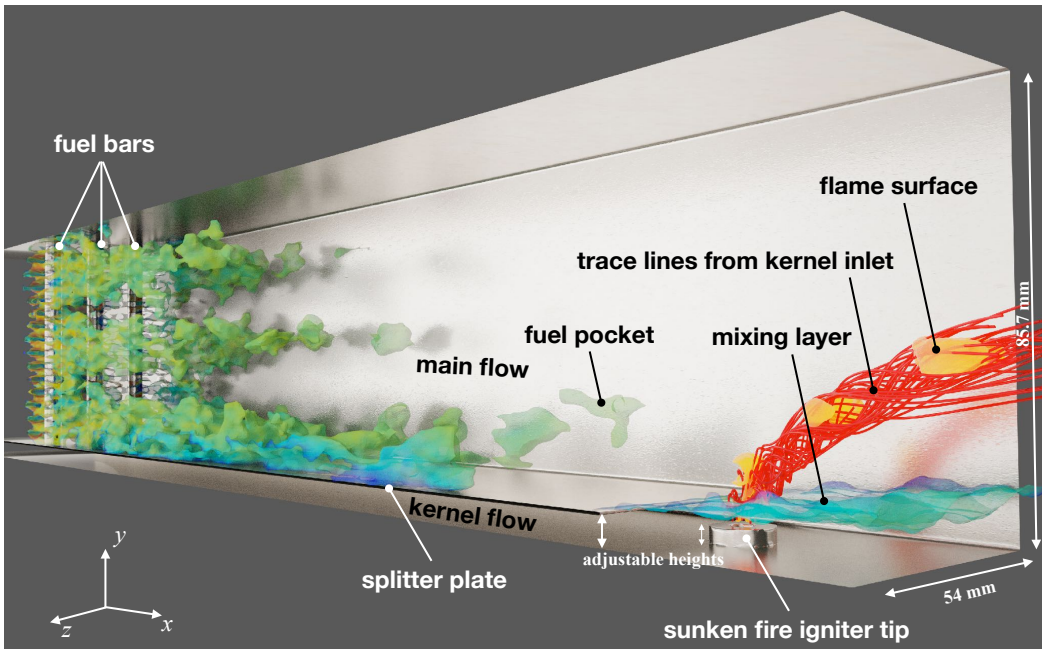

Figure 3.1: Configuration of the forced ignition rig developed at Georgia Institute of Technology. The flow direction is from left to right.

plate trailing edge - the upstream is the fuel-mixing section and the downstream is the ignition test section. The length of the fuel mixing section is designed to be sufficient such that some level of mixing has been achieved [115]. However, the mixture is not homogeneous and there exist spatial-temporal fluctuations of equivalence ratio when the main flow enters the ignition test section. Inside the ignition test section, the kernel flow and the main flow meets with a mixing layer formed in between them. The mixing layer is almost shear-free as the kernel flow and the mean flow are introduced with the same bulk velocity. The sunken-fire igniter introduced in Sec. 2.1.3 is placed at the bottom of the ignition test section. The spark is discharged within a cavity recessed from the igniter top surface, and the thermal expansion inside the cavity forces the kernel to be ejected into the kernel flow. The kernel then transits through the non-flammable kernel flow and eventually enters the fuel-seeded main flow where chemical reactions can occur. Depending on the initial conditions of the spark and the flow field, the kernel can either dissipate (ignition failure) or sustain and develop

into a propagating turbulent flame front (ignition success).

The configuration is representative of the forced ignition process that typically takes place in aircraft engines during relight. Particularly, the kernel flow here represents the non-flammable stream that prevents the spark-induced kernel from an immediate reaction after the spark discharge and is critical for reproducing the non-localized ignitions. The transit time it takes for the kernel to reach the mixing layer $\tau_{transit}$ can be controlled by adjusting the height of the splitter plate and the intrusion depth of the igniter tip into the flow domain. The definition of a successful ignition applied in the experimental study [5] is that the flame front sustains and expands for a certain time period after the initial spark discharge (2 ms), measured by the OH^* signal. This definition is slightly less stringent than those applied in other previous studies [2, 27] where the flame needs to be fully stabilized. Because the experimental operating conditions applied here all lead to an effective turbulent flame speed below the main flow bulk velocity, the flame front eventually convects downstream even in a successful ignition. Nonetheless, the ignitions here have reached step 3 of the non-localized ignition process (defined in Sec. 1.2.2.2), most likely in the form of 3A and 3B as the inflow here is fuel-stratified instead of completely non-premixed. This corresponds to an early phase 3 of the turbulent forced ignition problem (defined in Sec. 1.2.2.1), which is a fairly mature ignition process despite being not fully complete. The corresponding numerical definition of ignition success/failure is introduced in the following section.

3.1.2 Numerical Cases & Setups

To reduce the computational cost, the simulation domain only includes the downstream ignition test section of the stratified forced ignition rig (Fig. 3.2). Here, the origin of the physical coordinate system is positioned at the projection of the igniter spark gap center point onto the facility floor plane. Temporarily and spatially varying

profiles of turbulent velocity and mixture fraction are enforced at the domain inlet to represent the upstream turbulent flow development and fuel mixing. These profiles are obtained from an auxiliary cold flow LES of the upstream fuel-mixing section [115] and can be reused for similar operating conditions. The inlet enthalpy boundary conditions apply a time-space-dependent Dirichlet boundary conditions with value inversely looked-up from the table using the target inflow temperature value. The solid walls enforce a no-slip boundary condition for velocity and an adiabatic boundary condition for enthalpy. The boundary treatments at the kernel inlet have been explained in Sec. 2.1.3.2.

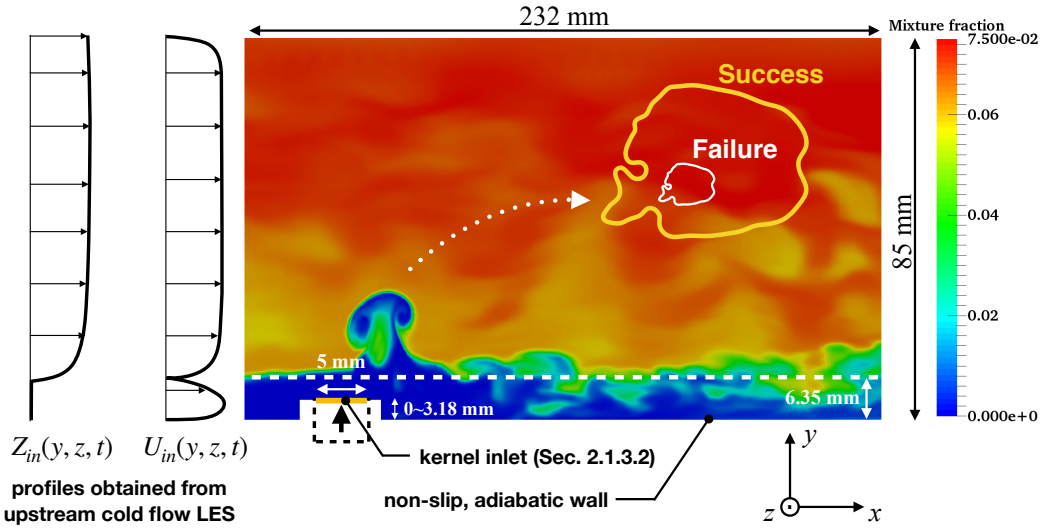

Figure 3.2: Schematic of the simulation domain and the applied boundary conditions. The background contour is colored by the mixture fraction field depicting the moment when a kernel just enters the main flow. The kernel edge (yellow and white lines) plotted here are artificial results only for demonstration purposes.

To better explain the applied modeling parameters and setups, the numerical test cases are introduced first. Based on the fuel type and geometrical setups used in the corresponding experimental studies, the numerical cases can be categorized into two main groups, as listed Tab. 3.1. Group 1 involves the small molecule fuel of CH_4, which is to investigate the model performances under varying inflow temperatures

and global equivalence ratios. Group 2 contains three cases, each using a different realistic jet fuel, which is to investigate the model performance under varying fuel blends. For all cases, the operating pressure is 1 atm. Within each case, one single component of the operating conditions vector O is varied (i.e., highlighted by square brackets in Tab. 3.1), and a response surface of the conditional ignition probability $P_{I|K}$ is reconstructed in the corresponding phase space, as explained in Sec. 2.2.2.2.

Table 3.1: Summary of operating conditions of numerical cases

Group	Case ID	Fuel	Inflow temperature	Global equiv. ratio
1	I	CH4	[375, 425, 455, 485, 525] K	1.1
	II	CH4	455 K	[0.9, 1.1, 1.2, 1.3, 1.4]
2	III	C1	475 K	[0.6, 0.7, 0.8]
	IV	A2	475 K	[0.6, 0.7, 0.8]
	V	C5	475 K	[0.6, 0.7, 0.8]

To be consistent with the experiments, the definition of ignition success/failure is based on the kernel volume, measured as the total volume of computational cells with temperature higher than 1500 K. Successful ignition causes this volume to increase in the time range $2-3$ ms after the spark.

The applied simulation setups and modeling parameters are mostly dependent on the group of study, as summarized in Tab. 3.1.2. Unless otherwise mentioned, the numerical results presented in this chapter are obtained with these setups listed in the table. The choice of each modeling parameter will be discussed below in the sections dealing with the corresponding simiulations. Here, the differences in the operating conditions between the two study groups are clarified. In Group 1, the igniter top surface is flush-mounted on the facility floor plane, whereas in Group 2, the igniter top surface is raised 3.18 mm above the floor plane, as illustrated in Fig. 3.2. Besides, the main flow bulk velocity is also different in these two groups of studies. Experimentally, the main reason for these adjustments is to increase the ignitability of the jet fuels in Group 2 [6]. As a result, the velocity profile enforced at the kernel inlet uses different peak values for the two groups of studies. This peak velocity value

is the only one modeling parameter that is particularly "tuned" in this thesis, which is nonetheless due to the nature of the developed kernel initialization strategy: there is less of a direct physical justification of the enforced kernel inlet velocity except to be able to reproduce the experimental kernel trajectory. Apart from this choice, all the other modeling parameters are applied with identical/consistent setups across all the numerical cases within the two groups of studies.

An evaluation of computational cost is provided in Section 3.3.3.

3.2 Performance of the Forced Ignition LES Simulation

This section validates the developed LES simulation capabilities in predicting the target forced ignition problem. First, the performance of the developed coupling strategy between the kernel and the turbulent flow field is evaluated, by comparing the predicted kernel shape and vortex dynamics against experimental schlieren data. Then, the variability of the predicted forced ignition outcomes are interrogated, by evaluating the sensitivity of the simulation outputs w.r.t. the inputs of turbulence and kernel parameters, and the modeling parameter that determines the partition between the HR and FPVA tabulations. Last, the LES simulation capabilities are evaluated for capturing the fundamental physics of the forced ignition process, by comparing the simulated forced ignition process with DNS and experimental data.

3.2.1 Reproducing the Pulsing Dynamics of the Kernel

For the geometrical setups in both groups, using the nominal values of $\{E_d = 1.25$ J, $V_{ker} = 0.25$ cm$^3, \tau_{ker} = 50$ μ s$\}$ and U_{ker} as listed in Tab. 3.1.2, the kernel injection process was simulated. Results are first compared with experimental schlieren images, shown in Fig. 3.3. It can be seen that the injection method reproduces the kernel shapes and locations reasonably well throughout the time sequence for both groups of studies. Further, quantitative validation can be made by comparing the

Table 3.2: Nominal simulation setups and modeling parameters.

Components	Prameters	Group 1	Group 2
Operating conditions	Igniter surface height	0 mm	3.18 mm
	Inflow bulk velocity	20 ± 2 (m/s)	12 ± 0.2 (m/s)
Combustion model	Chem. mech.	GRI 3.0 [117]	HyChem [118–121]
	HR/FPVA partition[a]	$H_{HR,min} = H(T_a)$, $H_{FPVA,max} = H(T_p)$	$H_{HR,min} = H(T_a)$, $H_{FPVA,max} = H(T_p)$
Mesh[b]	Finest resolution	$2/15\ r_{igniter}$	$2/15\ r_{igniter}$
	Total mesh size	3.9 million	2 million
Turbulence modeling	SGS viscosity	dyn. Smagorinsky	dyn. Smagorinsky
	Non-dimensional constants	$Pr_T = 0.72$, $Sc_T = 0.7$	$Pr_T = 0.72$, $Sc_T = 0.7$
Kernel initialization	Enthalpy profile	H_{ker} from Eq. 2.14, $V_{cav} = 0.25$ cm^3	H_{ker} from Eq. 2.14, $V_{cav} = 0.25$ cm^3
	Velocity profile	$U_{ker} = 300$ m/s, $\tau_{ker} = 50\ \mu$s	$U_{ker} = 200$ m/s, $\tau_{ker} = 50\ \mu$s
Probability estimation	Turbulence sampling	$N_{Spl} = 15$	$N_{Spl} = 15$
	Spark deposit energy sampling[c]	$E_{d,Spl} = 1 \sim 1.75$ J, $\Delta E_{d,Spl} = 0.01$ J	$E_{d,Spl} = 1 \sim 2.5$ J, $\Delta E_{d,Spl} = 0.01$ J
	PCE truncation order	$q = 6$	$q = 6$
	Normal distribution of spark deposit energy	$\mu_{E_d} = 1.24$ J, $\sigma_{E_d} = 0.14$ J	$\mu_{E_d} = 1.24$ J, $\sigma_{E_d} = 0.14$ J

[a] The HR and FPVA tabulation is partitioned based on enthalpy, which is translated from the unburnt temperature of the canonical reactions. Here, T_a denotes the autoignition temperature and T_p denotes the partial extinction temperature. Details can be found in Sec. 2.1.1.3.

[b] After Group 1 studies, it is determined that the higher domain region ($y > 0.5$ m) can be trimmed off. Therefore, the total number of control volume in Group 2 is about half of that in Group 1. The mesh resolution remains unchanged, which applies 15 points across the kernel inlet diameter ($2r_{igniter}$).

[c] The spark deposit energy E_d is reduced from the kernel parameters K (Sec. 3.2.2.2). The sampling range in the E_d-space can be arbitrarily extended until the resulting probability $P_{I|E_d,Spl}$ goes to 0/1 at the lower/upper bound. The exact lower/upper value here is far less important than the sampling resolution $\Delta E_{d,Spl}$, which is identical for the two study groups.

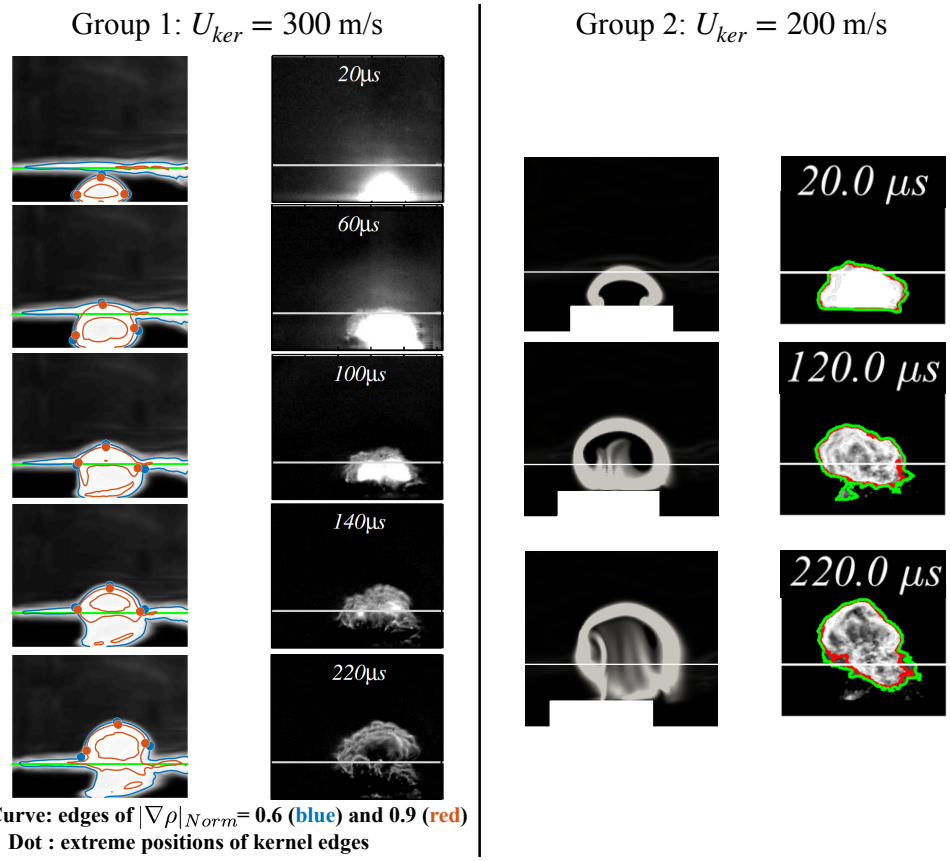

Figure 3.3: Time-series of kernel injection. Within each group, the left column is numerical schlieren, and the right column is experiment schlieren [5, 6]. For Group 1, the numerical schlieren is obtained with line-of-sight integration. After confirming the numerical kernel edge is not affected by out-of-plane density variations, the numerical schlieren is simply calculated at the mid-plane for Group 2.

kernel diameter and the topmost location of the kernel as a function of time. The extreme positions that mark the kernel edge are defined using a numerical edge tracking algorithm and are obtained with different threshold values. Figure 3.4 shows that irrespective of the metric chosen to get these quantities, the simulations predict the observed trends in the experiments reasonably well.

Further investigation is conducted into the kernel vortex roll-up dynamics and fuel mixing after the kernel enters the main flow. As the kernel is ejected into a crossflow instead of a stationary outer flow, the flow dynamics here features a pulse-jet-in-

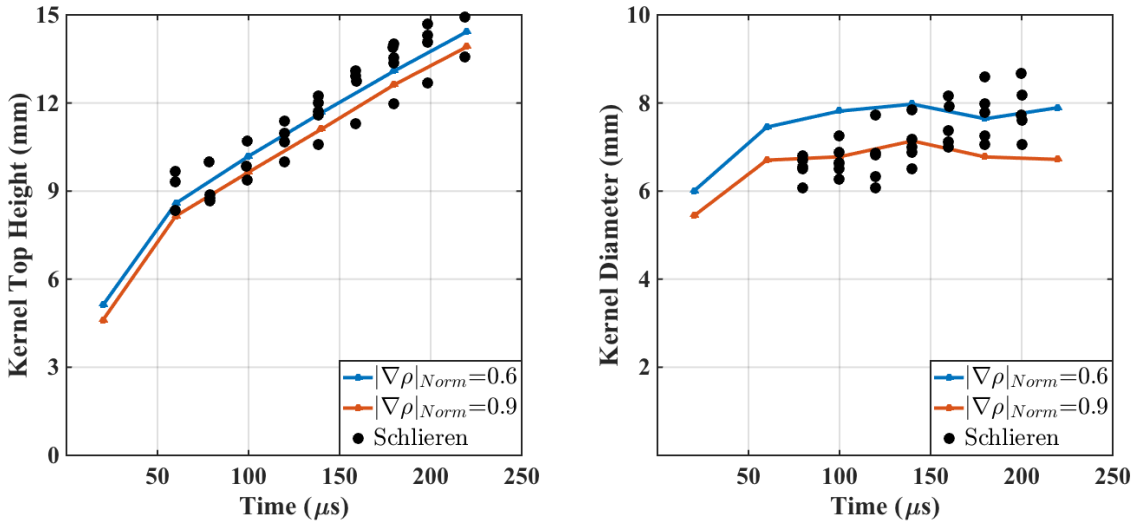

Figure 3.4: Time history of kernel top edge vertical distance from the base wall and kernel diameter. The numerical results are obtained using extreme positions highlighted in Fig. 3.4.

crossflow (PJICF) configuration. Prior studies of PJICF [7] showed that the kernel evolution is strongly dependent on the formation of vortex rings at the leading edge of the jet. The structure of these rings depends on non-dimensional parameters given by the velocity ratio ($r = U_{ker}/U_{in}$) and stroke ratio ($L/D = U_{ker}\tau_{ker}/(2r_{igniter})$), where U_{in} is the inflow bulk velocity. A regime diagram defined based on these two non-dimensional parameters is shown in Fig. 3.5. For the kernel initialization applied here, the velocity ratio and stroke ratio are respectively $r = 15$ and $L/D = 3$ for Group 1 studies, and $r = 16.7$ and $L/D = 2$ for Group 2 studies. Under both conditions, the PJICF should fall into the regime of "discrete vortex rings". A demonstration of the simulated PJICF kernel flow patterns are plotted in Fig. 3.6, along with experimental schileren and DNS data. The discrete vortex ring has a short trailing vortex column, the length of which is directly proportional to the stroke ratio. Also, the vortex ring slightly tilted upstream as it evolves, indicated by the two vorticity iso-lines (white solid) in the LES results, with the one on the leeward side (i.e., the right side of the

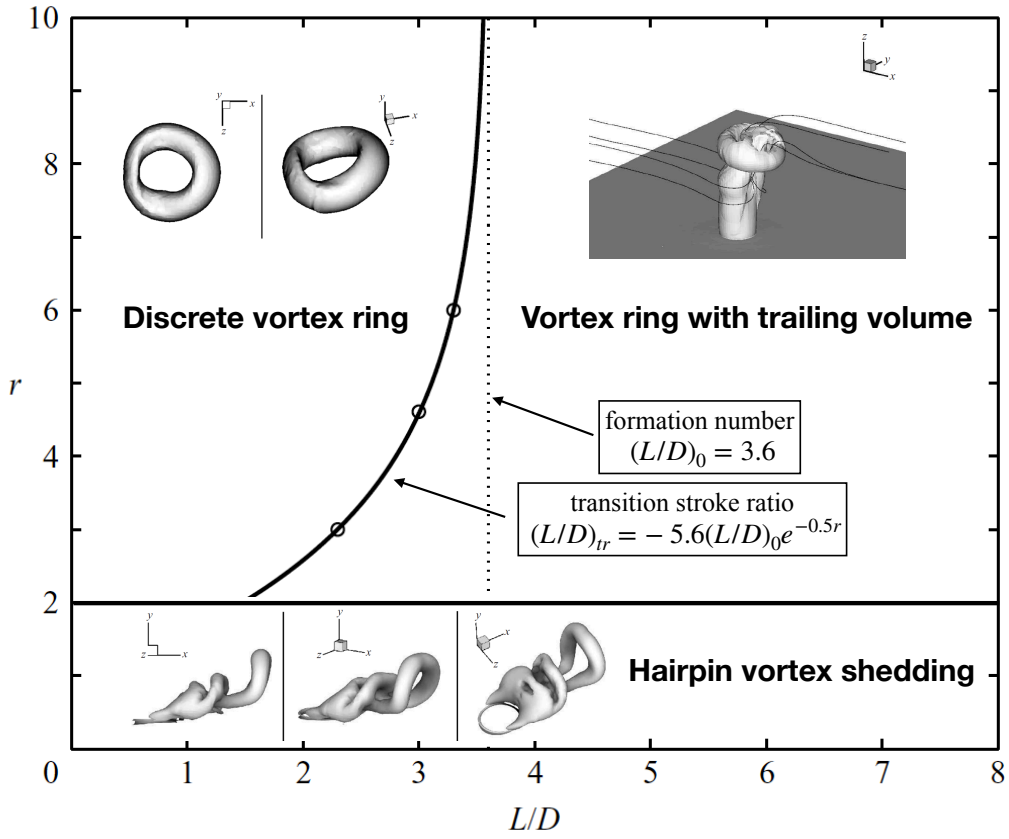

Figure 3.5: Regime diagram of different PJICF flow structures and entrainment characteristics. The diagram is reproduced from [7], where the subplots are typical vorticity iso-surfaces.

view in Fig. 3.6) rose slightly faster than that on the windward side. This tilting momentum comes from the Kutta-Joukowski lift that is induced by the relative flow motions between the crossflow and vortex circulation. The available experimental schlieren images show the kernel edge up to 0.32 ms, which appears to exhibit the same trend of upstream tilting, while further measurements of the velocity field await. Since the vortex structure here features a 3-D ring, the concept of counter-rotating vortex pair (CVP) can be introduced as a 2-D description of such structure. It should be clarified that there are two versions of CVPs in the PJICF problem here: the CVP in the mid-spanwise plane (side view) and the CVP in a cross-section plane (front view), both of which are later used to facilitate the discussions of the forced ignition

process.

In terms of fuel-mixing, the mixture fraction field evolution is presented in Fig. 3.6 by the colored contours, where it can be seen that the scalar entrainment is mainly achieved by the vortex ring bottom being rolled-up into the ring center. The entrainment is barely observed at $t = 0.36$ ms and increases rapidly with time, which is believed to correspond to the first cycle of vortex roll-up after the kernel trailing edge enters the main flow. Besides, throughout the process, the windward side of the vortex ring is better mixed than the leeward side, which is interesting as the leeward side of the kernel should have the advantage of early access to the main flow due to the upstream tilting. Similar fuel-mixing behavior is also found in the DNS study by Sau and Mahesh [7]. In their study, it is explained that the flow stretching effect plays an important role to enhance the scalar mixing, which is more prominent on the windward side than the leeward side.

As a quick summary, the applied kernel coupling strategy is able to reproduce the size and trajectory of the ejected kernel. Besides, the LES is able to correctly capture the kernel vortex dynamics and fuel mixing of the PJICF in the target configuration.

3.2.2 Reproducing the Variability of Forced Ignition Outcomes

3.2.2.1 Sensitivity to turbulence

To study how turbulence affects the forced ignition process, a large number of LES forced ignition simulations are performed for operating conditions similar to Group 2 studies later in Chapter IV. Here, a preview of the simulation results is provided in Fig. 3.7, where the time histories of the maximum field value of the progress variable are plotted for the forced ignition processes. The simulations here are initialized with the same kernel status but different initial turbulent flow fields, which isolates the turbulence effects. It can be seen that the bifurcation between ignition success and failure cannot be determined until reaching a later stage of the ignition process. In

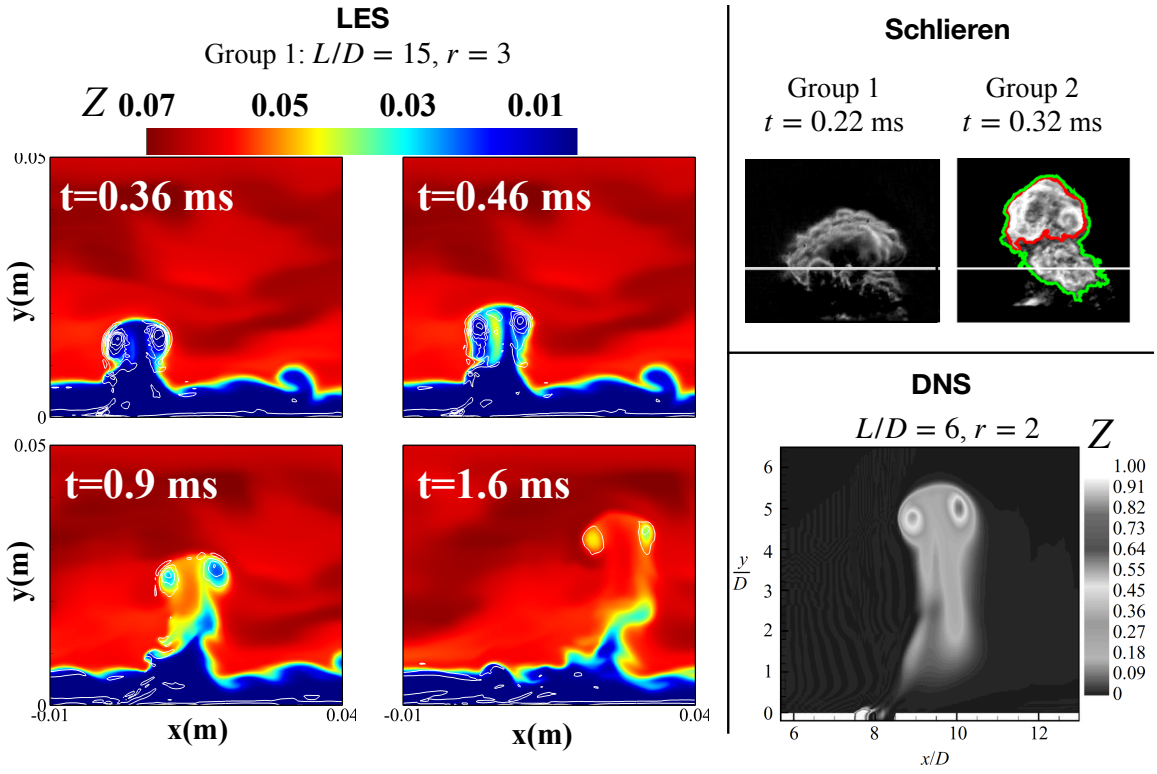

Figure 3.6: Left - LES time series of vortex evolution and scalar mixing for a kernel PJICF of Group 1 plotted at the mid-plane in the spanwise direction. Upper right - experimental schlieren images under Group 1 [5] and Group 2 [6] operating conditions. Bottom right - instantaneous DNS contour of scalar mixing of the PJICF under a similar velocity ratio and stroke ratio [7].

particular, at the early stage of the ignition process ($0-1$ ms), despite the maximum C values in the successful ignitions being statistically greater than those in the failed ignition, the trajectories of success and failures can still cross path at a later ignition stage ($1-3$ ms). This observation suggests that turbulence is playing an active role that affects the ignition outcome throughout the ignition process, i.e., a forced ignition trajectory that initially develops towards ignition can be quenched later due to turbulence strain. The mechanisms that cause success or failure of ignition will be discussed in detail latr (Chap. IV, Sec. 4.1). Here, it is simply demonstrated that the simulated forced ignition outcomes are sensitive to the initial turbulent flow field.

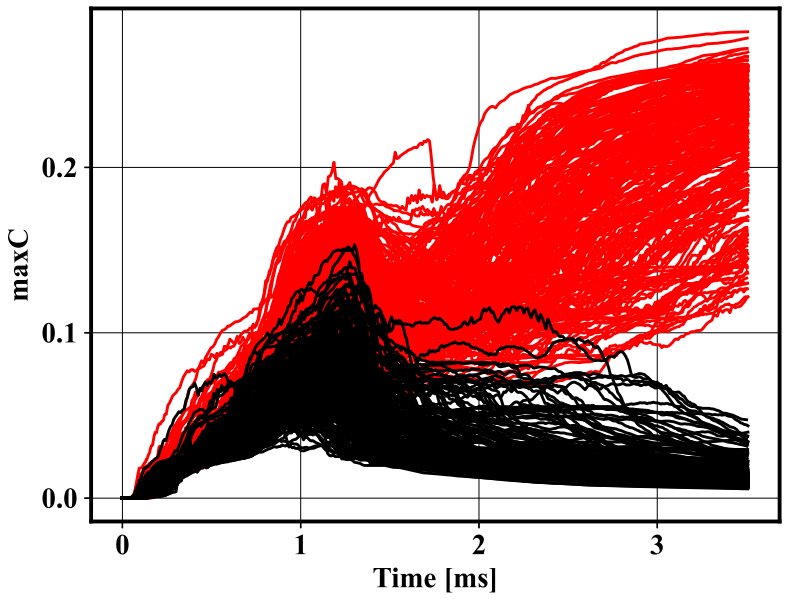

Figure 3.7: Time histories of maximum progress variable obtained from a total number of 467 LES forced ignition simulations: red - successful ignition; black - failed ignition. The operating conditions are similar to Group 2 using the fuel A2 (Chapter IV, Section. 4.1).

3.2.2.2 Sensitivity to kernel parameters

While the coupling strategy between the kernel and the turbulent flow field (Sec. 2.1.3.2) uses a set of parameters defined by $K = \{E_d, V_{ker}, \tau_{ker}, U_{ker}\}$, some of these parameters may be correlated. In order to further reduce the phase-space of uncertain variables, it is useful to consider these correlations. For example, the energy of the ejected kernel is proportional to both E_d and V_{ker}, and the PJICF stroke ratio (the length of the momentum pulsing jet) is proportional to both U_{ker} and τ_{ker}. As a starting point, consider the spark deposit energy E_d and the nominal kernel velocity U_{ker} as the two independent parameters to be investigated here. The other two parameters $\{V_{ker}, \tau_{ker}\}$ are fixed at the nominal values suggested in Sec. 2.1.3.2.

While it can be postulated that increasing the deposition energy will increase the probability of ignition, the dependence of the ignition event on U_{ker} is less direct. For instance, higher velocities will cause the kernel to reach the main flow faster, but

will also increase kernel air entrainment leading to dissipation of the high-enthalpy gases (turbulence stretch [7]) and flame quenching (turbulent strain). To further understand the relative roles of these parameters, a series of cases varying $\{E_d, U_{ker}\}$ within two standard deviations of their nominal values of {1.24 J, 300 m/s} is under the Group 1 operating conditions. These standard deviations are set to {0.02 J, 25 (m/s)}, based on results from [5]. When all other conditions are maintained the same (in particular, the initial turbulent flow field). Note that when all other parameters are held constant, there is a clear separation between the ignition and failure regimes for each of the input variables. In other words, these events are deterministic for any given set of kernel parameters. The results are shown in Fig. 3.8.

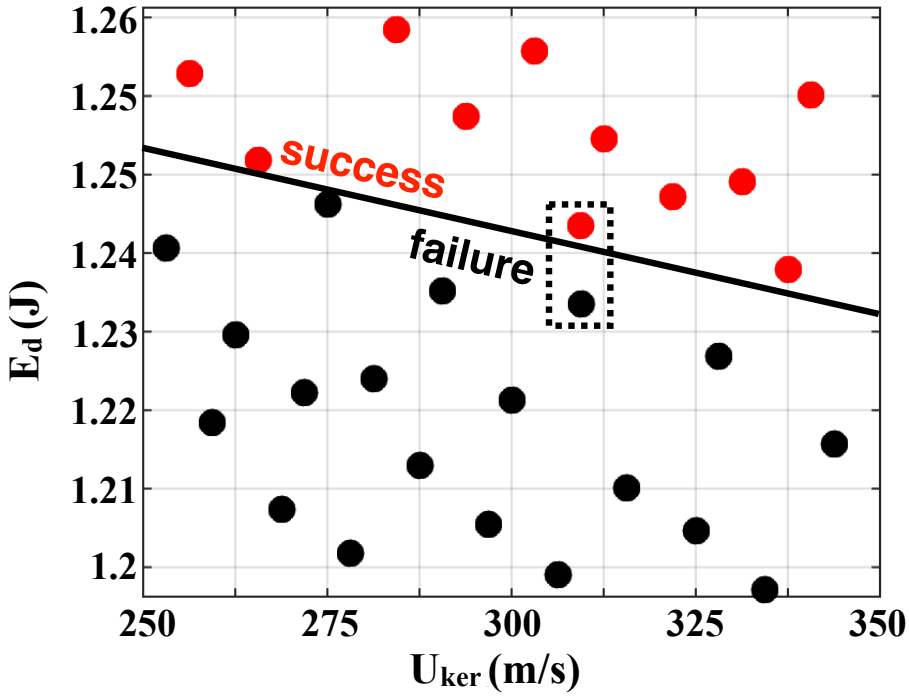

Figure 3.8: Points in the $\{E_d, U_{ker}\}$-space tested in the kernel parameter study colored by their ignition outcomes: red – successful ignition; black – failed ignition. The dashed box indicates the two cases that were applied for in-depth analysis in Section 3.2.3.1.

The model captures the impact of the velocity of the kernel as well as its energy on the ignition outcome. Specifically, based on the boundary that separates the

failed and successful ignitions, the ignition outcome is strongly dependent on the spark deposit energy E_d. Besides, there is also a weak dependency of the ignition outcome on the kernel nominal velocity, i.e., when the kernel is ejected with a higher velocity, the less amount of spark deposit energy is required to achieve a successful. This relationship between U_{ker} and ignition outcome suggests that the transit time $\tau_{transit}$ for the ejected kernel to enter the main flow (i.e., faster fuel entrainment) is the dominating mechanism over other physical effects, such as turbulent stretch and strain. This prediction is also qualitatively confirmed by experimental studies in Ref. [5], where the $\tau_{transit}$ is adjusted by setting the splitter plate to different distances above the floor plane. The experimental results showed that when $\tau_{transit}$ decreases, which is qualitatively equivalent to an increase of U_{ker} here, the forced ignition is more likely to succeed.

Lastly, note that the energy of the kernel primarily influences chemistry. Moreover, the variation in critical energy for ignition is nearly constant for a wide range of velocities, indicating that spark energy deposition is an independent factor. While there is also considerable uncertainty in the specification of injection time τ_{ker} and kernel volume V_{ker}, the previous section (Section 3.2.1) used experimental images to calibrate these values. Here, it is assumed that post-calibration, the uncertainty in these parameters is small. As a result, any uncertainty in the kernel parameters is reduced to uncertainty in E_d. In the rest of this thesis, 'K' is replaced by 'E_d', for both the variable name and the subscript.

3.2.3 Reproducing the Fundamental Physics of Forced Ignition

3.2.3.1 Numerical predictions of methane forced ignitions

In this section, two different simulations from the Group 1 studies of methane ignition are interrogated. The global equivalence ratio of the cases is $\phi = 1.1$ and the inflow temperature is $T_{in} = 455$ K. Both cases use the same initial flow field.

However, the spark deposition energy E_d is varied for the two cases by 0.8%, with $E_d = 1.2325$ J and 1.2425 J for the successful and failed ignition, respectively.

Figures 3.9 show the time evolution of an iso-surface of progress variable for the successful and failed ignition cases, respectively. For the successful case, and at early times (before 1.6 ms), the reaction front has a complex spatial structure. For reference, Fig. 3.6 discussed above corresponds to the successful ignition process here. It can be seen that the progress variable peaks inside two vertical columns (purple, 0.36 ms) that go through the vortex ring of the kernel. At later times (green, 1.6 ms), it can be seen that the flame surface occurs along the outer edges of the kernel, which corresponds to the cross-section plane CVP. In between $0.36 - 1.6$ ms, the flame surface takes various complex shapes as it tries to propagate. Interestingly, the windward part of the reaction front that initially forms at 0.9 ms is later quenched at 1.6 ms, suggesting stretch-induced quenching on the windward side of the kernel as discussed in Sec. 3.2.1. After 1.6 ms, the reaction front propagates from the kernel side edges gradually to the leeward side, and also to the windward side to form a horse-shoe shaped flame surface. Allowing the flame to further develop, the flame front will eventually encompass the entire vortex ring (not shown). For the failed ignition case, the progress variable iso-surfaces are noticeably smaller after $t = 0.9$ ms. This shows that the reaction has already been inhibited enough even before this time. After $t = 1.6$ ms the horse-shoe-shape pattern is not visible and the reaction zone gradually dissipates until complete disappearance at $t = 3.5$ ms.

To further understand the details of ignition, a Lagrangian analysis is conducted. A set of tracer particles are seeded in the flow, and the gas-phase properties seen by these particles are recorded as they move within the domain. The particles are grouped based on their recorded progress variable at an end time, taken to be $t = 3.5$ ms here. The trajectories of fluid particles grouped by the end state show interesting features. It is seen that the primary contributor for ignition success is the formation

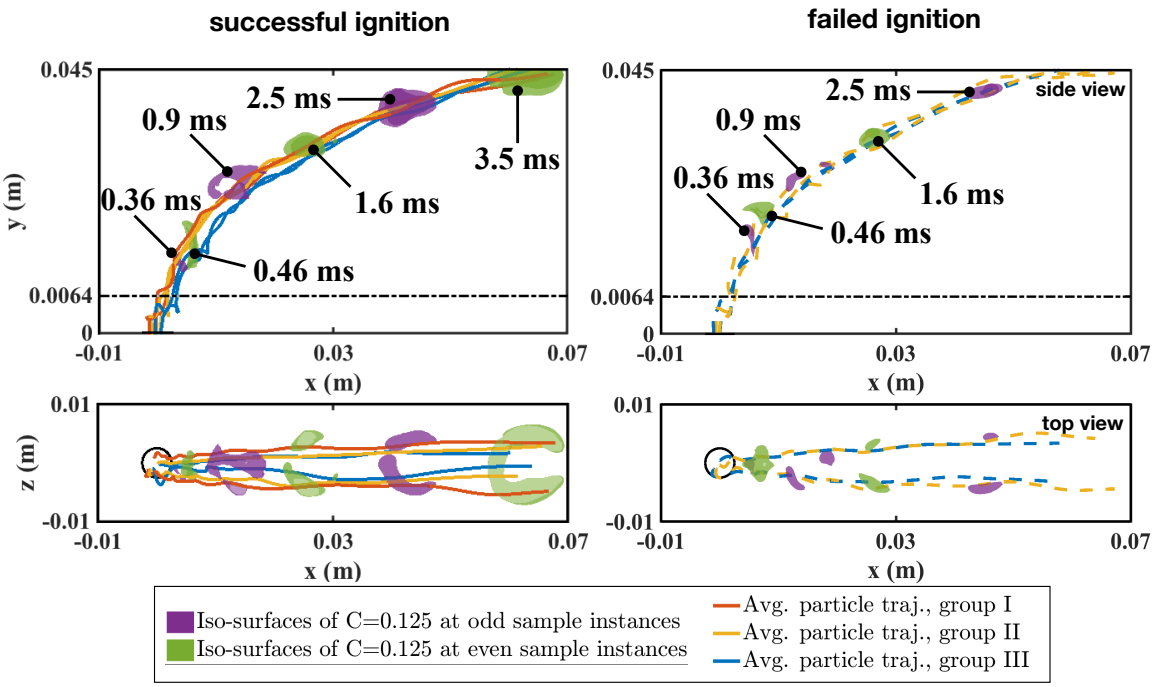

Figure 3.9: Time series of a successful (left) and failed (right) ignition kernel development under Group 1 operating conditions: averaged fluid particle trace lines conditioned on the ignition final states at $t = 3.5$ ms; group I: $C \geq 0.125$; group II: $0.05 \leq C \leq 0.125$; group III: $C \leq 0.05$; iso-surfaces of progress variable C sampled at 6 time instances. The dashed line estimates the location of the mixing layer.

of the kernel vortices as the pulsed-jet turns into the crossflow. In the failed ignition case, this outer region of highly reacted gases fails to stabilize. The side-view of the trajectories shows another feature. The igniting part of the kernel is positioned towards the windward side, which is consistent with the kernel vortex formation that is stronger on this side than the leeward side that is protected by the jet itself from the crossflow. As a result, group I trajectories are found on the windward side, while the non-igniting group III trajectories are on the leeward side. For the failed ignition case, there is not much variation in the trajectories of the different groups. This clearly indicates that the entrainment mechanism that produces the ignition pockets has failed to stabilize the reaction zone. As a result, fluid particles on the windward side

also fall in group III. Note that all the trajectories only present an average behavior of the particles.

The ignition process can also be described in terms of the flame kernel volume, marked by a region of high progress variable values. For this purpose, the volume of fluid occupied by different progress variable groups can be tracked as a function of time. Since values greater than zero are feasible only within the kernel volume, the sum of all of these group volumes will provide the total flame kernel volume. Figure 3.10 shows the evolution of the flame kernel volumes for the two cases. The flame kernel volume defined by progress variable in the range of $[0.05, 0.125]$ is formed predominantly by entrainment and signals the initial region of ignition. For both cases, this volume grows with time until $t = 0.9$ ms, which is the time when these groups reach the diffusion-limited reaction part of the process. It is seen that at this stage, excessive straining can quickly quench this initial ignition pocket. On the other hand, the successful ignition process can make the transition to a diffusion-controlled flame, which is accompanied by an increase of the flow volume with progress variable $C > 0.125$. As this high progress variable region grows in volume, it infuses higher enthalpy to the inner part of the kernel, causing a growth in the volume of the $C = [0.05, 0.125]$ group as well.

3.2.3.2 Three-phase evolution of the PJICF non-localized ignition

Combining the observed forced ignition process in the last section, along with the PJICF dynamics in Sec. 3.2.1, the PJICF non-localized ignition process here can be summarized by the following schematic in Fig 3.11, which is a 3-phase schematic similar to the previous definition [2]. Phase 1: An observable reaction is first initiated within the vortex ring center (0.36 ms) in a homogeneous reaction fashion. By Lagrangian particle trajectories, this initial reaction should be contributed from the fuel entrainment from the windward side. Phase 2: The transition period from

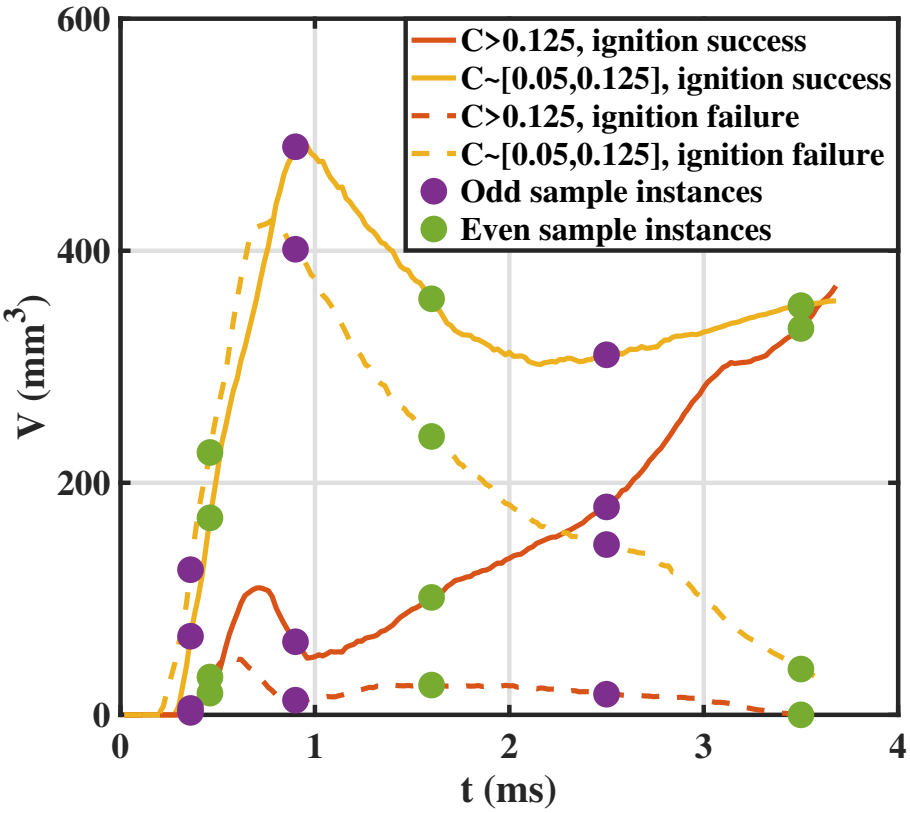

Figure 3.10: Time history of flame kernel volumes defined by different progress variable threshold values. Dots mark the sampled instances same as in Figs. 3.9.

$0.36-1.6$ ms is critical for the initial complex-shaped, small flame to stabilize. By the C iso-surface histories, there are significant flame quenching during this period on the windward side. By the flame kernel volume history, the kernel volume is gradually restored after the fast quenching of the initial ignition pocket. Phase 3: As the PJICF evolves, a propagating flame front is eventually established within the cross-section plane CVP (1.6 ms), which, shown by the C iso-surface histories, develops into a horse-shoe shaped flame for a successful ignition, or, gets dissipated for a failed ignition. Combined with the PJICF flow dynamics, the flame propagation mechanism resembles a swirling flame that evolves along the vortex ring, from the two spwanwise side edges toward the windward edge and leeward edge, and eventually encompasses

the entire vortex ring.

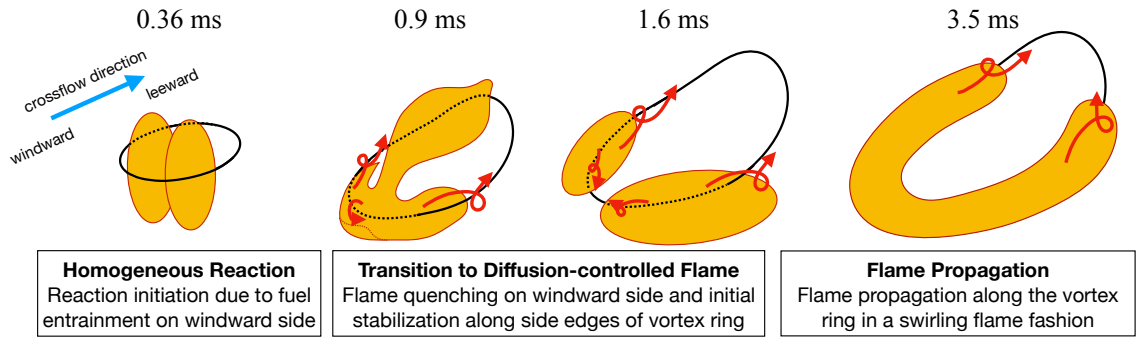

Figure 3.11: Schematic of the successful forced ignition process of the PJICF kernel: black line - PJIFC discrete vortex ring; yellow surface - flame surface; red arrow - motion of flame wrap-up and propagation. For the failed ignition, the pattern is similar while the flame surface is observably smaller and more broken since Phase 2, and eventually gets dissipated in Phase 3. Note that this is a demonstrative plot that does not represent actual size or detailed shape.

Note that while the 3-phase ignition schematic is summarized here based on a only few realizations of the ignition process. AS follow-up data-driven analysis using a large sample of LES simulations confirm that this is the most frequently encountered ignition pattern in this target configuration, which is later presented in Chapter. IV, Section. 4.1.5. In the remaining of the thesis, the term "3-phase schematic" will be used to facilitate the discussion of the forced ignition physics.

3.2.3.3 Numerical predictions of jet fuels forced ignitions

A similar analysis can be conducted for simulation results of Group 2 studies of different realistic jet fuels. A total number of three jet fuels are tested, i.e., C1, A2, and C5. The labeling of the fuels are adopted from the National Jet Fuel Combustion Program [33], where A2 refers to the conventional Jet-A fuel, which serves as the nominal case here, and C1 and C5 are synthetic jet fuels designed for testing. In the last section, the interrogated successful and failed ignition cases are chosen to have

the same initial turbulence but different spark deposit energy. Here, the cases are chosen conversely, i.e., to have the same spark deposit energy of $E_d = 1.25$ J (close to the nominal spark energy) but different initial turbulent flow fields. The cases are under the operating condition of $\phi = 0.8$.

The OH iso-surfaces of the ignition process of three realistic jet fuels are first plotted in Fig. 3.12. The time between $0.6 \sim 2.25$ ms is critical for ignition success, where a small reaction zone is generated through homogeneous ignition, leading to a ring-like OH-isosurface forming, with the high reaction progress variable concentrated at the bottom of the kernel and stabilizing on the leeward side of the jet. As time progresses, this high C region grows to encompass the entire OH isosurface. While the failed ignition cases show similar initial features (at 0.2 ms), the progress variable does not increase significantly beyond this time. Similar to Fig. 3.9, the initial flame stabilization is heavily dominated by the generation of cross-section plane CVP due to the PJICF flow dynamics. The top view shows an asymmetry in the spanwise direction, which is realization dependent, with some cases showing stronger ignition fronts on the left lobe as opposed to the right lobe. Such asymmetry can also be observed in Fig. 3.9 for Group 1 cases, despite being less prominent.

As a summary, the ignition pattern is qualitatively the same as the methane ignition, while a few differences and supplemental observations are as follows. (a) By coloring the OH iso-surface with the C-contour, the propagating flame front is found to first establish on the leeward (bottom) side of the mid-spanwise plane CVP (1.5 ms) and later grows to cover the entire flame kernel. Note that this propagating flame front should not be confused with the initial small flame surface, which is still formed from the fuel entrainment mainly on the windward side (0.6 ms). (b) The flame front shape here exhibits asymmetry that is more prominent than that in Group 1 studies. This could be due to the operating condition differences that, firstly, the igniter tip here intrudes into the domain and may disrupt the flow pattern, and

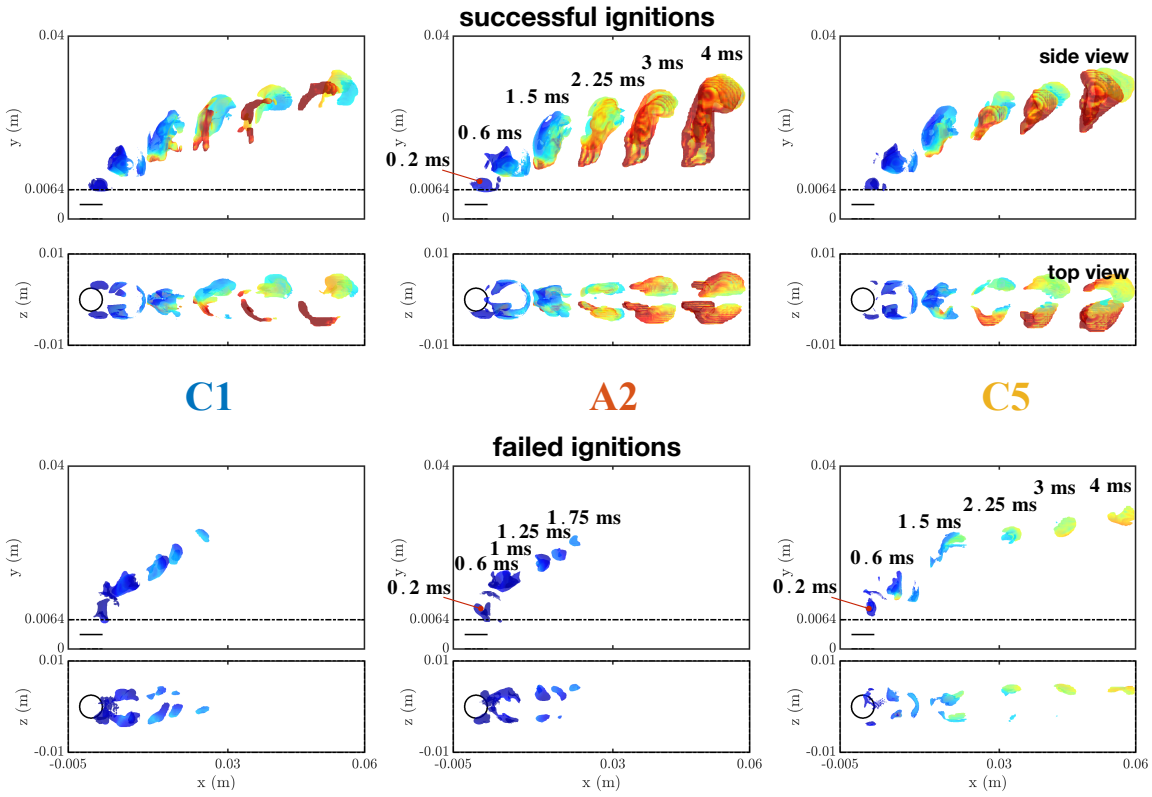

Figure 3.12: Iso-surface of OH mass fraction $Y_{OH} = 5\times10^{-4}$ (top) and $Y_{OH} = 1\times10^{-4}$ (bottom) colored by progress variable $C \sim [0, 0.075]$. Dash line estimates the location of the mixing layer.

secondly, the asymmetry may get amplified as the reaction here is more sensitive to the flow dynamics as the global equivalence ratio is lower. (c) The flame propagation here fails to form a complete horseshoe shape as it fails to propagate back to the windward side of the kernel at phase 3 of the ignition schematic. This is possibly due to the chemical properties of the realistic jet fuels being less resistant to turbulent strain and stretch on the windward side of the vortex ring as it would require a longer local residence time for the large molecule fuels to decompose and react.

Moreover, there are appreciable differences in the ignition structure for the three jet fuels. For instance, C1 shows a larger OH iso-surface compared to C5 at 0.2 ms, but the kernel occupies a smaller volume at later stages. C1 also shows regions of high

progress variable aligned with the core of the kernel, where the two counter-rotating pairs (side edges of the vortex ring) meet, compared to C5, which is similar in structure to A2. In the failed ignition case, C5 exhibits an appreciable reaction even at later times, but the kernel volume does not grow, indicating that the homogeneous reactions have not transitioned to a relatively low strain flame region. On the other hand, A2 and C1 fail similarly, with the progress variable dissipating due to entrainment of the colder fuel-air mixture. However, note that the above results are realization dependent and should not be over-generalized at this point.

To better understand the fuel effects, the kernel composition is probed, again, using Lagrangian particles. The particles are initialized within the kernel ($H \sim 2\times10^6$ J/kg) when its top edge reaches the main flow. For each LES simulation, a total of 1200 particles are tracked. Multiple LES realizations ($N_{Spl} = 15$) are simulated for each operation condition, and here the results are shown for the resulting successful ignitions. The individual particle trajectories from one of the ignition samples are first plotted in the physical domain, shown in Fig. 3.13. In contrary to Fig. 3.9 where the trajectories are shown for the grouped particles, here, the flow vortex structures are better revealed by the individual trajectories especially for the two side edges of the vortex ring (see bottom right subplot in Fig. 3.13). This provides a more straightforward impression of where the propagating flame front is initially established.

The average of the particle trajectories are then re-plotted in the phase space of interest, as shown in Fig. 3.14, the uncertainty bandwidth is not shown as the total number of sample trajectories are sufficiently large to distinguish between the averaged trajectories here. In the left plot, the trajectories are interrogated in the 3D phase space of $H - \phi - C$. The projection onto the $H - \phi$ space is identical for all cases, indicating that mixing is nearly independent of the fuel. The differences between fuels are seen mainly in the variations of progress variable as a function of

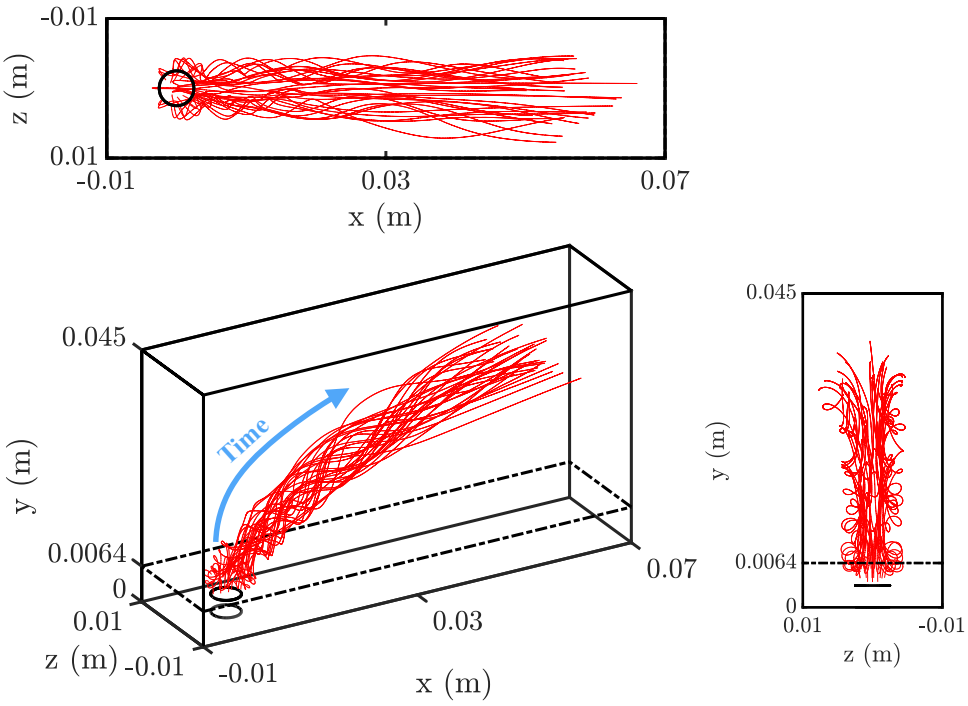

Figure 3.13: Physical space trajectories of mass-less Lagrangian particles from an LES forced ignition simulation in Group 2 studies. Plotted every 50^{th} particles.

time. From the time histories of the progress variable C and the reaction rate $\dot{\omega}_C$, a spike of $\dot{\omega}_C$ occurs about 0.2 ms, which leads to the first increment of C. This should correspond to phase 1 of the forced ignition schematic introduced in the last section. The reaction is then sharply suppressed after the initial spike, suggesting a fall-off of reaction rate due to the entrainment of colder flow and turbulent stretch. The reactions then accelerate after the initial reduction. This period corresponds to phase 2 of the forced ignition process. During this transition period, it can be seen that the C5 fuel exhibits the fastest restoration of $\dot{\omega}_C$, while the C1 fuel exhibits a restored value of $\dot{\omega}_C$ that is significantly lower than A2 and C5. After about 2 ms, the reaction rates reach a plateau, indicating the transition from homogeneous reaction to diffusion-controlled flame, which corresponds to phase 3 of the forced ignition process.

Again, the C1 fuel here exhibits a much lower reaction rate than the A2 and C5 fuel. Figure 3.13 also shows the time histories of two of the major pyrolysis species. The

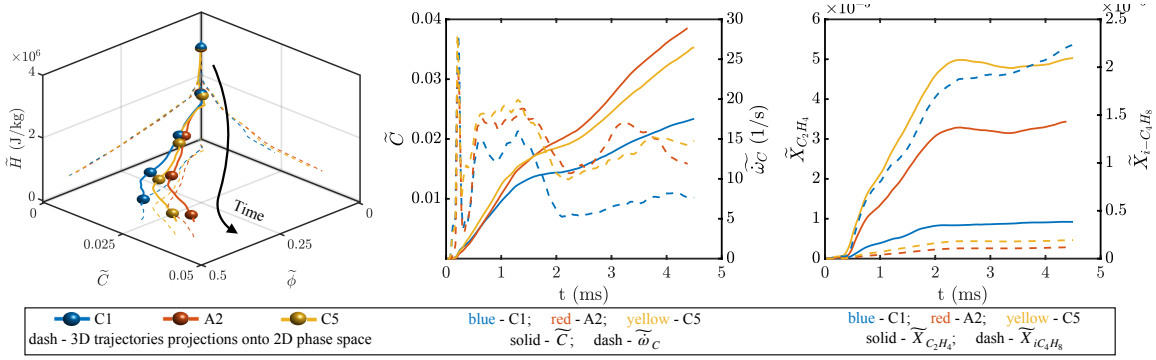

Figure 3.14: Ensemble-averaged phase space particle trajectories collected from all successful ignition simulations in Group 2 studies at $\phi = 0.8$ and $E_d = 1.25$ J.

main species is found to be C_2H_4 for A2 and C5, and i-C_4H_8 for C1. As i-C_4H_8 takes a much longer time than C_2H_4 to be oxidized [94], this chemical difference explains the overall weaker ignition strength of the C1 fuel, although pyrolysis products of C1 are generated at roughly the same rate as that for C5.

A summary of the fuel effects is as follows. Overall, C1 fuel exhibits a considerably weaker ignition process compared to A2 and C5. Fluid trajectory analysis reveals that the ignition process itself did not affect the fuel-air entrainment into the kernel. Hence, the observed differences come mainly from the interaction of the chemical processes with the particular trajectory in phase space introduced by the boundary and initial conditions. Specifically, the progress variable histories of the three fuels are qualitatively the same while only different in terms of the magnitude, and the restoration of reaction rate from the initial reaction fall-off is critical for successful ignitions. In this regard, C1 exhibits a lower reaction rate the A2 and C5, possibly due to producing pyrolysis products that do not oxidize easily.

3.2.3.4 Numerical predictions compared against DNS and Experiment

Although forced ignition has been sparsely studied numerically, Rieth *et al.* [8] provided a DNS study under the Group 1 operating conditions, i.e., methane/air forced ignition under ambient pressure. The results are used here for a qualitative comparison, as only preliminary results are available in Ref. [8]. The OH contour at the domain spanwise mid-plane is plotted in Fig. 3.15. The DNS ignition process is available for up to 600 μs, which corresponds to phase 1 and early phase 2 of the forced ignition process. The OH evolution demonstrates how the reaction is first initiated from a side view. At about 100 μs, which is the estimated time for the kernel to reach the mixing layer ($\tau_{transit}$), OH is first generated at the top edge of the kernel. The fuel mixing here is achieved via molecular diffusion across the kernel surface. At this point, the OH concentration appears to be very low. The exact magnitude of the OH peak mole fraction is not directly comparable between the DNS and LES results and is possibly very sensitive to the particular time instance chosen for the plotting relative to the local ignition delay time, at least for the case of the LES results (e.g., at 100 μs, the magnitude of the LES OH peak mole fraction becomes 1×10^{-5}). As the kernel further enters the main flow, the OH layer is wrapped up around its edge. This demonstrates that the forced ignition mode here is essentially a homogeneous reaction under high unburnt temperature, i.e., the reaction closely follows the fuel mixing process. At 600 μs, the fuel mixing layer is fully entrained into the kernel around the vortex pairs. While the exact velocity ratio r is unclear for the DNS study, the kernel is also tilted towards the windward direction.

The LES simulation predicts qualitatively the same process. The main difference is in the exact time instance/peak OH mole fraction when the comparable patterns are observed, which is acceptable as the operating conditions are not necessarily the same, and kernel initialization setups (e.g., the radius of kernel inlet and the enforced velocity profile) are different for the two simulations. Another difference is the shape

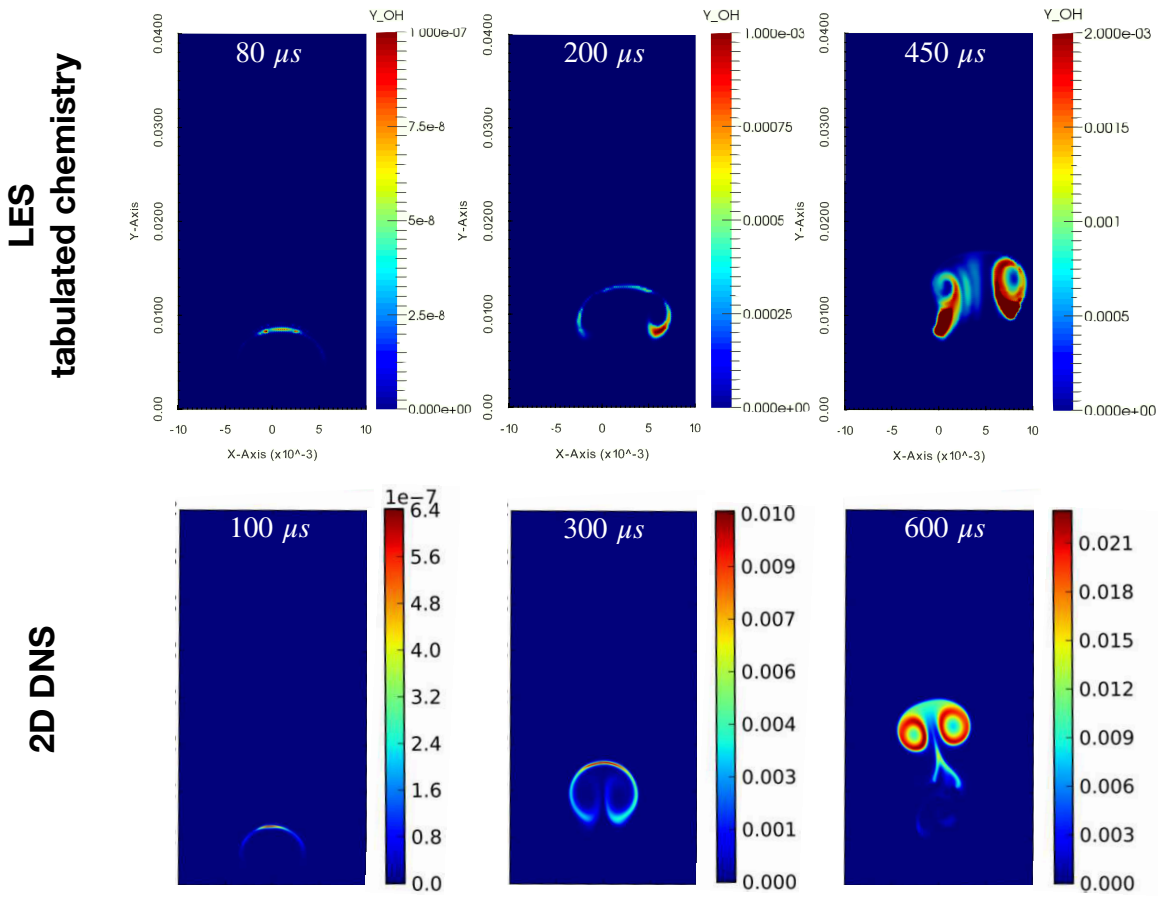

Figure 3.15: OH mass fraction evolution compared between LES forced ignition simulation and DNS simulation. The LES operating condition is of Group 1, with $\phi = 1.1$, $T_{in} = 425$ K. The DNS operating condition is of Group 1, while the exact values of ϕ and T_{in} are not specified in Ref. [8].

of the OH layer appears to be more disturbed for the LES results. This is possibly due to the fuel stratification effects in the LES main flow, where the mixture fraction inlet profile is obtained from the upstream cold flow LES. Conversely, the DNS simulation simplified the main flow to be fully premixed.

For a quantitative validation, the growth history of the flame kernel is compared between numerical simulations and experimental measurements. The operating conditions are similar to Group 2 studies, but at a higher equivalence ratio of $\phi = 1.5$ as this is the only experimental data available. The results are plotted in Fig. 3.16. The

kernel growth is first observed at $1 \sim 2$ ms after kernel injection with an accelerating rate, which corresponds to phase 1 of the forced ignition process where the flame kernel growth is governed by fuel entrainment. After 3 ms, the kernel growth reaches a more stable stage, which corresponds to phase 3 of the forced ignition process where the rate of flame kernel growth is governed by the flame speed. For all fuels considered, the simulation correctly predicts the ignition trends, with C1 showing the weakest growth rate. As pointed out in the last section, this arises from the slow oxidation of initial pyrolysis products.

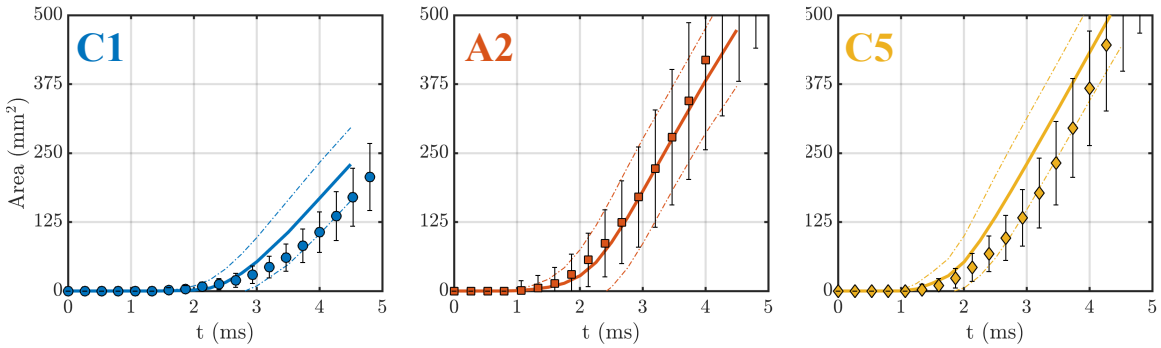

Figure 3.16: Kernel area growth history from 40 samples of successful ignition at $\phi = 1.5$. Experimental results [6] are obtained from chemiluminescence images. Numerical results are transformed from the flame kernel volume (defined by $C \geq 0.275$) by assuming a spherical shape. Dash lines and error bars indicate a 95% confidence interval.

The above comparison against DNS and experimental data, therefore, validated the LES forced ignition simulation and the unified HR/FPVA tabulation model for qualitatively and quantitatively reproducing the fuel entrainment, the transition from an ignition kernel to diffusion-controlled flame, and the propagation of flame front in the forced ignition process.

3.3 Performance of Ignition Probability Estimation

This section validates the developed capabilities of ignition probability estimation. Firstly, the modeling parameters applied in the construction of the response surface of the conditional ignition probability $P_{I|E_d}$, i.e, the first component in the integration of Eq. 2.17, are validated. Secondly, the calibrated distribution of the spark deposit energy, i.e., the second component of the integration, is validated. The resulting final ignition probabilities are as well compared against experimental data for a range of operating conditions.

3.3.1 Validating the Ignition Response Surface

In the two following subsections, it is validated that the estimated response surface of $P_{I|E_d}$ using LES simulation sampling and PCE expansion provides a reasonable and consistent estimation of the true ignition probability conditioned on the spark deposit energy, with uncertainties that can be quantified and controlled.

3.3.1.1 Sensitivity study of partition boundary between HR and FPVA tabulation

Before discussing the response surface of $P_{I|E_d}$, the potential modeling error of the combustion model itself needs to be evaluated. While the combustion model has been validated in Section 3.2.2 for reproducing the forced ignition physics (mainly for the ignition success), the robustness of the LES forced ignition simulation in predicting the ignition outcomes to be success or failure has not been evaluated yet. In particular, while most of the modeling assumptions of the unified HR/FPVA tabulation are intuitive (Sec. 2.1.1) and have been validated (Sec. 3.2.3.4), one modeling parameter that has a potential impact on the ignition outcomes remain questionable, i.e., the partition boundary between the HR and FPVA tabulation. In specific, the upper enthalpy boundary of the FPVA tabulation $H_{FPVA,max}$ is transformed from the partial

extinction temperature T_p (Sec. 2.1.1.2), which is introduced from the counterflow diffusion flamelet theory that is indirectly related to the forced ignition problem here. In this section, a sensitivity study of the LES forced ignition outcomes w.r.t. the $H_{FPVA,max}$ boundary is performed, using the cases of Group 1 studies (methane fuel).

Three levels of the upper enthalpy bound of the FPVA tabulation are tested here, which are obtained from the temperature bounds (denoted as T_{FPVA}). Precisely, T_{FPVA} is tested at {1000 K, 1600 K, 2200 K}, as demonstrated in Fig. 3.17. The highest value of 2200 K is close to the partial extinction temperature of $T_p = 2250$ K, which represents the modeling assumption applied in Section 2.1.1.2. The lowest value of 1000 K is slightly above the $H_{HR,min}$ boundary of $T_a \approx 875$ K, which represents a sharp transition between HR and FVPA. The middle value 1600 K is a compromise between the two extremes, which serves as a nominal case. Simply by looking at the contour of Δt_{Tab}, all three cases show a smooth transition from HR to FPVA tabulation with no prominent differences. To better visualize the difference, the

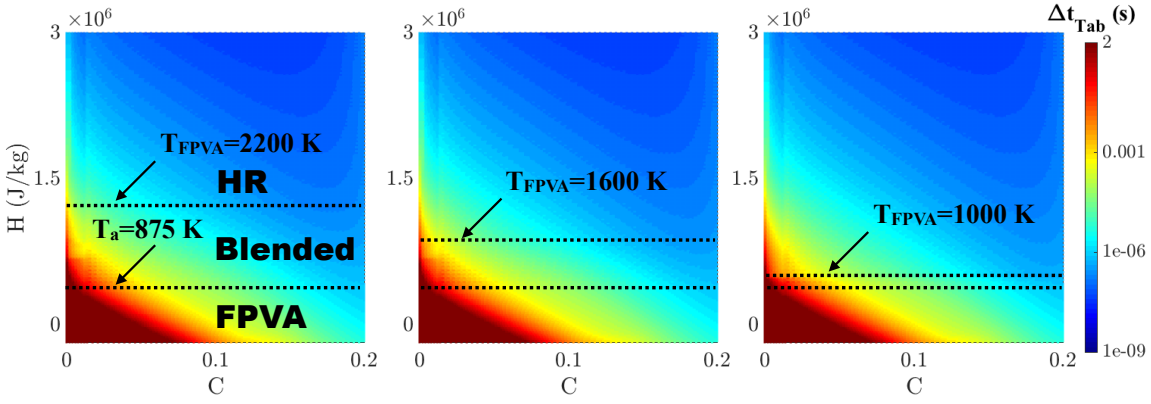

Figure 3.17: Unified FPVA/HR tabulations built using different upper bounds of the FPVA tabulation. The contour is Δt_{Tab} plotted in $h - C$ space, at $Z = Z_{st}$.

percentage of error between different tabulations are shown in Fig. 3.18, which is

calculated as

$$\varepsilon = \frac{\Delta t_{Tab} - t_{Tab}^{T_{FPVA}=1600K}}{\Delta t_{Tab}^{T_{FPVA}=1600K}} \times 100\%. \tag{3.1}$$

In general, when the FPVA-based tabulation region is larger, the tabulated reaction rates are lower. Note that Δt_{Tab} is inversely related to the reaction rate. This suggests that under the operating conditions in the blended tabulation phase space (i.e., an unburnt temperature higher than T_a) the rate-limiting effects of fuel mixing and strain dominate over the rate promoting effects of radical and thermal diffusion.

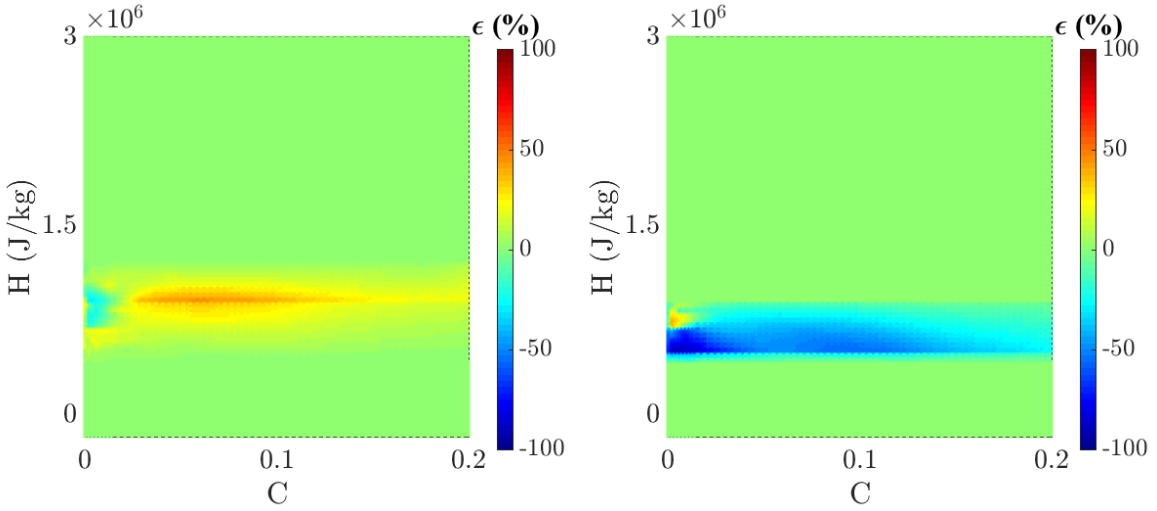

Figure 3.18: Percentage of error of Δt_{Tab} of different tabulations compared to the nominal case of $T_{FPVA} = 1600$ K. Left: $T_{FPVA} = 2200$ K; Right: $T_{FPVA} = 1000$ K.

The potential impact of different enthalpy bounds on the simulated ignition outcome is further studied. A total number of $N_{Spl} = 15$ simulations with randomly assigned initial turbulent flow conditions are performed for each tabulation. All other operating conditions and kernel parameters are set to a fixed level. The results are shown in Fig. 3.19. It can be seen that the actual impact of T_{FPVA} on the simulated ignition outcome is much less significant as the maximum error percentage contour in Fig. 3.19 may suggest: the case of $T_{FPVA} = 1600$ K and 1000 K leads to identical

results; the case of $T_{FPVA} = 2200$ K predicted one ignition success less than the other two cases. Statistically, the potential error caused by this modeling setup is less than the sampling error (Sec. 2.2.4). Physically, this suggests that the ignition outcome here is more dependent on the development of reaction in the early HR stage than the transition stage. It is therefore concluded that within the suggested modeling choice of $T_{FPVA} \sim [T_a, T_p]$, the LES forced ignition simulations using the unified HR/FPVA tabulation predict the ignition outcomes consistently regardless of the specific partition between the two sub-tabulations.

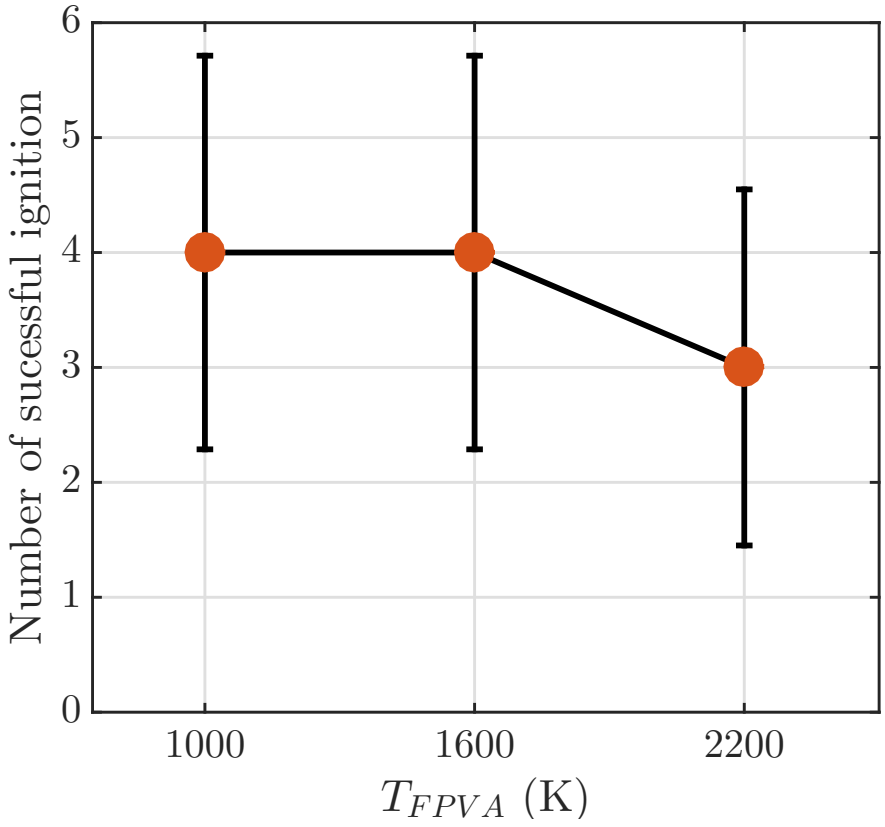

Figure 3.19: Number of successful ignition predicted using different upper enthalpy bounds of the FPVA tabulation. The error bars indicate $1-\sigma$ of sampling error from the total number of simulations $N_{Spl} = 15$.

3.3.1.2 Convergence study of polynomial chaos expansion

In Section 2.2.4, Eq. 2.28, it has been shown that the PCE truncation error is one of the modeling uncertainties that contribute to the estimated conditional ignition probability $P_{I|E_d}$, where a formulation that can be explicitly applied to quantify such error is unavailable. In this section, this error is quantified in the form of a convergence test. The approach is by varying q in Eq. 2.24, as

$$\mathcal{R}_{PCE}(E_d, O; q_i) \approx |\sum_{n=0}^{q_i} \alpha_n H_n(E_d, O) - \sum_{n=0}^{q_t} \alpha_n H_n(E_d, O)|, \tag{3.2}$$

where q_i denotes the PCE truncation order being inquired, and the approximation should approach the true value when $q_t \to \infty$. In this thesis, all the PCE surfaces are constructed with $q_i = 6$, and the PCE convergence is tested with $q_t = 8$. The tests have been performed for each of the response surfaces constructed in the two groups of studies (Sec. 2.2.2.2). Here, only the two PCE response surfaces in the Group 1 studies are shown, i.e., in the phase space of $T_{in} - E_d$ (Case I in Tab. 3.1) and $\phi - E_d$ (Case II), whereas the convergence tests of Group 2 studies are not shown but giving consistent results. The errors between the two PCE expansions are plotted in Fig. 3.20. For comparison, the corresponding turbulence sampling errors estimated by Eq. 2.29 are also plotted. The PCE response surface is plotted as well. Both response surfaces show the consistent trend that the sampling error and PCE truncation error is highest near the region where ignition probability increases from 0 to 1. Further, the PCE response surfaces $P_{I|E_d,PCE}$ well capture the sampled ignition probabilities $P_{I|E_d,Spl}$ (green symbols), and the estimated PCE truncation error is generally smaller and more sparsely distributed than the sampling error. This validates that the applied PCE truncation order of $q = 6$ should be sufficient in this thesis. The PCE truncation error is also neglected in the uncertainty quantification of the final ignition probability, as has been explained in Section 2.2.4.

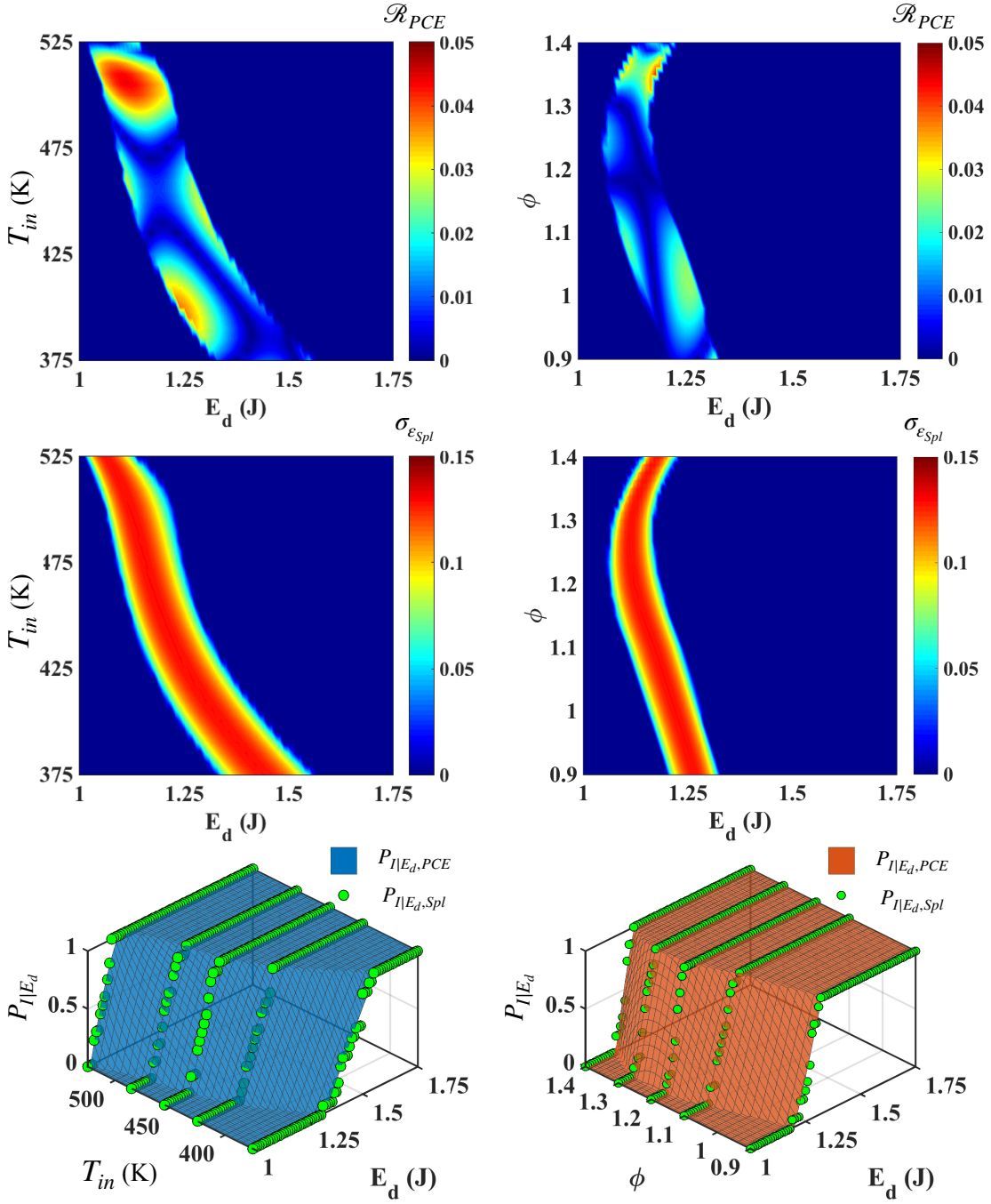

Figure 3.20: PCE truncation error estimated by Eq. 3.2 (top) and sampling error estimated by Eq. 2.29 (middle) and the PCE response surface itself (bottom). The results are shown for Case I in the phase space of $T_{in} - E_d$ (left) and for Case II in the phase space of $\phi - E_d$ (right).

3.3.2 Predicting the Final Ignition Probability

The final ignition probability can now be obtained by the convolution calculation in Eq. 2.17 using the response surface of conditional ignition probability $P_{I|E_d}$ and the statistical distribution of the spark deposit energy $f(E_d)$. The former component has been validated in the above sections, and the latter component is obtained via the distribution calibration procedure developed in Sec. 2.2.3. In this section, the performance of this distribution calibration is first evaluated.

As explained in Section 2.2.3, the calibration procedure is essentially to minimize the L_2-norm of the error between the convolved ignition probability and the experimental data, referred to here as the 'calibration error'. As the experimental measurements also have uncertainties, here, the calibration results obtained using different subsets of the experimental data (i.e., Case I-V in Tabl. 3.1) are compared against each other as cross-validation. Figure 3.21 shows the calibration results by the calibration error for different values of mean energy (μ_{E_d}) and standard deviation (σ_{E_d}) of the spark energy distribution. The result on the l.h.s. is obtained using experiments that contain variations in inflow temperature but at constant global equivalence ratio, i.e., Case I., whereas the result on the r.h.s. is obtained using experiments that contain variation in global equivalence ratio but at a constant inflow temperature, i.e., Case II. Firstly, it is seen that the mean and standard deviation that minimizes the calibration error is approximately the same for both Case I and Case II results in particular for the mean value. This suggests the two experimental datasets have relatively low uncertainties, and the modeling strategy of distribution calibration is consistent with the computational framework of LES forced ignition simulation and ignition probability estimation. Moreover, the mean value that minimizes the calibration error is close to 1.25 J for both Case I and Case II, which is the nominal energy deposited by the igniter. This further validates the developed calibration strategy and the developed coupling method between the kernel and turbulent flow field. Lastly,

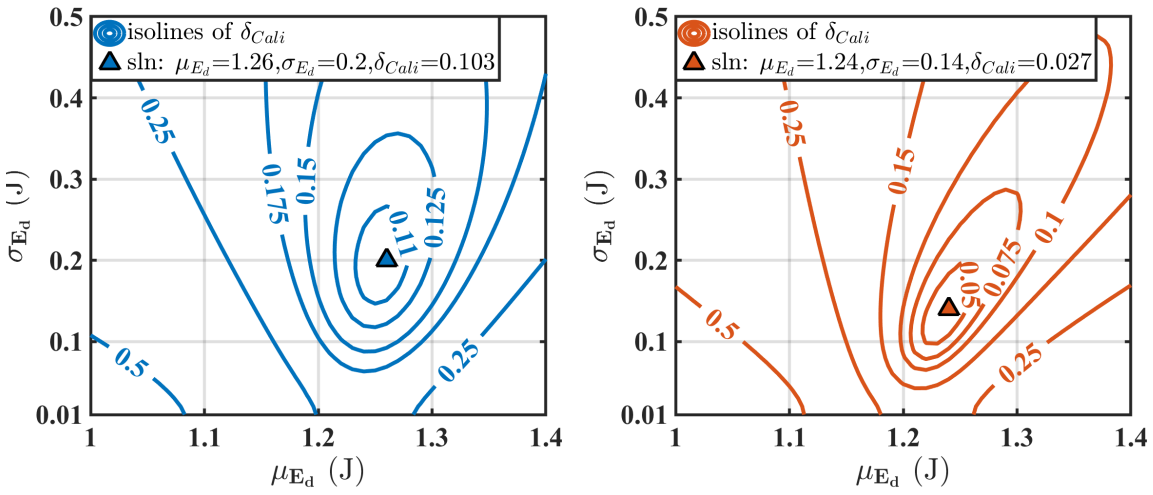

Figure 3.21: Contour of L_2-norm error between convolved ignition probability and experimental measurement calibrated with the Group 1 experimental dataset of Case I (left) and Case II (right). The triangle marks the coordinates of distribution mean and standard deviation that minimizes the calibration error.

it is also seen that as the mean and standard deviation of the distribution deviates away from the optimal solution, the increment of distribution error is more sensitive to the variation in the mean value than that in the standard deviation, which makes sense in terms of the order of the statistical moments.

The resulting ignition probabilities in Group 1 studies is shown in Fig. 3.22 for results obtained with both sets of calibrated distributions. It can be seen that all simulated data predict the variation in the probability of ignition reasonably accurately. In particular, the simulations capture the peak in ignition probability followed by a reduction for both leaner and richer mixtures, and the change in slope noticed between low and high main flow temperatures is also predicted well. For all cases, the computed ignition probability, as well as the uncertainty due to the statistical sampling of the initial turbulence field, cover most of the experimental data.

The same distribution calibration procedure is also performed for Group 2 studies of Case III-V, as shown in Fig. 3.23. Again, the calibrated mean value is consistent

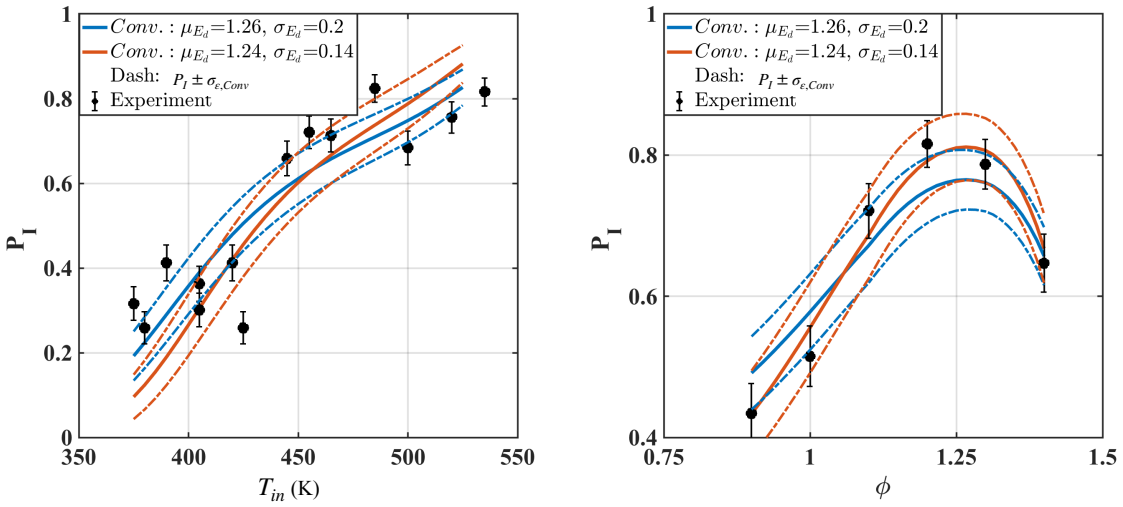

Figure 3.22: Comparison of convolved final ignition probability compared against experimental measurements for Case I (left) and Case II (right) study: blue - results obtained with distribution calibrated against Case I experimental data; red - results obtained with distribution calibrated against Case II experimental data; dash lines and error bars indicate 84.1% confidence interval (i.e., 1-σ).

among three Group 2 cases, while being slightly lower than that in Group 1 cases. Interestingly, the pattern of the iso-lines of the calibration error is also similar for cases within the same study groups but different in between the study groups. Considering the operating condition differences between the two study groups and the uncertainties associated with the experimental measurements, the comparison is acceptable. Besides, the trend of experimental data (symbols in Fig. 3.24) in Group 2 cases are less clear compared to that in Group 1 cases, suggesting larger uncertainties in the Group 2 calibration results. In this consideration, the spark deposit energy distribution calibrated against the Group 1 experimental data should be more reliable and is therefore applied to calculate the final ignition probability of all (Group 2) cases. More precisely, the Case II calibration result is applied (distribution listed in Tab. 3.1.2), which leads to the lowest calibration error among all three Group 1 cases.

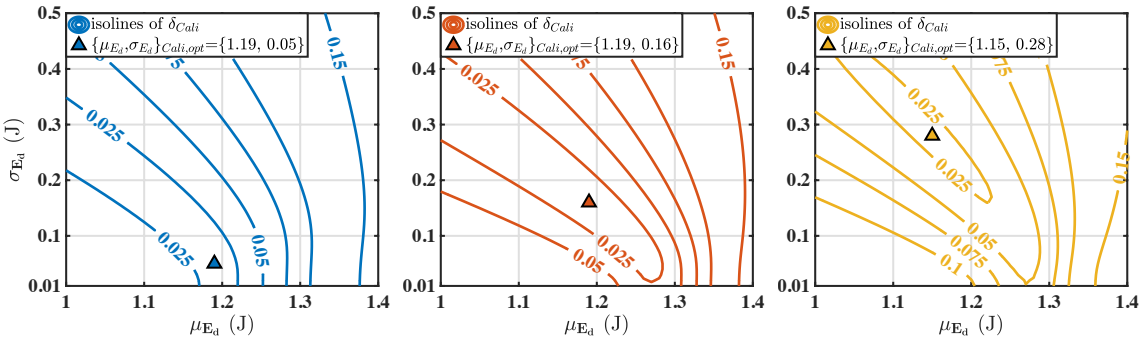

Figure 3.23: Distribution calibration results obtained with Group 2 experimental dataset of Case III (left), IV(middle), and V(right), plotted in the same fashion as Fig. 3.23.

The resulting final ignition probabilities of Group 2 studies are shown in Fig. 3.24. For all three realistic jet fuels, the ignition probability compares well with experimental data. Ignition probabilities over the range of lean equivalence ratios for each fuel generally increased with increased fuel content. Related back to the observed fuel effects discussed in Section. 3.2.3.3, since C5 exhibits significant reactivity during the transition from kernel to propagating flame, it is predicted to have the highest ignition probability among the three fuels considered here. Since C1 is less reactive compared to A2/C5 due to its chemical properties, the kernel quenches more easily due to mixing. The plateau of ignition probability for C1 with increasing equivalence ratio is an illustration of the limit to the balance between the mixture reactivity and the cooling effect of that mixture as it is entrained into the kernel.

As a summary of this section, the developed distribution calibration procedure is validated for providing a statistical distribution of the kernel parameter of E_d that performs consistently among multiple experimental datasets, and the final ignition probability successfully predicts the ignition probability for a range of different operating conditions including, inflow temperature, global equivalence ratio, and realistic fuel effects.

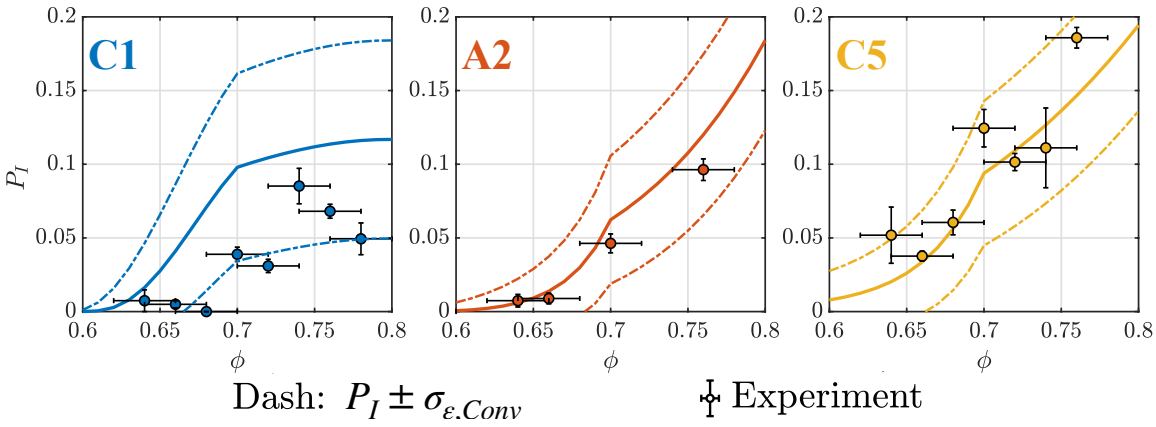

Figure 3.24: Comparison of convolved final ignition probability compared against experimental measurements for Case III (left), Case IV (middle), and Case V (right) study. Dash lines and error bars indicate 84.1% confidence interval.

3.3.3 Evaluating the Computational Cost

As has been explained in Section 2.2.2.1, the number of LES simulations performed during the Monte-Carlo sampling per tested operating conditions has a logarithmic relation to the total number of sampling levels in the E_d-space and a linear relation to the total number of sampling levels in the t_{Spk}-space. The total computational cost is then proportional to the number of LES simulations performed during the Monte-Carlo sampling per tested operating conditions, multiplied by the number of tested operating conditions, as

$$N_{LES} = log_2(N_{E_d}) \times N_{t_{Spk}} \times N_O, \tag{3.3}$$

where N_{LES} is the total number of LES simulation performed in a study, N_{E_d} and $N_{t_{Spk}}$ are respectively the number of sampling levels in E_d-space and t_{Spk}-space, and N_O is the number of tested operating conditions.

In the two groups of validation studies presented in this chapter, the sample E_d-space applied in Group II studies is extended to be larger than that of Group I studies

to ensure a sampled conditional probability of 0/1 at the lowest/highest sampled E_d (see footnote in Tab. 3.1.2), which is related to the intrinsic ignition performance of the tested operating conditions and cannot be controlled before the sampling. To maintain the same sampling accuracy in E_d-space, the number of sampling cases for each tested operating conditions is larger in Group II studies ($N_{E_d} = 150$) than that of Group I studies ($N_{E_d} = 75$). For both study groups, the number of sampled levels in t_{Spk}-space is $N_{S_{Spk}} = 15$, and the number of tested operating conditions in each study group is $N_{Op} = 9$. The total number of LES simulations are therefore $N_{LES} = 900$ and $N_{LES} = 1200$ for Group I and Group II studies, respectively. Later, the initial difference in N_{LES} between the two study groups is compensated by the mesh size difference (see the footnote in Table 3.1.2) as well as other practical supercomputing factors such as the parallel computing scaling efficiency. The final computational cost to perform the LES simulations becomes roughly equal, which is about 1 million CPUh for each of the two study groups. Other computational costs, e.g., cold flow simulations, homogeneous reaction and flamelet calculations, PCE-UQ post-processing, are negligible compared to the Monte-Carlo sampling. Lastly, in a more straightforward illustration, with 4000 processors, it takes about 3 weeks to simulate all the study cases listed in Table. 3.1 and obtain the ignition probability shown in Fig. 3.22 and Fig. 3.24.

The above computational costs remain tractable, mostly due to chemistry tabulation being used in place of full chemistry evolution. Prior studies use at most 25 simulations to construct ignition probabilities [65], which would not have been adequate for the current analysis. The method developed in this thesis is comparatively cheap and allows multiple sources of uncertainties to be included. In general, an ignition probability prediction using the method proposed here should require a computational cost comparable to the validation study presented in this chapter. In particular, the total number of LES simulations of a similar magnitude should be

expected to achieve a modeling uncertainty comparable to conventional experimental measurements, independent of the complexity of chemical reactions, while the exact computational cost should be dependent on the scale of the specific geometry.

3.4 Summary

In this chapter, the developed computational framework is validated using a forced ignition rig that represents turbulent non-premixed forced ignition in altitude relight. The validation is performed extensively covering major aspects of the target problem. The two highlights are as follows: (a) The LES forced ignition simulation using the unified HR/FPVA tabulation model can reproduce the variability of the ignition outcome as well as the forced ignition physics comparable to DNS and experimental data. (b) The ignition probability estimation based on the reacting-flow LES simulations captures the variability with operating conditions at an acceptable computational cost.

CHAPTER IV

Supplemental Studies

In this chapter, two supplemental studies are performed to address unresolved issues related to the thesis topic. The first one is a data-driven study that focuses on understanding the effects of turbulence on the variability of ignition outcome. The second one is a detailed simulation study that evaluates the performance of existing numerical capabilities in predicting the pulsing kernel introduced by the aircraft sunken fire igniter discharge.

4.1 Data-driven Analysis of Turbulent Induced Ignition Variability

In Section 3.2.2.1, the variability of the simulated ignition outcome is demonstrated to be sensitive to turbulence. As the LES forced ignition simulation has now been validated to capture fundamental physics, the focus of this section is to understand how such variability is induced by turbulence by analyzing the simulation data. In specific, the two main questions are addressed here: (a) since turbulence affects the ignition outcome, it is desirable to pinpoint the turbulence structures that induce ignition failure in the target combustor; (b) since turbulent ignition and misfire can themselves occur in different ways, knowing whether or not the combustor has ignited is not sufficient to precisely characterize the response of the combustor to the sparking

process. Therefore, a method that identifies ignition and failure pathways would be useful.

The developed forced ignition LES platform is used to generate a large number of successful and failed ignition events in the target combustor. The two different realistic jet fuels of A2 (Jet-A) and C1 are tested here, which were found to exhibit significantly different ignition behaviors in the validation study presented in Chapter III. Using this data, the cause of ignition failure is evaluated based on a discriminant analysis that delineates the difference between turbulent initial conditions that lead to ignition or failure. From the discriminant analysis, a compressed sensing algorithm is then applied to help pinpoint the locations of relevant turbulent features. Next, a clustering strategy is used to identify ignition success and failure modes. The results presented in this section are mainly based on a recent study of Ref. [122].

4.1.1 Configuration & Numerical Setups

The simulation configuration here is the same one applied in Chapter III for model validation, which has been explained in detail in Section. 3.1.1. The operating conditions along with the numerical setups are almost the same as the Group 2 studies, as introduced in Section 3.1.2 (Table 3.1 and Table 3.1.2). However, the following two adjustments are applied: (a) the global equivalence ratio is raised to $\phi = 1.1$ to increase the ignition probability to about 50%; (b) the spark discharge energy is further adjusted to $E_d = 0.96$ J for the C1 fuel and $E_d = 1.1275$ J for the A2 fuel, where these energy values are obtained iteratively in a preliminary study to bring the ignition probability further closer to 50% for each fuel. The reason to have an ignition probability as close as 50% is to ensure a comparable amount of data samples for both successful and failed ignitions.

4.1.2 Forced Ignition Dataset

The LES simulations are used to characterize individual ignition realizations. Although LES should, in general, reproduce one-time multi-point statistics of the flow [123], the particular forced ignition problem considered here is well-suited for the approximation made. Additional justification is provided in Appendix A.1. Below, the generation of the LES dataset is explained.

The 3-D LES results are recorded for a total number of $T = 21$ times per simulation between 0 and 3.5 ms with points clustered at the early phase of the ignition process, where each 3-D LES flow field is referred to as a "snapshot". To ease the manipulation of data, the unstructured field is interpolated onto a structured grid made of $M = 160 \times 100 \times 40$ grid points with uniform spacing in a domain surrounding the kernel inlet, given by 74.5 mm $\times$ 36.5 mm $\times$ 20 mm in the x, y, and z-directions respectively, which is of a comparable resolution of the original LES grid. For each of the two test fuels, the whole dataset comprises an ensemble of scalar fields $\mathbf{X}_i^t \in \mathbb{R}^M$, where $i = 1, \ldots, N$ is the realization index and $t = 1, \ldots, T$ is the snapshot index within each realization. Here, the ignition success/failure occurs not because of a change in operating conditions, but because of initial turbulent flow condition variability, which is modeled with the same field initialization strategy as explained in Sec. 2.2.2.1.

Unlike in the validation study (Sec. 3.1.2), the ignition outcome here is determined using the maximum field value of the progress variable ($C = Y_{H2O} + Y_{H2} + Y_{CO} + Y_{CO2}$) at the final simulation time $t = T_f = 3.5$ ms. At the final time, if the progress variable value exceeds anywhere in the domain 0.12, the ignition is considered successful. In turn, if the progress variable value does not exceed 0.05 anywhere, the ignition is considered failed. It was found that only in a few simulations lead, at $t = T_f$ to a

maximum value of progress variable between 0.05 and 0.12. Formally,

$$\begin{aligned} \max\left(\mathbf{C}_i^{t=T_f}\right) > 0.12 \implies \forall t, \mathbf{x}_i^t \in \mathcal{S}, \\ \max\left(\mathbf{C}_i^{t=T_f}\right) < 0.05 \implies \forall t, \mathbf{x}_i^t \in \mathcal{F}, \end{aligned} \tag{4.1}$$

where $\mathcal{S}$ and $\mathcal{F}$ are the sets of $\mathbf{x}_i$ containing respectively ignition successes and failures, and $\mathbf{C}_i^{t=T_f}$ is the final progress variable field for the i-th LES simulation. The total number of LES realization is $N = \text{card}(\mathcal{S}) + \text{card}(\mathcal{F})$. For A2, $\mathcal{S}$ and $\mathcal{F}$ have sizes of 237 and 230, respectively; for C1, the corresponding amounts are 212 and 220. From the time history of the maximal field value of progress variable for each LES simulations and each fuel (Fig. 4.1), it can be seen that the criterion clearly demarcates successful ignition and failed ignition. Some of the simulations had a final maximal progress variable value that fell in the range $[0.05, 0.12]$. In that range, it was found that the maximal value of progress variable was neither continuously increasing or decreasing, which prevented labeling the realization as ignition success or failure. It is likely that these simulations correspond to a late ignition or late failure which happens after 3.5 ms. To avoid polluting the dataset with false success or false failure, these simulations were discarded. Nonetheless, the discarded cases constitute only a small portion ($\sim 5\%$) of the total LES realizations.

4.1.3 Data Analysis Strategies

A total of three strategies are applied here to analyze the forced ignition data: (a) an efficient discriminant analysis combined with a compressed sensing approach; (b) a conditional averaging of flow dynamical properties near the flame kernel; (c) a network of ignition success/failure sequence constructed based on K-means clustering. The first two strategies are leveraged to extract the turbulence structures that cause of ignition failure (Sec. 4.1.4), whereas the last one is applied to identify the modes of ignition success and failure (Sec. 4.1.5). The detailed methodologies are explained

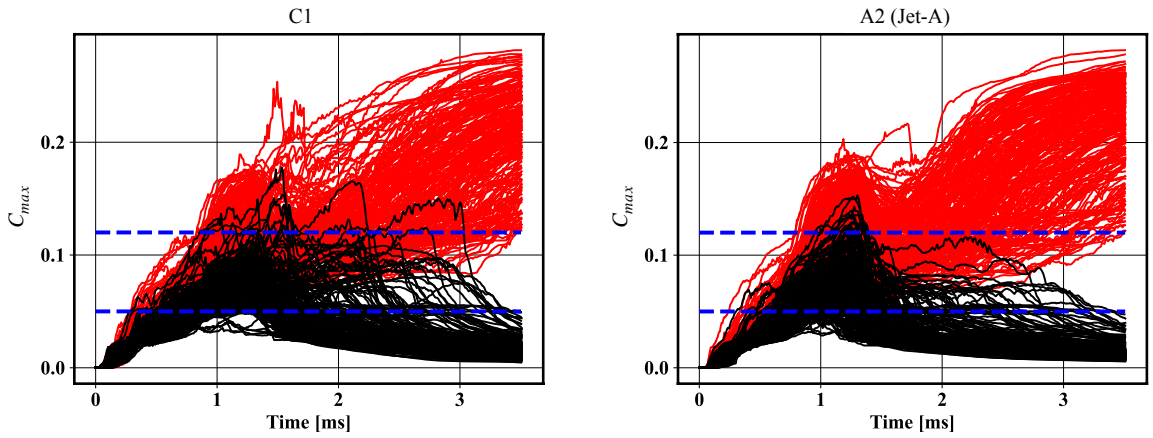

Figure 4.1: Time history of maximal field value of progress variable for all 467 (A2) and 432 (C1) LES forced ignition simulations labeled as successful (red) and failed (black) ignition.

in the following three subsections.

4.1.3.1 Discriminant analysis & sparse sensing

The discriminant analysis and sparse sensing are applied to the initial mixture fraction fields to identify how the initial conditions differ between igniting and failing cases. This goal is reformulated as follows. Each snapshot in $\mathcal{S}$ and $\mathcal{F}$ can be considered as a member of an M degree-of-freedom (DOF) phase space, where M is the number of grid points (or pixels) present in a single snapshot. The goal is to determine a small subset of these M dimensions or grid points that plays an important role in distinguishing whether or not an initial condition will lead to ignition and to potentially connect this subset to turbulence-based causal features. Ultimately, this identified subset of grid points should identify locations in physical space related to high variability in the ignition outcome.

To accomplish this goal, one route is to individually inspect each snapshot and extract key features that delineate ignition success and failure using expert-guided analysis. However, since M (as well as N, the number of realizations) can be very

large, this approach is infeasible. Instead, a more practical route is to employ data-driven techniques that take advantage of the fact that the ignition outcome for each initial condition to be analyzed is already known. As such, the technique employed here (and to be described in further detail below) draws from a method based on supervised classification and sparse sensing [124, 125]. The method relies on a combination of proper orthogonal decomposition (POD, [126]) and linear discriminant analysis (LDA, [127]) to eventually produce the desired subset of grid points, termed *sensors*, of which there are N_S. The term "sparse" here refers to the fact that the method ensures $N_S \ll M$. The workflow of the sparse sensing technique can be categorized into four steps. In step 1, the data in question is organized into classes of interest, here $\mathcal{S}$ and $\mathcal{F}$ (as described in Sec. 4.1.2). In step 2, in the usual case that $M \gg N$, the data is pre-processed using a variant of POD known as the method of snapshots [126]. As a result of the second step, the data is transformed into a so-called POD-space of K dimensions, where $K \leq N$ is the number of retained POD modes. In step 3, LDA is carried out in the POD-space. The *LDA vector* is obtained as a result of this third step, which can be interpreted as a visualizable "flow direction" in physical space (not dissimilar to a POD mode) that discriminates the classes of interest. Then, in step 4, an optimization problem is solved to produce a sparse counterpart to the LDA vector, which provides the desired N_S sensor locations. Inspection of these sensors in physical space then facilitates the analysis of turbulence-driven ignition misfires. This workflow is summarized in Fig. 4.2. Additional detail on the POD (step 2) and LDA procedure (step 3) is provided below, followed by details on the recovery of the sensors from the LDA output (step 4).

The LES data is first transformed from physical space into a K-dimensional POD representation via the method of snapshots [126], as

$$\boldsymbol{X}_i = \sum_{j=1}^{K} a_{i,j} \boldsymbol{\phi}_j. \tag{4.2}$$

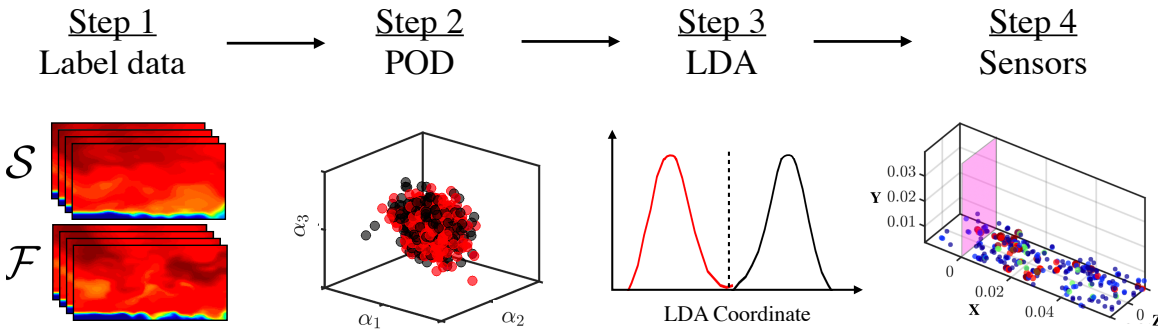

Figure 4.2: Illustration of the sparse sensing workflow. In POD and LDA representations, red is ignition success and black is failure. In the LDA representations (2nd to the rightmost plot), the black line corresponds to the LDA density conditioned on ignition failure and the red line corresponds to that conditioned on ignition success. No clear separation is seen in the first three POD coordinates, but the densities show a clear separation in the 1-D LDA space, which is the desired outcome. The theoretically ideal discriminant outcome measured by Eq. 4.3 should yield from two δ-PDFs located at $\pm\infty$ in the LDA space.

Here, $\boldsymbol{\phi}_j \in \mathbb{R}^{M\times 1}$ is the POD basis vector with j being the mode index, which exhibits the orthogonality feature of $\boldsymbol{\phi}_j^T \boldsymbol{\phi}_j = \delta_{ij}$. The total number of retained POD mode is denoted by K. $\boldsymbol{X}_i \in \mathbb{R}^{M\times 1}$ is the scalar field vector describing the initial turbulent flow (e.g., Z, C, U_x, U_y, ...) with i being the index of snapshot. As only one snapshot in each ignition realization (i.e., the initial flow field) is applied for the discriminant analysis, i here is also the index of the ignition realization (i.e., $i = 1, \ldots, N$). $a_{i,j}$ is the POD coefficient that describes the transformation from the i-th snapshot to the j-th POD mode. The POD transformation allows for a significant speed-up in the following LDA execution, as $K \ll M$. The data-driven analysis here is performed using $K = 400$ POD modes, which retained 99% of the data variance.

LDA is essentially a supervised classification technique, i.e., to label certain quantities to one of several classes using a trained "discriminator". In the two-class problem considered here, the inputs to the LDA algorithm are the sets of pre-labeled data, i.e., $\mathcal{S}$ (successful ignition) and $\mathcal{F}$ (failed ignition), and the output is a single discrimination vector, referred to as the LDA vector $\mathbf{w}$. The LDA vector is an optimal linear

discriminator in the sense that a projection of the data in $\mathcal{S}$ and $\mathcal{F}$ onto $\mathbf{w}$ generates the *LDA coordinates* that best discriminates the classes, where "best" is defined by the two objectives of (a) maximize between-class distance and (b) preserve within-class variance. There also exist more complex discriminant analysis techniques such as non-linear discriminant analysis (NLDA). In NLDA, the data is transformed with a non-linear transformation and the LDA is applied to the transformed data [128]. It can be useful to turn to non-linear techniques if the LDA is unsuccessful. Here, the LDA alone was found sufficient to distinguish igniting and failing initial conditions.

The LDA vector is obtained in the K-dimensional POD space by maximizing the objective function

$$\mathcal{L}(\mathbf{w}) = \frac{\mathbf{w}^T C_B \mathbf{w}}{\mathbf{w}^T C_W \mathbf{w}}, \tag{4.3}$$

where the K-by-K matrices C_B and C_W represent the between-class and within-class covariances, respectively. These are computed using the class-conditional averages, i.e.

$$C_B = (\boldsymbol{\mu}_{\mathcal{S}} - \boldsymbol{\mu}_{\mathcal{F}})(\boldsymbol{\mu}_{\mathcal{S}} - \boldsymbol{\mu}_{\mathcal{F}})^T, \tag{4.4}$$

$$\begin{aligned} C_W = &\langle (\boldsymbol{a} - \boldsymbol{\mu}_{\mathcal{S}})(\boldsymbol{a} - \boldsymbol{\mu}_{\mathcal{S}})^T \mid \boldsymbol{a}_i \in S \rangle \\ &+ \langle (\boldsymbol{a} - \boldsymbol{\mu}_{\mathcal{F}})(\boldsymbol{a} - \boldsymbol{\mu}_{\mathcal{F}})^T \mid \boldsymbol{a}_i \in F \rangle. \end{aligned} \tag{4.5}$$

Here, $\boldsymbol{\mu}_{\mathcal{S}} = \langle \boldsymbol{a} \mid \boldsymbol{a}_i \in \mathcal{S} \rangle$, $\boldsymbol{\mu}_{\mathcal{F}} = \langle \boldsymbol{a} \mid \boldsymbol{a}_i \in \mathcal{F} \rangle$, and $\boldsymbol{a}$ is the POD coefficient vector with i being the snapshot (and realization) index. It can be shown that the LDA vector $\mathbf{w}$ is the eigenvector corresponding to the maximum eigenvalue of $C_W^{-1} C_B$ [124, 127].

An illustration of effective LDA discrimination has been shown in Fig. 4.2. The POD coefficients obtained from the individual classes of data are not necessarily distinguishable in the original POD phase space. The 1-D LDA coordinate here is the projection of a POD coefficient vector $\boldsymbol{a}_i$ onto the LDA vector $\mathbf{w}$, and is, therefore, a

linear combination of the POD coefficients. In the demonstration of Fig. 4.2, an LDA vector can be found such that the resulting PDFs (referred to as the LDA densities) of the projected POD coefficients are clearly distinguished in between the two classes, suggesting the data can be demarcated. However, even if all LDA vectors fail to demarcate the classes (e.g., the LDA densities are heavily overlapping in Fig. 4.6), such an LDA result is still an important piece of information that could be used to understand the causal mechanism.

The sparse sensors are calculated from the LDA vector. First, the representation of the LDA vector in the original M-dimensional space, denoted here as $\mathbf{s} \in \mathbb{R}^M$, is obtained using the POD modes, as

$$\mathbf{s} = \phi \mathbf{w}, \tag{4.6}$$

where $\phi \in \mathbb{R}^{M \times K}$ is the POD basis matrix. Based on the above definition of the POD-LDA analysis, the $\mathbf{s}$ here should represent a single direction (discriminator) in the M-dimensional space that best discriminates the two classes of interest defined in the LDA problem with respect to the scalar field snapshots used to generate the LDA vector. In other words, different snapshots of the initial mixture fraction fields $Z \in \mathbb{R}^M$, after being projected onto this $\mathbf{s}$, will be most clearly separated between the "failure" set and the "success" set. Besides, $\mathbf{s}$ is visualizable for a physical interpretation of the original discriminant problem, as every coordinate (or DOF) of the M-dimensional space is associated with a physical grid point. The magnitude of each component of $\mathbf{s}$ should therefore quantify how a physical grid point contributes to the discriminator $\mathbf{s}$. Then, a sparse vector $\hat{\mathbf{s}} \in \mathbb{R}^M$ is obtained as the solution to the optimization problem of

$$\min_{\hat{\mathbf{s}}} \|\hat{\mathbf{s}}\|_1 \quad \text{s.t.} \quad \phi^T \hat{\mathbf{s}} = \mathbf{w}. \tag{4.7}$$

Upon convergence of the optimization, the sensors are the non-zero elements of this sparse vector $\hat{\mathbf{s}}$, and the total number of sensors is denoted here as N_s. Note that both $\hat{\mathbf{s}}$ and $\mathbf{s}$ are similar in that they (a) exist on the original M-dimensional grid, and (b) produce the same LDA vector $\mathbf{w}$ in the POD space. Thus, assuming good convergence in Eq. 4.7, analysis of the N_S sensors (i.e., the non-zero pixels in $\hat{\mathbf{s}}$) provides a low-dimensional representation of the discriminative features between the two classes used to generate the LDA vector $\mathbf{w}$. To elucidate the meaning of the LDA vector and sensors, the LDA procedure is demonstrated on a toy problem in Appendix A.3 – examples of an LDA vector and sensors obtained from the mixture fraction dataset ($\mathbf{s}$ and $\hat{\mathbf{s}}$, respectively), are also shown.

As will be shown in Sec. 4.1.4.2, there is no guarantee for the LDA vector to be interpretable since it can overfit the input data. Therefore, it is important to assess classification accuracy (referred to here as the LDA accuracy) on the dataset used to generate the LDA vector. Note that the classification accuracy here is not necessarily equivalent to whether the data can be demarcated. For example, the data can be demarcated by two clearly-separated clouds of points after the LDA projection, while the data labels within each cloud (class) can still be completely out of consistency (i.e., the tails of the LDA densities can extend far beyond the classification boundary). The LDA classification here is performed by computing the distance between a snapshot $\boldsymbol{a}_i$ and the respective means $\boldsymbol{\mu}_{\mathcal{S}}$ and $\boldsymbol{\mu}_{\mathcal{F}}$ after being projected onto the LDA vector $\mathbf{w}$ (i.e., the distance between the corresponding LDA coordinates). A snapshot closer to the conditional mean of one class in the LDA space is assigned to that class. Therefore, the classification boundary in the LDA space is simply at the mid-point of the two conditional means, which is demonstrated as the dashed line on the rightmost plot in Fig. 4.2. The resulting LDA accuracy of a certain class is measured as the percentage of data with the correct labels. The LDA accuracy quantifies the ability of the LDA analysis to recognize initial conditions that

leads to ignition success and failure. To ensure no overfitting, the sparse version of the LDA accuracy can be obtained. This step is achieved by generating a dataset using an element-wise multiplication of each snapshot $\boldsymbol{X}_i$ with the sensor locations in the sparse vector $\hat{\mathbf{s}}$. Namely, only the data corresponding to the location of the sensors is kept, with everywhere else is discarded. The LDA classification accuracy in terms of this sparse dataset then provides a measure of the overall viability and utility of the recovered sensors. If the sparse classification accuracy is reasonably high, it can be concluded that the discrimination power of the LDA is not a result of overfitting, and thus the sensors can be physically interpreted. Otherwise, the corresponding sensors should not be considered as meaningful.

As a final measure to address overfitting, a cross-validation training strategy is further applied when computing the sparse sensors. More specifically, a statistical representation of the sensor locations is obtained by running multiple realizations of the LDA sensor training (i.e., Eq. 4.7) using randomly chosen subsets of snapshots from the full dataset. Besides, before each training realization, a single subset is obtained by removing 15 snapshots at random from both $\mathcal{S}$ and $\mathcal{F}$. The 30 removed snapshots then become the testing set for that training realization where the LDA accuracy is evaluated. The above ensemble of optimization runs allows for a more robust analysis of sensor behavior - in particular, the frequency at which a single grid point is chosen as a sensor can be used to assess sensor importance. Here, 50 realizations of the optimization (i.e. 50 different LDA and sensor outputs) are performed to assess the sparse sensing results for each fuel.

4.1.3.2 Conditional averaging of near-flame-kernel flow dynamics

The discriminant analysis combined with the sparse sensing isolates turbulent features that differ between initial conditions that lead to ignition success or failure. Because that analysis was performed at initial times, it allowed concluding the cause

of ignition or failure. Following the discriminant analysis, the evolution of the flame kernel at later times is tracked, to confirm those findings from the aspect of the forced ignition physics. In this case, conditional averages among the igniting and failing flame kernels are useful. Note that the surface averaging here is calculated over the flame kernel instead of the kernel. As has been clarified earlier, in this thesis, the term "flame kernel" (fluid pocket of high concentration of reaction product) is different from the term "kernel" (fluid pocket high energy), where only the first concept is closely related to the forced ignition outcomes and, therefore, chosen as the ignition process tracker that better suits the study purpose here.

Since the focus is on the interaction between turbulence and the flame kernel, only quantities at the flame kernel boundary are extracted. The flame kernel boundary is defined here as the iso-surface of $C = 0.02$, which was found to be indicative of the early stages of flame kernel development. However, note that the results presented later in this study are also broadly insensitive to the choice of the iso-surface value. The surface is extracted using a standard marching cube method [129]. Different turbulence properties (i.e., vorticity and strain rate) are then extracted and interpolated at the flame kernel iso-surface.

At every time instance (the same snapshots index within each ignition realization), the iso-surface area can vary from realization to realization. To avoid biasing the results towards early ignition cases which have a larger kernel surface area, the plotted statistics of the quantity ξ are calculated simply as the arithmetic means of the surface-averaged quantity over different realizations:

$$\begin{aligned} \widehat{\xi_{\mathcal{S}}}(t) &= E_{\mathcal{S}}(E_{fks_i|\mathcal{S}}(\xi_i(t))), \\ \widehat{\xi_{\mathcal{F}}}(t) &= E_{\mathcal{F}}(E_{fks_i|\mathcal{F}}(\xi_i(t))), \end{aligned} \tag{4.8}$$

where $\widehat{\xi_{\mathcal{S}}}(t)$ (respectively $\widehat{\xi_{\mathcal{F}}}(t)$) denotes the near-flame-kernel statistics for successful (respectively failing) ignition, and $E(.)$ and $E_{fks_i}(.)$ are the expectation operators that

calculate, respectively, the arithmetic average among different realizations and the surface average over the flame kernel surface boundary. Note that $\widehat{\xi_{\mathcal{S}}}(t)$ (respectively $\widehat{\xi_{\mathcal{F}}}(t)$) is a time-varying statistic of the quantity ξ for all successful (respectively failing) cases, with subscript i being the index of ignition realization. To clarify, in contrary to the LDA analysis, where i is both the snapshot index and the realization index, here, multiple snapshots are used for each realization, and i is used only as the realization index. The variances used to quantify uncertainties for $\widehat{\xi_{\mathcal{S}}}(t)$ and $\widehat{\xi_{\mathcal{F}}}(t)$ are also computed in a similar manner.

4.1.3.3 K-means clustering & networks of ignition sequence

Existing data classification techniques are leveraged to identify ignition and failure modes from the simulations. At every time instance recorded, the snapshots from different ignition realizations are classified into clusters, such that each cluster represents an ignition mode. This process is done in an unsupervised manner using K-means clustering [130, 131], which has been successfully used in a variety of fluid applications [132–135]. The K-means algorithm takes as an input a number of clusters and subsequently groups the realizations (or snapshots) into these many clusters. The groups are created such that the variances of the snapshots within a cluster are minimized. More formally, starting from N data points $\mathcal{X} = \{x_1, ..., x_N\}$, one would like to define N_k clusters $\mathcal{C} = \{C_1, ..., C_{N_k}\}$. Each cluster C_k is an ensemble of data points and can be characterized by its barycenter, or centroid $c_k = \sum_{x \in C_k} x$. The K-means algorithm solves the following minimization problem

$$\arg\min_{\mathcal{C}} \sum_{C_k} \sum_{x \in C_k} d(x, c_k)^2. \tag{4.9}$$

The centroid can then be considered as a representative of its cluster and can be used for interpretation.

The K-means clustering relies on two "hyperparameters" that need to be decided by the user: the number of clusters and the type of distance chosen. For the first hyperparameter, there exist indicators that evaluate how suited a candidate number of clusters is to a particular dataset. However, these indicators should not be considered as a systematic way of choosing the number of clusters [133], but rather as guidelines that should be refined by the user. Here, two different indicators (silhouette score [136] and X-means [137–139]) were used to determine the optimal cluster number. Although both methods gave a different cluster number, the results presented in Sec. 4.1.5 were not sensitive to this choice. In the results shown, the number of clusters is chosen using the silhouette method, since the number of clusters was lower overall than the X-means counterpart, facilitating interpretation (see Appendix A.2). The silhouette and K-means algorithms are imported from the Scikit-learn library [140], and X-means is imported from the `pyclustering` library [139]. For the second hyperparameter, here, the distance chosen for the clustering is the L_2 norm computed in physical space. While this choice has been sufficient in other applications [132–134], it is not necessarily ideal. Other distance measures based on image recognition concepts were investigated [141], though these led to the same conclusions as the ones to be presented in Sec. 4.1.5.

During each ignition or misfire realization, the 3D data is printed at 21 time instances. Then, for each fuel, for each type of event (ignition or misfire), and for each one of the 21 time instances, an optimal number of clusters is computed using the silhouette method. Note that the number of clusters need not be constant across time instances (see Appendix A.2). For each fuel, for each type of event, and for each one of the 21 time instances, the data is clustered. The result of the clustering is visualized by using the centroid as a representation of each cluster. Since the data clustered is three-dimensional, the centroid is also three-dimensional. Between each time instance, a snapshot jumps from one cluster to another. By recording how often

a realization transitioned between clusters, one can build a probability map of the ignition sequence. For example, if 90% of the realizations that belong to cluster A after 1 ms, belong to cluster B after 2 ms, one can infer that the path from cluster A to B is dominant. This idea is similar to the one developed in Ref. [134], except that the goal is not to build a reduced-order model of an ergodic system, but to summarize the evolution of many realizations. The full ignition sequence can be visualized as a forward-in-time network, where vertices are the centroids and edges are the transition probability. The network allows quick visualization of different ignition and failure pathways. For clarity, the networks are not reproduced inside the manuscript of this thesis.

Different ignition modes can then be interpreted based on the network of ignition sequence constructed. It should be emphasized that the number of clusters should be distinguished from the number of ignition modes: a mode refers to a unique physical mechanism that distinguishes it from other modes. In practice, the same mode can appear in several clusters in a more or less pronounced form. Identifying modes from clusters depends on the type of conclusions needed, and requires expert knowledge. The results shown in Sec. 4.1.5 are the result of this analysis, where the interpretations are carried out mainly as the following procedure. For each cluster at the last recorded time (21^{st}), the highest possible pathway that leads to this cluster is found from all permutations of pathways and is assigned to an ignition mode. In other terms, here, the total number of interpreted ignition modes N_m equals to that of the clusters at the last recorded time, which is found to be 2 for all the cases using the silhouette method. At other recorded times, all the clusters that those highest probability pathways go through are also assigned to the corresponding ignition modes.

4.1.4 Cause of Ignition Failure

Using the above data analysis strategies, the first objective is to extract the turbulence structures which most disturb the ignition outcome, i.e. causing the ignition to fail. The causality is first inferred using the POD-LDA analysis combined with the sparse sensing, and is then confirmed by the flow dynamics statistics collected near the flame-kernel. The physical interpretations of the results are presented in the two subsections below.

4.1.4.1 Influential initial conditions

The LDA densities and sensor outputs corresponding to the mixture fraction for A2 fuel at $t = 0$ (the initial condition) are shown in Fig. 4.3. In the top row of Fig. 4.3, three LDA densities are shown for three different representations of the input mixture fraction fields. Each LDA density plot contains the results from 50 realizations of the LDA sensor training in Eq. 4.3. The leftmost LDA density plot corresponds to the projection of the full mixture fraction dataset onto the LDA vector $\mathbf{w}$. The middle LDA density plot corresponds to the projection of the sparse mixture fraction dataset (obtained from the sensor locations as described in Sec. 4.1.3.1) onto the same LDA vector. The rightmost density plot corresponds to another sparse dataset for a smaller, cropped domain that is more localized around the igniter tip (see the box in the bottom-right plot in Fig. 4.3) - its purpose is described further below.

The sensors obtained from the A2 mixture fraction fields achieve overall good discriminative power. The separation in the LDA densities of different classes, though not perfectly ideal, is also quite pronounced even in the sparse datasets. This is a powerful result in itself, as the average number of sensors over the 50 optimizations for the full and cropped domains is $N_S = 299.6$ and 332.4, respectively. Such numbers are three orders of magnitude smaller than the original field dimensionality ($M =$

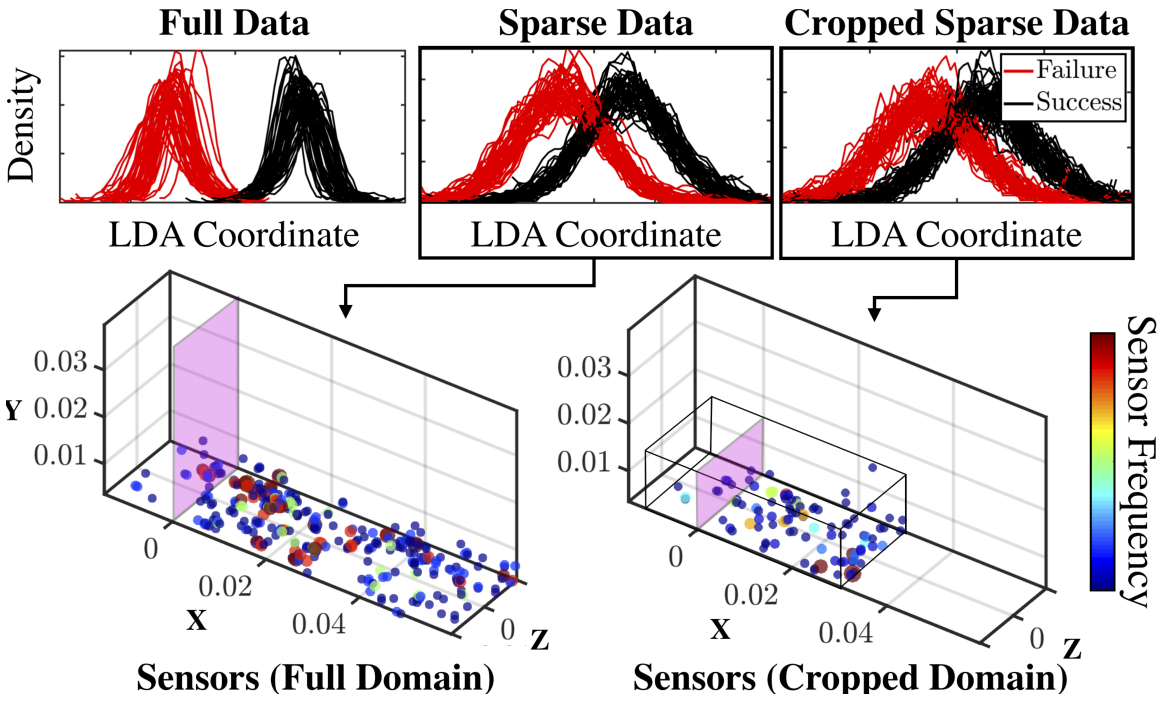

Figure 4.3: Top - density of mixture fraction at $t = 0$ for A2 in the LDA space generated by 50 different runs. Left corresponds to original data, middle to sparse data, and right to sparse data computed from runs with a cropped domain. Bottom - corresponding sensor locations with colors indicating the sensor frequency (higher frequency means more probable in the cross-validation sensor training). The highlighted plane indicates $x = 0$ and the box enclosing indicates cropped domain bounds.

$160 \times 100 \times 40$). In other words, only a few mixture fraction locations at the initial condition are needed to discriminate between ignition success and failure to reasonable accuracy in the A2 case. Besides, the corresponding sparse LDA-accuracy (Fig. 4.6) is also good for the A2 fuel, suggesting its ignition outcome is mostly affected by the turbulent fuel mixing.

The full domain sensor locations (bottom-left plot of Fig. 4.3) show that most high-frequency sensors are predominantly (a) contained in the mixing layer, and (b) located to the downstream (positive x-direction) of the igniter tip (centered at $x = 0$). Besides, some of the sensors in the full-domain case are located far downstream of the igniter and are therefore non-physical. This behavior is a limitation of the sparse

sensing method and requires physical insight to rule out some of the sensors. In this consideration, the analysis re-performed but on the cropped domain (bottom-right of Fig. 4.3) intended to explicitly enforce the sensor locations to coincide with physical, prior expectations, i.e., domain region closer to the igniter tip. This can be considered as a user-guided weighting of the near-igniter region, so as to eliminate potential downstream noise effects on the sparse sensing output. Figure 4.3 shows that the high-probability sensors in the cropped-domain case are still predominantly downstream of the igniter, indicating that this region is indeed influential with regards to A2 ignition outcome.

The experimental studies have already evidenced the influence of the time taken by the kernel to reach the mixing layer (transit time $\tau_{transit}$) on ignition [5]. Therefore, it is unsurprising to find sensors located at the mixing layer. What was not well-established is that the fuel-kernel mixing above the mixing layer is of little importance. This suggests that the non-local effects are solely contained in the mixing layer, i.e., the fuel entrainment into the PJICF kernel (discussed in Sec. 3.2.1) when it first reaches the mixing layer are the most influential on the ignition outcome. Similar observations were made for different geometries in Refs. [2, 46, 65, 142]. The importance of this downstream part of the mixing layer on ignition is more surprising, as one would instead expect turbulent structures advected from upstream to be more influential. A further interpretation is provided below.

The sparse representation of the LDA analysis can only achieve a good LDA accuracy when a small collection of points in the original domain can be used to recover a high class-discrimination. For the turbulent forced ignition problem, this is possible when the ignition outcome is affected by the localized turbulent structures of large scales. More discussions of this interpretation are presented in the following section. While the sensors do not provide a physical interpretation by themselves, they indicate where the flow should be examined - the mixture fraction field should

be inspected along the streamwise and spanwise directions near the mixing layer. To this end, the mixing layer height is extracted as the height of the iso-surface of $Z = 0.03$. The height is averaged over the igniting and failing initial conditions for the A2 fuel, and over the streamwise direction, and is shown in Fig. 4.4. It can

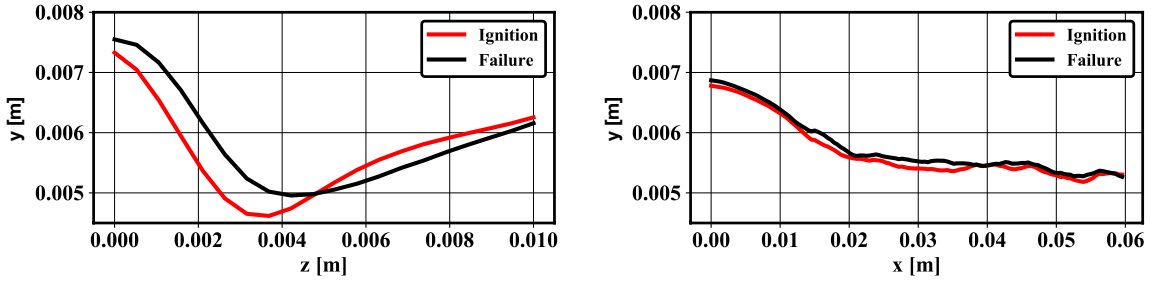

Figure 4.4: Left - spanwise profile of mixing layer height averaged over ignition realizations and the streamwise direction plotted for half of the domain. Right - streamwise profile of mixing layer height averaged over ignition realizations and the spanwise direction. Igniter tip is at $\{x = 0, y = 0\}$.

be seen that the mixing layer is the highest near the centerline which is where the igniter tip is located. Since the mixing layer height decreases with the streamwise direction, it could explain why the downstream region is instrumental for A2 ignition. The main difference between the cases of ignition success and ignition failure can be seen along the spanwise direction where the mixing layer experiences a steep drop, especially in the igniting cases. This phenomenon may be the result of a stronger recirculation caused by the igniter tip (the igniter tip intrudes into the domain for the Group 2 operating conditions, as explained in Sec. 3.1.2), which will in turn aid the entrainment of fuel into the kernel.

To validate this interpretation, near-flame-kernel turbulent statistics are used. The instantaneous vorticity magnitude ω averaged over the realizations of ignition success and ignition failure is computed using Eq. 4.8. Figure 4.5 shows the resulting $\widehat{\omega_{\mathcal{S}}}(t)$ and $\widehat{\omega_{\mathcal{F}}}(t)$ for both fuels. At 0.4 ms (when the kernel bottom first enters the main flow, see Fig. 3.12), higher values of vorticity appear to promote ignition. At

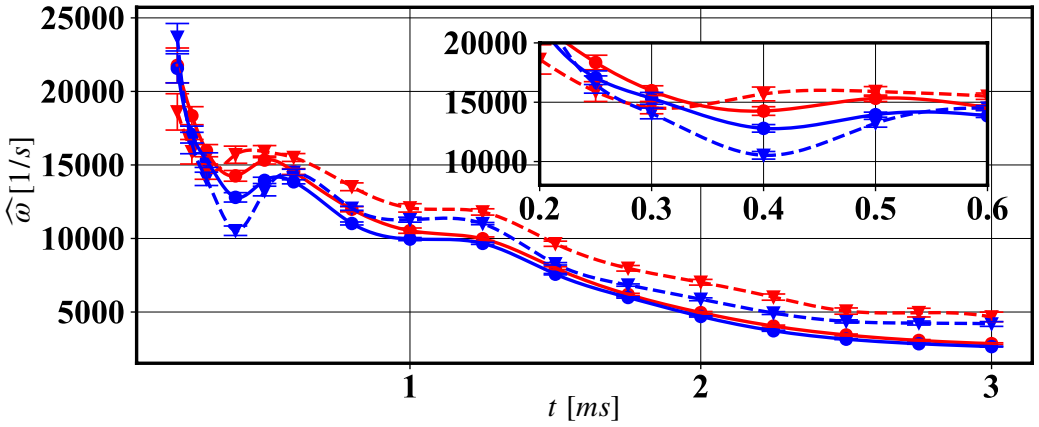

Figure 4.5: Time evolution of the mean vorticity magnitude at the iso-surface $C = 0.02$ for A2 (blue) and C1 (red) and averaged over the ignition success cases (solid) and the ignition failure cases (dash). The line plots are interpolated from values at recorded time instances (symbols, with error bars that represent statistical uncertainties) to ease visualization. The subplot represents zooms in the region of interest.

that time, the main vortical structure is the vortex ring generated by the PJICF kernel (Sec. 3.2.1), which entrains fuel. It can be concluded that fuel entrainment is an important driver for the ignition of A2. This contrasts with C1, where higher high values of vorticity do not promote ignition. At later times, large values of vorticity are detrimental to ignition for both fuels.

4.1.4.2 Cause of ignition failure for different fuels

The sensor procedure for the initial mixture fraction field was also carried out for the C1 fuel. The LDA density from the full-domain case, again for 50 realizations of the algorithm, as well as associated LDA accuracies for success and failure (along with the accuracy for the full domain case for A2 shown in Fig. 4.3) are shown in Fig. 4.6. As opposed to A2, the sparse LDA is significantly less accurate (right plot in Fig. 4.6). The minimum of C1 sparse LDA accuracy for both success and failure reaches the 50% mark, which is very close to the designed ignition probability of the dataset. Thus, the C1 sensors for initial mixture fraction do not provide any real

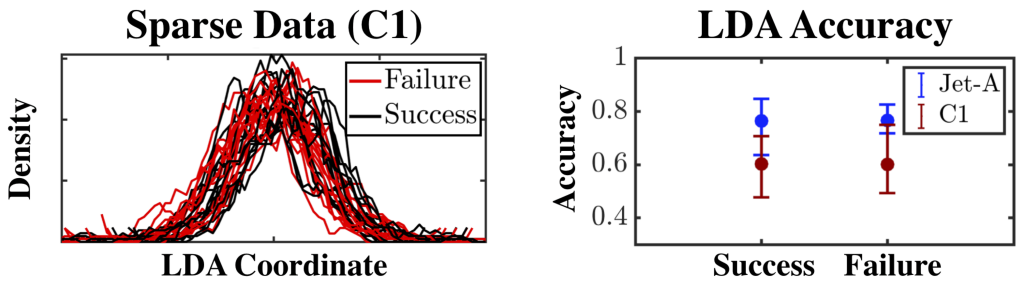

Figure 4.6: Left - LDA densities of sparse dataset using initial mixture fraction fields for C1 fuel (all 50 realizations of algorithm shown. Right: mean LDA accuracies of the full-domain sparse dataset for A2 (blue, corresponding LDA densities are plotted in Fig. 4.3) and C1 (red) for mixture fraction fields at $t = 0$. Error bars indicate maximum and minimum values from the various runs.

level of discrimination power. This reveals a key difference in the flow structures that drive ignition between the two fuels, which is interpreted below.

The sparse classification is based on a representation of the LDA vector in the grid coordinate space (i.e., $\boldsymbol{s} \in \mathbb{R}^M$) with a sparse vector. Since representing small scales requires more grid points than large scales, it can be expected that the sparse vector will perform better when representing processes that are dominated by the larger structures in the flow. If the scales that drive the ignition outcome are too small to be efficiently resolved by the sparse vector, then the classification is expected to be ineffective. This motivates the hypothesis that C1 ignition is more influenced by small scales, while A2 is influenced by larger structures.

To verify this hypothesis, near-kernel strain-rate statistics are examined. This time, the magnitude of the strain rate tensor S is averaged over the flame kernel surface and plotted for all of the igniting and failing cases for both fuels in Fig. 4.7. Similar to the mean vorticity magnitude history (Fig. 4.5), here, most of the differences between fuels can be observed at 0.4 ms, which corresponds to the early phase of ignition (see Fig. 3.11 and Fig. 3.12). At this time, for C1 fuel, the strain rate is about 30% higher for failing cases than for igniting cases. A similar discrepancy in strain rate for igniting and failing cases for A2 is not observed. Vorticity is indicative

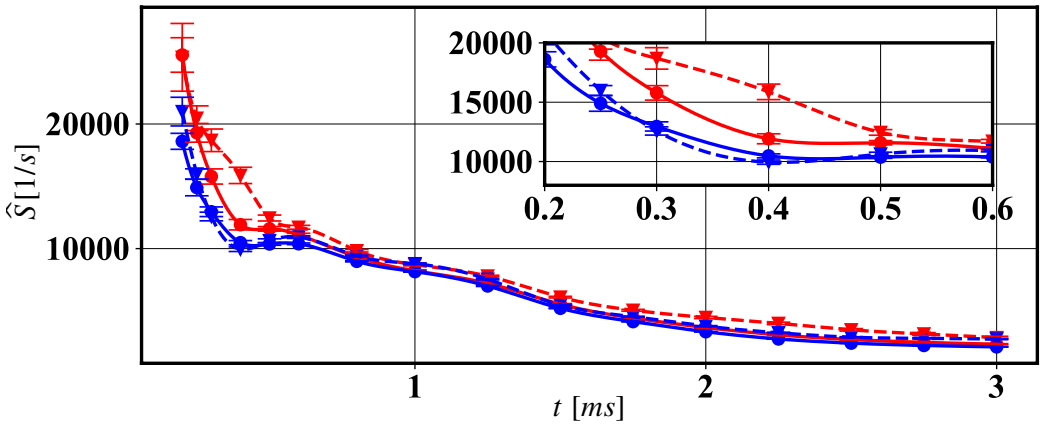

Figure 4.7: Time evolution of the mean strain magnitude at the iso-surface $C = 0.02$ for A2 (blue) and C1 (red) and averaged over the ignition success cases (solid) and the ignition failure cases (dash). Plotted in the same fashion as Fig. 4.5

of an organized turbulence structure while strain rate can be associated with any type of velocity gradient. This supports the fact that an organized structure such as recirculation may be more influential in the case of A2 as compared to C1.

4.1.5 Modes of Ignition Success and Failure

In the previous section, the types of turbulent structures that affect the ignition outcome were identified in the case of A2 and C1 fuels. However, the realization-to-realization variability is not only limited to changes in ignition outcome, but to variation in the process by which the ignition outcome occurs. In other terms, the combustor can experience different ignition and failure modes which can lead to different types of behavior for the combustor. Therefore, knowing what ignition and failure modes are possible in a given combustor is essential for design purposes. In this section, it is shown how the data generated can be used to identify the different ignition and failure modes through the clustering technique. The results are presented and discussed in the three subsections below.

4.1.5.1 Ignition Success Modes

First, all the progress variable snapshots that correspond to ignition realizations are clustered. While only the mid-spanwise plane of the centroids are shown here, the clustering is done with the 3-D data. Only three recorded time instances from each mode are shown here that corresponds to different phases of the forced ignition process. The probabilities mentioned here are based on the size of the cluster at the last time instance.

Two main ignition paths are found for C1 and are shown in Fig. 4.8 as a sequence of centroids at select time instances. Mode 1 is the most common ignition mode and is found to occur about 95% of the time (202 realizations out of 212). The ignition mode can be described as follows: ignition starts in the counter-rotating vortex pair (i.e., the mid-spanwise plane CVP, as introduced in Sec. 3.2.1) of the emerging kernel; then, the windward side (upstream) of the vortex ignites while a continuous roll-up of on the leeward vortex mixes the surrounding fuel with the hot kernel; eventually, ignition develops in the leeward vortex. This mode is similar to the previous descriptions from LES simulations with detailed chemistry [102]. Further, by comparing the 3-D flame surface to the forced ignition physics found in Section. 3.2.3.2 and Section. 3.2.3.3, it can be seen that this mode well-corresponds to the typical 3-phase ignition schematic summarized in Fig. 3.11: the ignition first takes place due to fuel entrainment on the windward side; then, the initial flame surface on the windward side is quenched, and the propagating flame front is established within the cross-section plane CVP (out of the plane of Fig. 4.8); at a later time, the flame propagation eventually reaches the leeward side of the kernel. Note that the ignition progresses here faster than that in the Group 2 validation studies in Sec. 3.2.3.3 due to the higher global equivalence ratio. Conversely, Mode 2 is found to occur only 5% of the time (10 realizations out of 212) and exhibits unique features. As the kernel emerges, the mid-spanwise plane CVP is heavily tilted with the windward vortex being located at a lower y-location

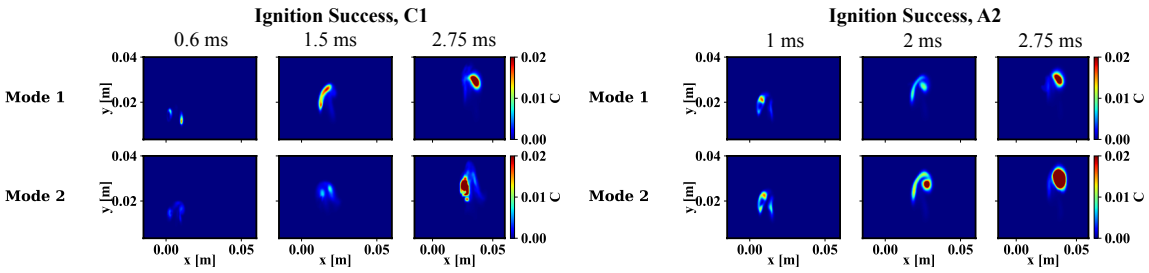

Figure 4.8: Mid-spanwise planes of progress variable centroids that correspond to Mode 1 (top) and Mode 2 (bottom) for ignition success of C1 (left) A2 (right), at different time of the ignition process.

than the leeward vortex. This behavior leads to a breakdown of the kernel which ignites only on the windward side, which will be further discussed in the later section.

As shown in Fig. 4.8, A2 also exhibits two main ignition paths, but the differences between these two modes are not as pronounced as for C1. Both modes of ignition of A2 resemble Mode 1 of C1, as well the 3-phase ignition schematic in Fig. 3.11. The only difference between the two A2 modes is that the progress variable in Mode 2 is higher than that in Mode 1 at each of the reaction phases, which leads to an overall stronger ignition. Out of the fuels studied, C1 is the only one that exhibited kernel breakdown which suggests that it is the most affected by small and disorganized turbulence structures. This observation is consistent with the analysis of Sec. 4.1.4, where it was found that C1 was influenced by smaller turbulence structures than A2.

4.1.5.2 Ignition Failure Modes

By clustering the progress variable field for all the failed ignitions, two main ignition paths are also identified for A2 and C1. For C1, the ignition failure modes shown in Fig. 4.9 are similar to the ignition success modes in Fig. 4.8. In the case of Mode 1, the progress variable grows first in the windward vortex and then the leeward vortex. However, the progress variable growth is too slow to counteract thermal

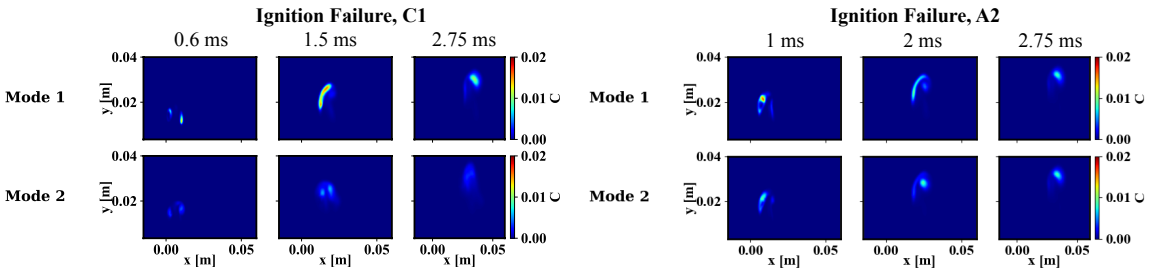

Figure 4.9: Mid-spanwise planes of progress variable centroids that correspond to Mode 1 (top) and Mode 2 (bottom) for ignition failure of C1 (left) A2 (right), at different time of the ignition process.

energy dissipation. In Mode 2, the kernel experience the same tilting as described in Sec. 4.1.5.1 which later leads to a vortex breakdown. A notable difference is that Mode 2 is observed for 27% of the realizations (59 realizations out of 220), while it was observed for 5% of the successful ignition realizations. When a kernel breakdown occurs (69 realizations in total), it can be favorable to successful ignition (15% of the time) but much more often leads to failed ignition (85% of the time).

In the case of A2, although the paths appear separate, the kernels are in a similar state, which is again similar to the successful ignition modes. Slight differences in the value of the progress variable can be identified between the two modes. Overall, the values of the progress variable are lower all the way through the failed ignition sequence compared to the successful ignition sequence. It can be concluded that the early phase of the ignition process is instrumental for the ignition outcome. This observation is in line with other work [2, 46, 65, 142].

4.1.5.3 Causes and effects of kernel breakdown

From the analysis of the previous subsections, it appears that C1 differs from A2 because the kernel can experience a breakdown at the later phases of the ignition process. Here, the causes and the consequence of the breakdown are further detailed.

First, the breakdown mechanism is investigated by clustering the temperature field

following the same procedure as used for the progress variable. Figure 4.10 shows the mid-spanwise plane of the temperature centroid corresponding to Mode 1 and 2 for the ignition and failure of C1 at 0.6 ms. At this phase, the kernel has just entered the main flow and started tilting and the advancement of the combustion is visibly different. In Mode 1 (typical ignition schematic), the entire vortex ring is hotter than in Mode 2 (kernel breakdown) which could act as a viscous buffer that would prevent the kernel from being exposed to turbulent fluctuations.

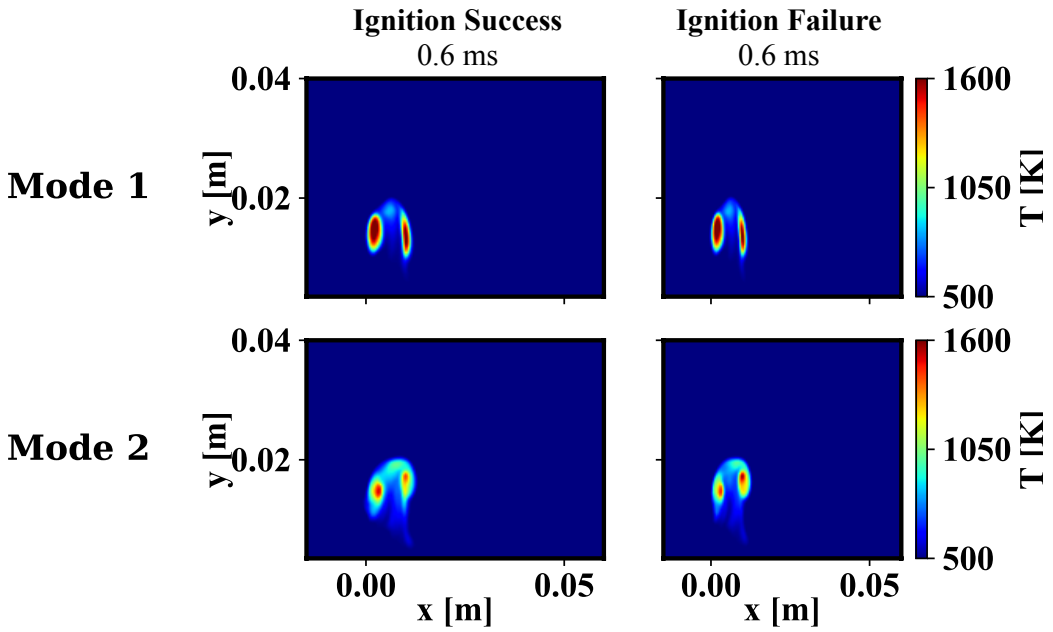

Figure 4.10: Mid-spanwise planes of temperature centroids that correspond to Mode 1 (top) and Mode 2 (bottom) for ignition (left) and failure (right) of C1, at $t = 0.0006$s.

While the probability map cannot determine the root cause of the kernel breakdown, they can be useful for identifying in the dominant flow quantities. One can construct a network of the ignition and failure of C1 for other quantities than the progress variable. For each quantity, the time at which the two ignition modes appear can be used to infer what causes the kernel breakdown. The networks and the time where the split occurs are shown in the Supplementary Material. Table 4.1 shows the time at which the two ignition paths appear for each quantity clustered. Here,

Table 4.1: Time instances at which the two ignition and failure path can be distinguished in the ignition network constructed by clustering the vorticity magnitude ω, the progress variable C and the mixture fraction Z.

	ω	C	Z
Ignition	0.08ms	0.3ms	0.6ms
Failure	0.08ms	0.25ms	0.4ms

the clustering is done for the vorticity magnitude (ω), the progress variable (C), the and mixture fraction (Z). It is found that the earliest path divergence (i.e., earliest recorded time when the highest probability paths of different modes go through different centroids) is observed in the vorticity field, whereas the latest divergence is observed in the mixture fraction field. Therefore, it can be concluded that the kernel breakdown is really due to a vortical structure that affects the kernel growth rather than a fuel-feeding mechanism.

To evaluate the effect of the kernel breakdown, the maximal temperature over the computational domain is tracked for C1 cases (Fig. 4.11). In cases of ignition success, the volume occupied by the products (defined as the volume of computational cells where $C > 0.1$), is also tracked (r.h.s. of Fig. 4.11). It can be observed that Mode 2 (kernel breakdown) leads to the most extreme ignition success and ignition failure events. If a failed ignition occurs, it is fastest when the kernel breaks. In cases of a failed ignition, the reaction rate is too slow to counteract mixing. Therefore, enhanced dissipation leads to faster ignition failure. Conversely, if the ignition is successful, the kernel breakdown leads to a high maximal temperature and larger fuel consumption. The larger kernel volume is not due to an earlier ignition since products always appear around the same time of $\mathcal{O}(\tau_{transit})$. Instead, the fuel consumption is more distributed in space. This effect of increasing turbulence was also observed in other studies [143], where larger integrated heat release was recorded in case of intense turbulence. The larger maximal temperature could be explained by a more intense fuel-kernel mixing which, in this case, overcomes the heat dissipation. In the past, it was found that

increasing turbulence could decrease the maximal temperature [144]. While this is also true on average here, the finer analysis conducted here reveals that turbulence can lead to high temperatures depending on the flow characteristics.

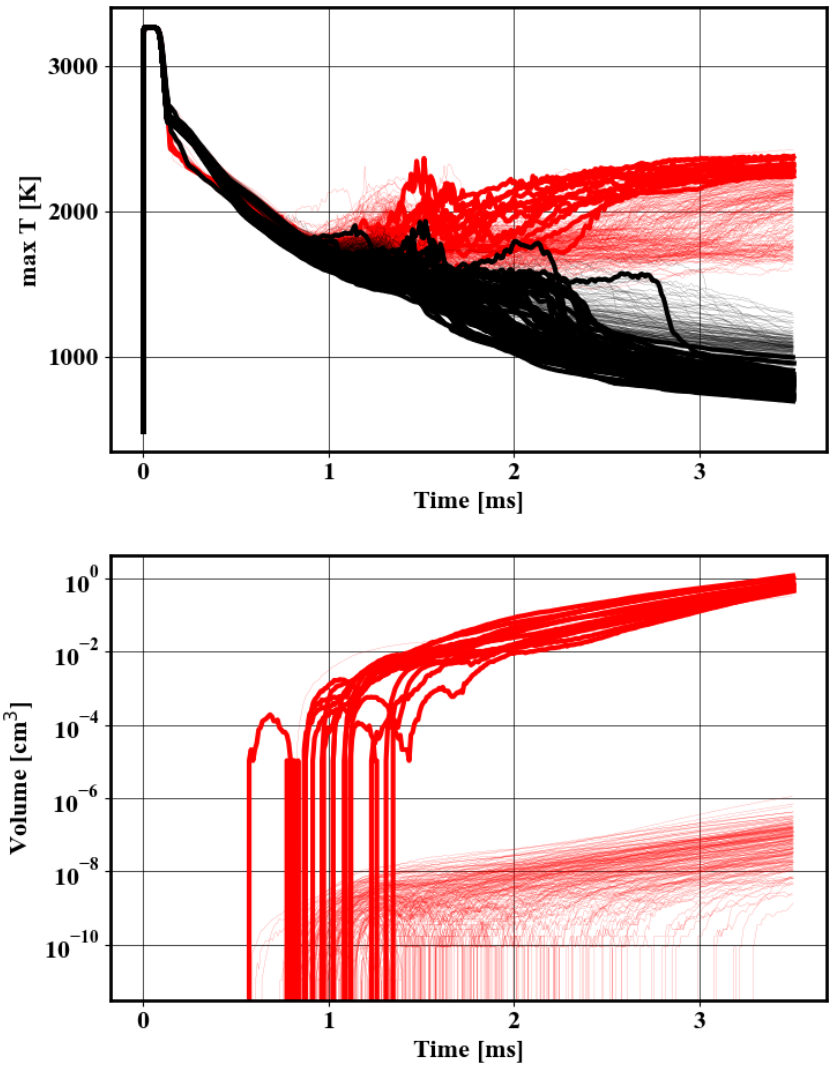

Figure 4.11: Left - time history of maximal field value of temperature for realizations labeled as ignition success (red) and ignition failure (black). Right - time history of the volume of flame kernel defined by the volume of computational cells with $C > 0.1$, for ignition success cases only. Thin lines denote Mode 1 (typical ignition schematic) and thick lines denote Mode 2 (kernel breakdown).

4.1.6 Summary and Conclusions

The realization-to-realization ignition variability of two realistic jet fuels (A2 and C1) observed with multiple LES simulations were analyzed using a range of data-driven analysis methods. The four highlights are as follows: (a) Using discriminant analysis combined with a sparse sensing approach, it is possible to identify that the entrainment of fuel in the kernel is crucial for the ignition of A2. (b) In the case of C1, the same discriminant analysis is not interpretable because the ignition was found to be dependent on the flame extinction through strain induced by small scale features. This finding highlights how the mechanisms that lead to ignition can be different for different fuels operated in the same geometry. Therefore, the design of aircraft engines regarding altitude relight may need to be revisited when alternative jet fuels are introduced. (c) With a data clustering analysis, it is found that two ignition success and failure modes can be observed for C1. One of the modes appears to be the result of an early kernel tilt which later results in kernel breakdown. Two ignition success and failure modes are also observed for A2, albeit being similar to each other. The difference lies in the strength of the ignition. (d) When the kernel breakdown occurs for C1, it leads to the most extreme ignition successes and failures. During ignition success, the kernel breakdown allows a distributed ignition over space and the kernel temperature is larger than when the breakdown does not occur. On average, ignition failure is more likely than ignition success when a kernel breakdown occurs.

The capabilities of the developed computational framework of turbulent non-premixed forced ignition are well-exploit and demonstrated in this study, where high-fidelity forced ignition data can be efficiently populated. Combined with state-of-the-art data-driven analysis, a detailed description of realization-to-realization variability for realistic jet fuel turbulent non-premixed forced ignition becomes possible and can be used in a realistic setting to refine the design of an aircraft engine. When com-

bined with the domain knowledge of the combustion process, these simulation and data analysis techniques provide extensive insight into the mechanisms that drive the ignition in such devices. An interesting extension is the application of these techniques to experimental data of gas turbine combustors, which will be pursued in the future.

4.2 Detailed Simulation of Aircraft Sunken Fire Igniter Discharge

In Section 2.1.3, it was discussed that conventional methods to represent the spark discharge as a volumetric energy source is challenged by the high-energy aircraft spark igniter discharge. As a result, an alternative approach (Sec. 2.1.3.2) is applied as the coupling between the ignition kernel and the turbulent flow field. Further, the distribution of the kernel parameter E_d is obtained using a calibration method (Sec. 2.2.3) during the ignition probability estimation. While these strategies are able to successfully reproduce the shape and dynamics of the PJICF kernel, as well as the final ignition probability, the methods rely on modeling parameters to be constrained by experimental data (e.g., Schlieren imaging and experiment measured ignition probability), which are not always available or may partially compromise the accuracy of the prediction. In this regard, the numerical capabilities that provide a forward prediction of the spark-induced kernel without targeting any of those experimental measurements by simulating the gas expansion process immediately following the spark discharge, would be ideal. Note that the igniter geometry and nominal discharge energy are still required in this case, but those can often be easily measured. Namely, from the aspect of prediction vs. calibration, which has been discussed in Sec. 2.3, it would be beneficial here if the spark deposit energy distribution can be predicted with existing numerical capabilities, which allows an important modeling

component to be treated as predictable instead of uncertain variable.

In this section, a preliminary study is presented to evaluate existing numerical capabilities in performing such a forward prediction. More specifically, the high-temperature gas expansion within the cavity of the target aircraft igniter is simulated using high-fidelity methods. Three commonly applied strategies are tested to resolve the issue of the temperature limit of the thermodynamic model when simulating the high-energy spark discharge. Preliminary results are shown for these methods along with a qualitative comparison against experimental measurements.

4.2.1 Experimental Configuration

4.2.1.1 Sunken fire igniter

The same target igniter applied in previous chapters is tested in this study. To isolate the spark discharge from other effects, the igniter is mounted in a quiescent environment of atmospheric condition (1 atm, room temperature), and is enshrouded in an acrylic tube as a protection measure in the corresponding experimental study [9]. A schematic of this configuration is shown in Fig. 4.12. As has been explained in Section 2.1.3.1, the configuration here features a sunken fire igniter, where the spark discharge takes place within a confined region, and the thermal expansion following the spark discharge would force a high energy flow pocket (i.e., the kernel) to be ejected into the domain. The high-fidelity simulation applied here aims to capture such effects. Note that while the external dimensions of the igniter are accurately known here, the inner dimensions are not known due to the proprietary design of the igniter. In this study, the inner dimensions are set based on a qualitative estimation by the experimental collaborator (Sfrozo, personal communication, 2019). The exact values are not presented since these simulations are qualitative in nature. Regardless, knowing the exact dimension is of secondary priority for this study, as the goal here is not to reproduce the quantitatively same spark-induced kernel, but to qualitatively

evaluate the performance of existing numerical capabilities.

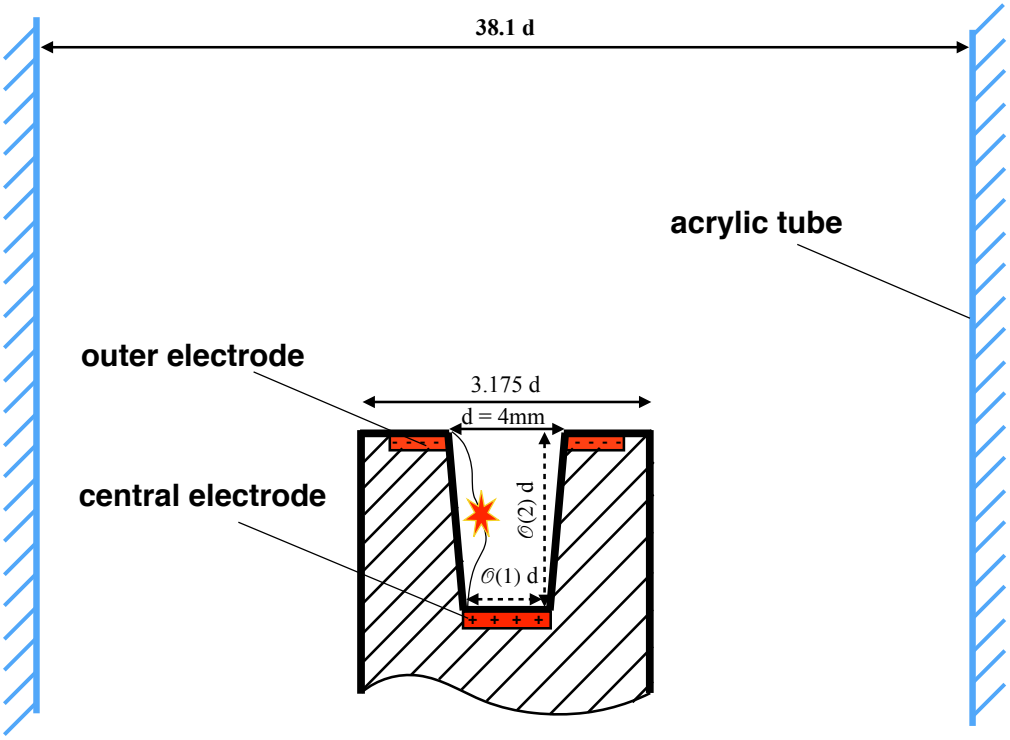

Figure 4.12: The target aircraft sunken fire igniter mounted in a quiescent environment.

4.2.1.2 X-ray diagnostics of kernel status

The x-ray diagnostic techniques applied in the experimental studies are briefly explained here for a better understanding of the experimental data. Due to the strong electromagnetic interference and light emission of the aircraft igniter discharge, conventional optical-based diagnostics are inapplicable to measure the kernel status shortly after the discharge. The x-ray beam is much less sensitive to scattering and can thus provide quantitative data inside optically incompatible flow fields, and is applied in the corresponding experimental study [9]. One feature of the x-ray measurement is that each measurement, which corresponds to a spark discharge, is a line-of-sight probe of the gas field taken at a fixed incident location. Therefore, it is impossible to record the spatial distribution of the kernel property from a single spark discharge

sequence with the x-ray beam. Instead, the spatial distribution is reconstructed on a raster grid of measurement points (see Fig. 4.13), where the time sequence of the spark discharge at each point is recorded, one point at a time. Further, to reduce the shot-to-shot uncertainties, the time histories at each point is measured as the ensemble average of multiple realizations of the spark discharge sequences. Therefore, the x-ray data depict neither the spatial nor temporal profile of the kernel for an individual discharge sequence, but instead the ensemble kernel behavior following the spark discharge.

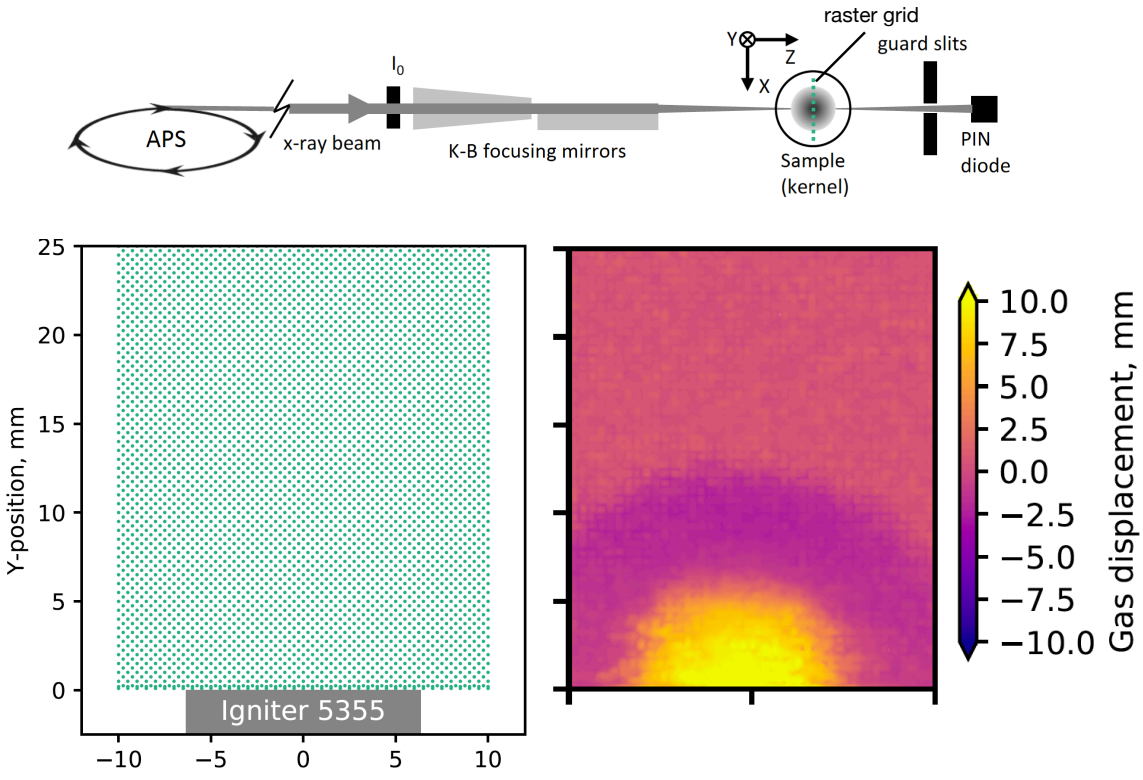

Figure 4.13: Illustration of x-ray diagnostics of kernel status reproduced from Ref. [9]. Top - top view of the x-ray radiography layout. Bottom-left - raster grid of experimental measurements. Bottom-right - a snapshot of the gas displacement contour reconstructed on the measurement grid using multiple spark discharges.

The direct output of the x-ray measurement is the decay of the light intensity of the x-ray beam along its pathway, which is then converted to the *gas displacement*

using the Beer-Lambert law [145], as

$$L{:}(x,y,t) = \int_0^l \frac{\rho_0 - \rho(z)}{\rho_0}\, dz = -\frac{1}{\mu\rho_0} \ln \frac{I_0(x,y)}{I(x,y,t)}. \tag{4.10}$$

Here, L is the gas displacement, μ is the photoelectric absorption coefficient, which applies a constant value in Ref. [9], I is the measured beam intensities, and ρ is the density. The subscript 0 denotes the baseline value measured from the ambient gas without the presence of the kernel.

The gas displacement L is a critical property that reveals the size, shape, and trajectory of the kernel. By the mathematical definition, L is dependent on the line-of-sight density variation induced by the kernel. Physically, $L > 0$ means gas expansion, $L < 0$ means compression, and in the most extreme condition, where the hot gas density approaches to zero (vacuum), L approaches the length of the vacuum space occupied by the kernel in the line-of-sight direction. Therefore, L is a measure of the kernel size. In this study, L is reconstructed as a time series of 2-D contours on the experimental measurement grid, which is applied to visualize the kernel shape and trajectory. An illustration of this visualization is provided in the bottom-right of Fig. 4.13. Further, the kernel size can be applied to evaluate the total amount of thermal energy carried by the kernel into the domain external to the igniter cavity [9]. Therefore, L is used in this study as the property to evaluate the performances of different spark discharge simulation strategies. The numerical version of the gas displacement is computed by post-processing the simulation output, which is explained in Section 4.2.2.3.

4.2.2 Numerical Methods

4.2.2.1 Simulation domain

A schematic of the simulation domain is shown in Fig. 4.14, which consists of a section of the experimental test tube with Neumann boundary conditions applied at both ends. In prior to the main simulations, preliminary simulations have been performed to determine the sufficient domain scale and grid resolution. A fixed grid embedding strategy is applied for mesh refinement, which is concentrated near the igniter tip, in particular, within the igniter cavity, which has the grid size of $\mathcal{O}(1.25 \times 10^{-4})$ m. The boundary condition at the wall features a non-slip velocity. As a

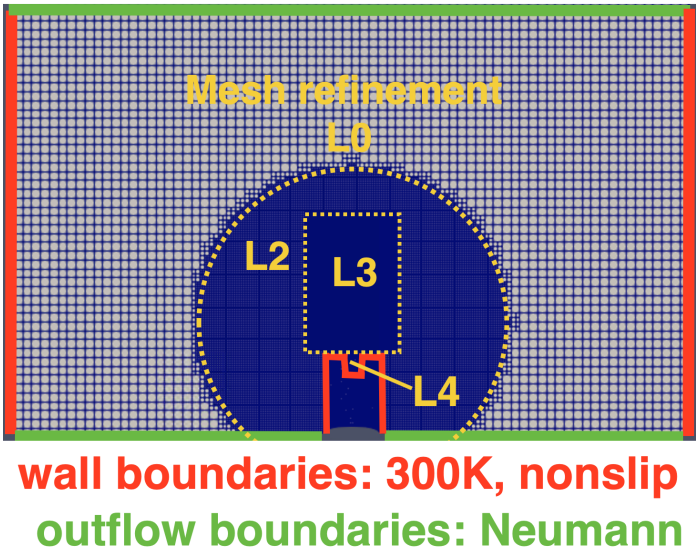

Figure 4.14: Schematic of simulation domain with pre-set, region-dependent grid refinements, with L0 and L4 being respectively the base grid and finest grid ($\mathcal{O}(2.5 \times 10^{-4})$). The rectangular region with L3 refinement corresponds to the x-ray measurement window.

preliminary case, a fixed temperature of 300 K is applied at the igniter surface, while a more realistic setup should consider conjugate heat transfer due to the presence of high-temperature gas. The simulation is initialized from quiescent flow at atmospheric conditions. The flow motion is driven by the thermal expansion induced by the energy rise, which is introduced into the simulation domain, at the beginning of the

simulation with details to be explained in Sec. 4.2.3.

4.2.2.2 CFD solver & Flow Modeling

A density-based compressible solver implemented in the commercial CFD platform CONVERGE [146] is used. The transport equations for mass, momentum, species, and total energy are solved in the LES framework. The dynamic Smagorinsky model [89] is applied to provide closures for the LES equations. The pressure-velocity coupling is achieved using the PISO algorithm [99] and a compressible pressure correction equation. A second-order-accurate spatial discretization scheme [147] is used for the governing equations with a fully-implicit first-order-accurate time integration scheme. The time step during the simulation was automatically determined based on the Courant-Friedrichs-Levy (CFL) numbers defined by the speed of sound, which is constrained to be lower than 1.0. The solver along with similar setups has been successfully applied to simulate high-temperature, high-speed flows that include discontinuities [148], which is similar to the test case here.

The equation of state of the gas mixture is closed using the ideal gas assumption. As a starting point, the gas phase is treated as a non-reacting mixture of O2 and N2, while more realistic effects require the inclusion of reactions of thermal dissociation/ionization. The thermodynamic modeling applies the polynomial fittings from the NASA CEA [149], which is defined up to $20,000$ K. Such modeling closures serve as the best available approximations that are compatible with existing combustion simulation frameworks. Further improving the modeling fidelity (e.g., the inclusion of thermal-non equilibrium, plasma kinetics) would be nontrivial, which requires professional knowledge of high-energy plasma and additional coupling between the "non-conventional" thermodynamic model with the "conventional" combustion simulation framework. For the scope of this study, the goal is to evaluate the best performance of the existing modeling strategies without such additional efforts. Regarding this,

more details are discussed the Section 4.2.3.

4.2.2.3 Post-processing techniques

To compare the simulation results against the experimental x-ray data introduced in Sec. 4.2.1.2, the numerical gas displacement needs to be reconstructed. For this purpose, the line-of-sight integration in Eq. 4.10 is calculated using the simulation output density field. To enable the line-of-sight integration calculation, the simulation density field is mapped onto a structured grid with one of the local grid coordinates aligned with the line-of-sight integration direction. The resulting integration output is therefore the numerical gas displacement measured from one incident angle.

Since the CFD simulation is deterministic, the output is not directly comparable to the ensemble kernel behavior of the x-ray data, which is the ensemble result of multiple spark discharge sequences. To partially resolve this issue while maintaining a low computational cost, the uncertainties associated with the spark discharge process is assumed to be only contributed from the variability in the position where the electric arc channel is formed. More specifically, the initial arc channel is assumed to follow a uniform distribution around the circumference of the igniter inner side wall (more details presented in Sec. 4.2.3). Then, by taking advantage of the symmetry of the geometry, the ensemble gas displacement can be approximated by averaging the numerical property reconstructed from a single simulation but using a discrete series of incident angles, as illustrated in Fig. 4.15.

4.2.3 Test Cases of Different Energy Deposition Strategies

Unless the simulation includes a thermal non-equilibrium modeling of the high-temperature plasma, existing energy deposition methods in a spark discharge ignition simulation will encounter the issue of energy breach. Namely, the energy density at the early phase of spark discharge is higher than the upper energy limit of the

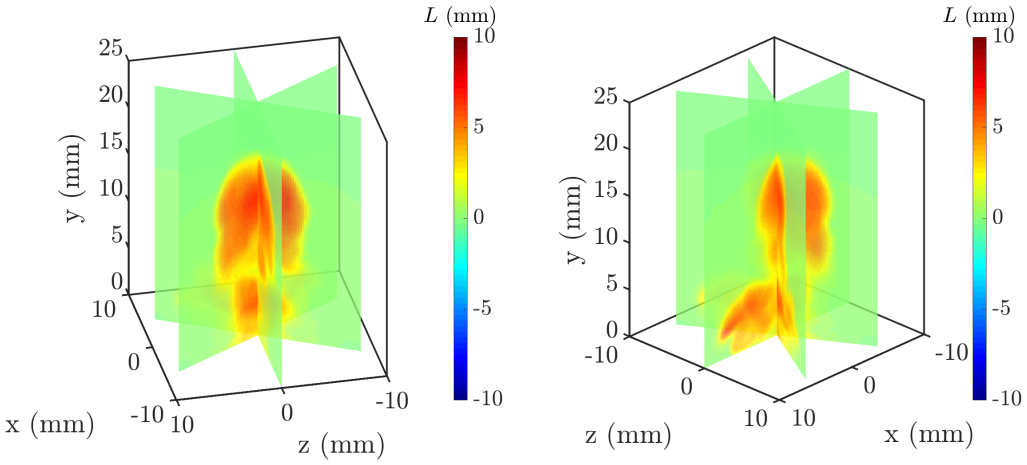

Figure 4.15: Numerical gas displacement measured from different incident angles. A total number of 3 incident angles are shown (3 cutting planes). The same 3-D schematic is plotted from two viewing angles (left and right) to provide a better illustration. In the actual post-processing, the final ensemble gas displacement is calculated as arithmetic average of the property measured from a total number of 60 incident angles.

thermodynamic model, which needs to be avoided as the simulation will either make unreliable predictions or even fail due to the non-physical thermodynamic properties extrapolated outside the upper thermodynamic limit. This section briefly discusses commonly applied strategies that resolve the issue within the conventional combustion simulation framework.

Based on the spatial distribution of the imposed energy source, the ED strategies can be categorized mainly into: (a) a line source; (b) a volume source. The line source deposits the spark discharge energy into the computational cells overlaps with the electric arc channel, which can be either prescribed or tracked using Lagrangian particles. Due to practical concerns of computational cost, the applied computational control volumes that overlap with the electrical arc often have a cell size greater than the arc channel radius $\mathcal{O}(0.1)$ mm [100], which is theoretically improper for resolving the shape of the arc channel, but technically mitigates the issue of energy breach as the effective radius of the channel becomes greater than actual physics. The volume source, on the other hand, deposit the spark discharge energy into a spatial region

occupied by the kernel expanded from the initial electric breakdown, which is often prescribed based on the observed or presumed shape of the kernel at a certain time after the discharge. Therefore, the line source is more physical than the volume source in terms of better retaining the initial shape of the kernel. However, the line source also faces a higher risk of energy breach compared to the volume source, as the spark discharge energy is initially deposited into a much smaller volume.

Apart from adjusting the spatial distribution of the ED energy source, other auxiliary methods help overcome the energy breach. One straightforward method is to simply clip off the energy source when the local energy is about to breach the upper energy limit of the thermodynamic model. This method is implementation friendly, and is the default option in CONVERGE, which is here referred to as "harsh energy clipping". The harsh energy clipping along with the line source has been used to successfully model the IC engine spark discharge [100], where the spark nominal energy is much lower than that in this study. Here, the harsh energy clipping may lead to non-physical results by removing too large of a portion of the energy. Another more physical method is simply to allow the energy to breach and later relax to a lower value via thermal expansion and heat dissipation. As for the thermodynamic modeling, all the other energy-dependent thermodynamic properties are clipped at the upper energy limit during the energy breach. This method is referred to here as the "soft energy clipping", as it is capable of conserving the correct amount of transported energy within the domain.

Based on the above discussions, a total number of three ED strategies are tested in this study, as listed in Table. 4.2. Case I and II applies a line source, but each with a different energy clipping method of harsh and soft, respectively. Case III applies a volume source. For Case I and II, the discharge profile applies a constant power profile of 1.24 J of energy over 40 μs [5]. The line source geometry is prescribed at a fixed displacement within the igniter cavity. In reality, the arc channel has curvature

and can be elongated due to flow motion. Here, since little prior information is provided for the physics within the igniter cavity, the line source here is assumed to be a straight line displaced along the inner side wall of the igniter. For Case III, the same 1.24 J amount of energy is uniformly distributed within a cylindrical region inside the igniter cavity. The volume of this region is relaxed to a critical value estimating using a constant volume PSR calculation, which leads to a post-discharge temperature just below the upper temperature (energy) limit of the thermodynamic model. The critical volume is found to be 4.1×10^{-8} m^3, which is close to the entire igniter cavity volume. In comparison, the effective volume of the line source in Case I and II are only about 4×10^{-10} m^3. Besides, the discharge of the volume source in Case III is set to be infinity fast. This is to "freeze" the flow field during the energy deposition to avoid the energy breach induced by the local density drop - an effect that cannot be taken into account by the PSR calculation.

Table 4.2: Energy deposition strategies applied in different test cases.

Case ID	Source Distribution	Energy Breach Treatment	Discharge Profile
I	line source	harsh energy clip	const power
II	line source	soft energy clip	const power
III	volume source	critical volume estimated from const volume PSR calculation	infinitely fast

4.2.4 Preliminary Results

Only preliminary results are currently available. The first part of the results shows a qualitative comparison of the pulsing kernel shape and trajectory compared against the x-ray measurement using the three different ED strategies. The second part shows an analysis of the thermal expansion process and energy loss via the igniter surfaces.

4.2.4.1 Kernel shape and trajectories predicted by different ED strategies

The time sequence of gas displacement contour obtained from the x-ray diagnostics and simulation cases with energy deposition strategies are plotted in Fig. 4.16. The x-ray data provides a global view of the post-discharge kernel evolution. At $t = 7$ μs after the discharge, the kernel top just emerged from the spark gap on the igniter top surface ($y = 0$ mm), prevailing the kernel (positive gas displacement) is a shock wave (negative gas displacement), which is formed due to compression effects induced by the drastic density ratio introduced by the spark-induced thermal expansion. It is clarified that the compression region behind the shock in the gas displacement appears to be greater than actual (e.g. at 25 μs), which is due to the line-of-sight effects. The actual density field features a sharp discontinuity at the shock front with a post-shock compression weaker than suggested by the gas displacement contour (see Fig. 4.18). It can be seen that the distance between the kernel boundary and the wave front is quickly widened as time progresses. This observation supports the low-Mach treatment applied in the developed LES forced ignition simulation platform (Section 2.1.2), as the separation of time scale between the shock wave and the kernel propagation allows the downstream reaction to being isolated from the compression effects. For instance, in the target configuration, by the time when the reaction is initiated ($\mathcal{O}(1)$ ms, as in Sec. 3.2.3.1) the shock front has propagated to a distance far away from the kernel (out of the measurement window). As time further progresses, the kernel penetrates further into the domain, retaining approximately the same shape while becoming smaller in size. Besides, the kernel boundary becomes more blurred out, and there is a trace of density disturbances in the wake of the pulsing kernel. Note that those effects are partially due to turbulent dissipation and partially due to the uncertainties of the individual discharge sequence contributed to the ensemble x-ray results.

In Case I, the size of the kernel is heavily underpredicted, as well the intensity of

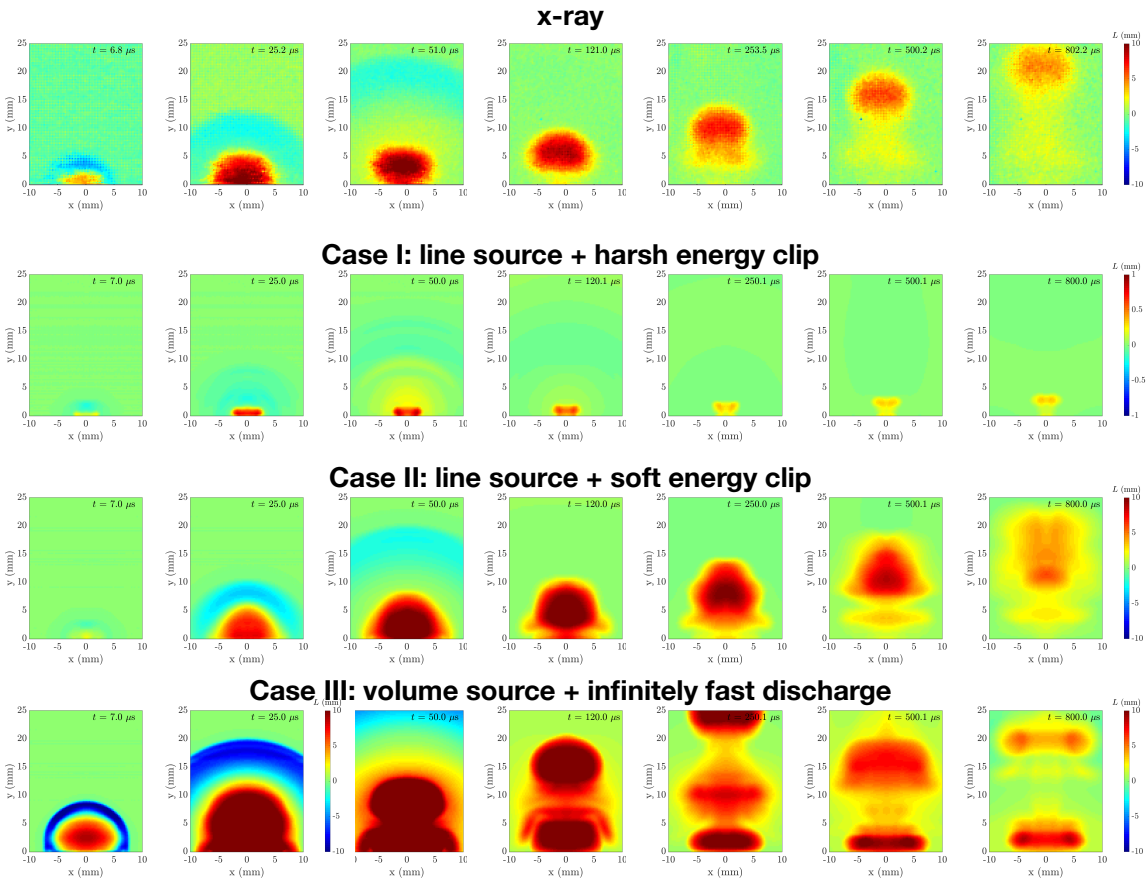

Figure 4.16: Time sequence of gas displacement contour obtained from x-ray diagnostics and simulations cases with different energy deposition strategies.

the shock wave. The result is therefore qualitatively incomparable with the experimental data. This proves the previous assumption that the harsh energy clipping would trim off too much energy in the case of the target aircraft igniter discharge.

In Case II, the numerical results are in qualitative comparison with the experimental data in terms of both the early stage kernel shape and the intensity and propagation of the shock wave. As time progresses, the predicted kernel shape becomes less comparable against experimental data, especially for the time at 800 μs, where the kernel appears to be heavily distorted in the radial direction at its upper part such that the azimuthal average appears to be of a lower gas displacement at the inner radius region than that at the outer radius region. However, considering the complex physics associated with the process, and, in particular, the uncertainties in the igniter inner geometry, the result is satisfactory.

For Case III, the "intensity" of the spark discharge is qualitatively over-predicted. More specifically, the size of the kernel is over-predicted as well as the density ratio across the shock wave. This over-prediction is more than an equivalent time shift to cancel out the applied infinitely fast discharge, where the result will still be over-predicted. More likely, the over-predicting of kernel size and density change is due to the constant volume PSR calculation. Consider the two types of PSR calculation - the constant pressure PSR and the constant volume PSR, the former calculation allows the kernel to freely expand by completely ignoring the comprehensibility effects, while the latter does not allow the kernel to expand at all. For the gas expansion process immediately following the electric arc, the actual physics should be somewhere in between the two calculations. In this regard, an improved method is to use the volume source with the constant power discharge profile to simulate the actual expansion physics and use the soft energy clipping to handle the potential energy breach, which is considered as a future study.

4.2.4.2 Physics of sunken fire igniter discharge

As Case II best reproduces the pulsing kernel in the above section, the analysis of the sunken fire igniter discharge process within the igniter cavity is interrogated using the Case II result. The time series of mid-plane density contour is shown plotted in Fig. 4.18 at the early stage of the spark discharge. The time series reveals

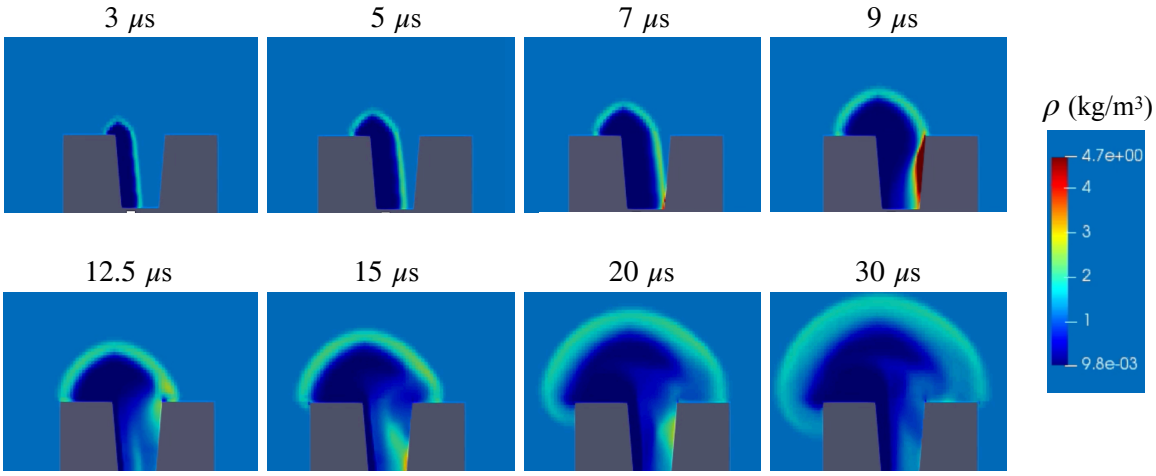

Figure 4.17: Time sequence of mid-plane density contour within the igniter cavity obtained from Case II simulation.

the expansion of the kernel from the electric arc channel (left) to the other side of the inner wall (right). Upon reaching the other wall (9 μs), the shock wave is reflected within the igniter, possibly for multiple times before eventually being dissipated out (30 μs). The top part of the expanding kernel moves upward, forming a hemispherical shape with an asymmetry effect that becomes more prominent as time progresses. Note that the minimum density allowed in the simulation is clipped at $20,000$ K due to the soft energy clipping, in this sense the actual expansion process is not necessarily the same as that predicted here.

The discharge process here also features significant wall heat loss, which is found to be 0.2 J in Case II. Moreover, and unsurprisingly, the wall heat loss here is sensitive to the upper-temperature limit allowed in the thermodynamic model. For instance,

in another test case where the maximum temperature is allowed to go to an artificial value of 90, 000 K (by extrapolating the local temperature beyond the thermodynamic limit using the last available data point of specific gas constant C_p), the wall heat loss is found to be 0.5 J, which is a significant portion of the total 1.24 J. The resulting kernel size in such a case is therefore much smaller than that in Case II, as shown in Fig. 4.18. This suggests that a quantitative prediction of right kernel energy is infeasible with the existing conventional combustion simulation platform.

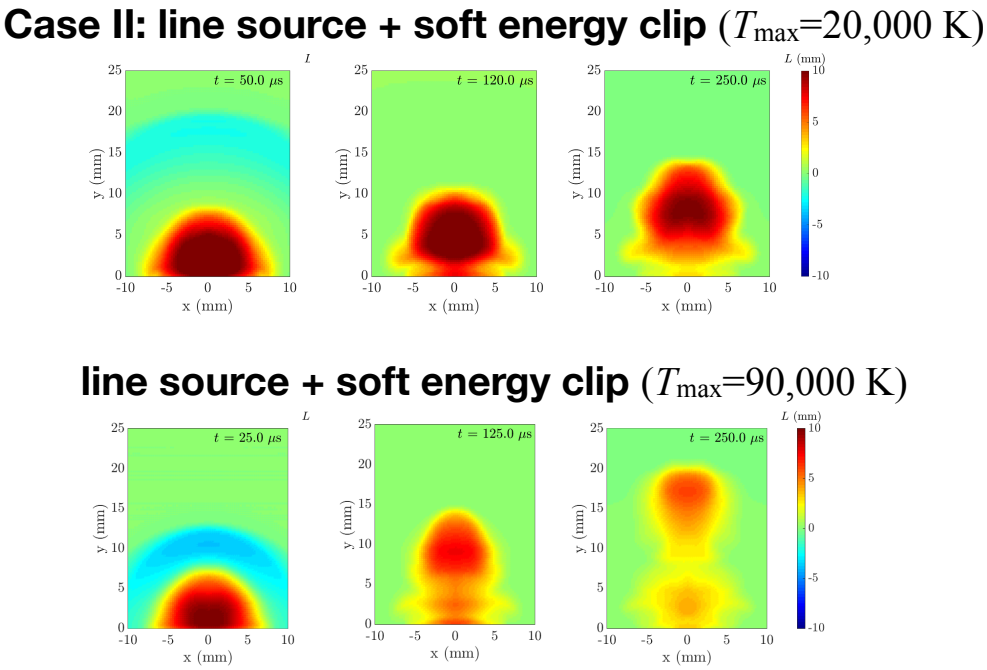

Figure 4.18: Time sequence of gas displacement contour compared in between results predicted by the energy soft clipping at the original upper energy limit of the thermodynamic model and that at an artificially high temperature extrapolated beyond the upper energy limit.

4.2.5 Summary

A detailed simulation is performed to predict the pulsing kernel produced from the aircraft sunken fire igniter discharge tested in previous chapters. A total number of three energy deposition strategies that address the issue of energy breach are

tested. Preliminary conclusions are as follows. (a) The line source combined with the soft energy clipping is able to qualitatively reproduce the shock propagation and kernel pulsing. (b) While the detailed simulation of the post-discharge kernel expansion is capable of providing a qualitative understanding of the early stage gas expansion process following the spark discharge, the robustness of existing simulation capabilities in predicting the correct amount of wall heat loss as well as kernel energy remains questionable. (c) Under the high-energy sparking effects, the early stage kernel evolution involves complex physics of conjugate heat transfer, radiation, and thermal non-equilibrium, all these factors make it difficult to make an accurate forward prediction on the amount of energy that eventually enters the pulsing kernel.

In light of these observations, the currently available options for evaluating the kernel or spark deposit energy of the aircraft sunken fire igniter should be based on experimental information, which can be either a direct probe of the kernel status (e.g. x-ray diagnostics) or some other properties that implicitly contain such information (e.g., the calibration of spark deposit energy distribution Section 2.2.3 using the experimental ignition probability).

CHAPTER V

Summary

5.1 Summary of Findings

In this study, a computational framework is developed and validated for predicting the turbulent non-premixed forced ignitions in altitude relight. A detailed list of main points is below.

Chapter I:

In this chapter, key numerical challenges are identified.

1. The fundamental physics of altitude relight are forced ignitions that involve non-local fuel entrainment and turbulent strain quenching.

2. The forced ignition problem here features a chaotic process that can only be described statistically.

3. Existing forced ignition models based on semi-empirical relations cannot be directly applied to altitude relight.

Chapter II:

In this chapter, the computational framework is developed.

1. A hybrid tabulation strategy is applied to include both physics of forced ignition and flame propagation.

2. A specialized kernel initialization strategy is applied to reproduce the aircraft igniter discharge effects.

3. A modeling procedure based on Monte-Carlo sampling, polynomial chaos expansion, and presumed-shaped PDF distribution calibration is applied to estimate the ignition probability.

4. Regardless of individual ignition outcome or the statistical behavior, the proposed modeling is predictive, in terms of evaluating the ignition physics given a kernel status after the initial thermal expansion, but calibrated, in terms of evaluating this initial kernel status.

Chapter III:

In this chapter, the computational framework is validated using a forced ignition rig that represents altitude relight scenarios.

1. The LES simulation captures the kernel vortex dynamics and fuel entrainment qualitatively comparable with experiment and DNS data.

2. The LES simulation captures the variability of ignition outcomes due to perturbations in both background turbulence and the spark discharge.

3. The LES simulation predicts the early-stage OH species evolution comparable to DNS data.

4. For the target configuration, the LES simulation predicts the complete forced ignition process to exhibit a 3-phase pattern, which is partially supported by experimental flame kernel area history.

5. The numerical ignition probabilities are quantitatively comparable with experimental data over a wide range of operating conditions.

6. The computational framework achieved a computational efficiency to afford numerical predictions of ignition probability based on reacting flow simulation.

Chapter IV:

In this chapter, two supplemental studies are carried out.

The first study applied the developed computational framework and data-driven analysis to understand the impact of turbulence on the ignition process.

1. Using discriminant analysis, the entrainment of fuel in the kernel is identified to be crucial for the ignition of the A2 fuel.

2. The same discriminant analysis was not possible for the C1 fuel, where the flame extinction was found to be dependent on strain induced by small scale features.

3. With a data clustering analysis, two different ignition modes can be observed for the C1 fuel, with one resulting in a flame kernel breakdown. The observed modes are similar to each other for the A2 fuel.

4. When the flame kernel breakdown occurs for C1, it leads to the most extreme ignition successes and failures.

The second study evaluated existing numerical capabilities in reproducing the early-stage kernel evolution immediately following the aircraft igniter discharge.

1. The line-shaped energy source combined with the proposed soft energy clipping strategy is able to qualitatively reproduce the shock propagation and kernel pulsing.

2. While the detailed simulation qualitatively captures the kernel pulsing effect following the spark discharge, the accuracy remains questionable.

5.2 Conclusion

The computational framework developed in this thesis provides a novel approach for predicting the forced ignition process in high-altitude relight. The general conclusions and lessons learned from this dissertation are provided below.

While forced ignition has been explored combustion literature, it is still not well understood. Depending on the specific configuration, the dominant physics can be vastly different, requiring careful choice of modeling strategy. For altitude relight applications, the core modeling challenges here are the effects of non-local fuel entrainment and turbulent strain, which can disrupt the otherwise monotonic relationship between the initial kernel status and ignition outcome. Existing ignition models based on semi-empirical relations are not applicable here, as those are derived from simple ignition configurations and modeling assumptions that do not include such effects.

Moreover, aircraft relight is different from internal combustion engines due to the non-local nature of the flame processes. In internal combustion engines, the spark is directly applied to fuel-air mixture. However, in forced ignition considered here, the spark is dischared into air, and has to travel a finite distance before reaching the fuel-air mixture. To capture both non-localized ignition and turbulent flame quenching, the modeling strategy here applies an LES tabulated detailed chemistry model that includes the reaction kinetics of the entire forced ignition process, i.e., from early-stage kernel reaction to later stage flame propagation. A hybrid tabulation of homogeneous reaction (HR) and flamelet progress variable approach (FPVA) is developed. The HR tabulation approximates the forced ignition to be a locally-quasi zero-dimensional reaction, whereas the FPVA tabulation models the non-premixed turbulent flame propagation by the popular flamelet assumption. Besides, a kernel initialization strategy specialized for aircraft igniter discharge is developed, to reproduce the pulsing effect of the spark-induced kernel. Together, these components

constitute the proposed simulation platform.

Apart from simulating forced ignition with sufficient fidelity, another critical goal is to predict the ignition probability, as the target problem is sensitive to stochastic events. The ignition probability estimation presented in this study features a comprehensive modeling procedure that includes the uncertainties associated with both the igniter discharge and the turbulence, along with a rigorous quantification of the estimated modeling uncertainties. A Monte-Carlo sampling using multiple forced ignition LES simulations is first applied to predict the ignition probability conditioned on the spark deposit energy. The final ignition probability is then predicted, as the integration of this conditional ignition probability and the statistical distribution of the spark deposit energy.

In this context, it is found that calibrating spark discharge using one set of experiments does not diminish predictive accuracy at other flow conditions. This, in itself, is a useful conclusion since it provides a way forward for independently characterizing igniters.

The proposed framework provides a level of fidelity that cannot be reached by conventional approaches that rely on flame-surface patching or other semi-empirical methods. The variation in spark deposit energy, which is often neglected in previous approaches, is shown here to be a critical factor that affects the individual ignition outcome. In terms of predicting ignition probability, by including the uncertainties associated with both turbulence and the spark discharge, the probability predictions here are shown to be highly accurate. Moreover, in the cross-validation study, the proposed ignition probability modeling has shown consistent prediction accuracy that is insensitive to the calibration procedure. Lastly, for the first time, the computational efficiency has been significantly advanced so that ignition probability prediction based on detailed reacting flow simulation has become feasible..

This computational approach can be further utilized for data-driven analysis by

generating large amounts of forced ignition data. A demonstration is presented by applying such analysis to study the impact of turbulence on the ignition process, where the ignition of different jet fuels is found to be affected by different turbulent scale features. An interesting pattern of the ignition process is also identified for one of the tested jet fuels, which features a flame kernel breakdown that is uncommonly seen among the generated ignition samples but can greatly affect the ignition outcome. It is noted that such analyses cannot be treated as fully validated conclusions yet, since the simulations utilize models for different processes. However, combined with expert knowledge of the fundamental physics, such analyses still provide extensive insight into the mechanisms that drive forced ignition in the altitude relight problem.

While considerable advances have been made in this thesis, the topic of modeling forced ignition in altitude relight is far from being fully completed. In the next section, possible future research efforts are presented.

5.3 Future Study

This thesis develops a computational framework that includes many aspects of the practical altitude relight problems. Realistic problems are always more sophisticated, requiring future efforts to pursue further improving the numerical capabilities. A few recommendations are proposed here based on the best understandings of the author.

5.3.1 Modeling Forced Ignition with Liquid Fuel Spray

As mentioned in the introduction of this thesis, the effects of liquid fuel spray is an important factor in practical altitude relight problems. While existing methods are abundant for liquid spray modeling, the coupling between the gas phase combustion model may need to be re-designed in the case of spark ignition. For example, while the aircraft igniter is displaced at the edge of the primary zone of the aircraft combustor, there are chances that a liquid fuel droplet can directly interact with an electric spark

discharge (especially for altitude relight, where the liquid fuel becomes difficult to be atomized). Under such circumstances, the evaporation of the droplet as well the ignition of the gas fuel could be different from conventional spray combustion where the droplet is only be heated by the gas phase.

5.3.2 Detailed Modeling of the Spark Discharge

The coupling of the spark-induced kernel and the turbulent flow field is an important topic that has been addressed multiple times in this thesis. There are still modeling components that await further improvement, mainly in the two aspects of (a) measurement-constrained field initialization approach and (b) forward modeling approach.

Before considering a more sophisticated modeling strategy, gaining a better understanding of existing capabilities is always helpful. While this study has successfully applied experimental constrained boundary profiles to reproduce the pulsing kernel introduced by the spark discharge, there are still many approximations and imperfections in the developed strategy. An in-depth study of how the ignition kernel should be initialized using a commonly available experimental dataset, including how to better represent the uncertainties associated with the kernel will be helpful.

As has been discussed in the second supplemental study, to provide a forward prediction of the kernel expansion during and immediately following the aircraft igniter spark discharge requires the inclusion of non-equilibrium modeling of the high-temperature plasma. Unless such prediction capabilities are developed, it is always difficult to make an accurate initialization of the spark-induced kernel solely based on nominal igniter spark properties (e.g., the electrode shape and electrical power histories). In this regard, there are abundant previous studies related to the high-temperature plasma that can be borrowed from. The immediate challenge is to build a computational framework that incorporates both non-equilibrium plasma and con-

ventional combustion simulation and provides the proper coupling between the two models. As always, finding the balance between modeling fidelity and modeling complexity (prediction and calibration) is critical.

5.3.3 Computational Efficiency Improvement

While the developed computational framework has achieved computation efficiency comparable to cold flow LES simulations, the computational cost to predict ignition probability is still not sufficiently low to simulate the forced ignition in a realistic aircraft combustorIn this regard, the following two directions are suggested to develop a more computationally efficient model.

Firstly, in the first supplemental study, the data-driven analysis has shown promising capabilities in identifying flow features that promote/suppress ignition. Following this idea, it is worth considering a multi-fidelity computation framework that applies a detailed CFD simulation as the high-fidelity prediction along with a classification model that can be trained on-the-fly as the low-fidelity prediction.

Secondly, while existing semi-empirical models based on cold flow LES are unsuitable for capturing the detailed fuel entrainment mechanism of the pulsing kernel and the non-localized ignition in some of the forced ignition problems, those models are still strongly competitive modeling candidates for providing fast estimations of turbulent forced ignitions. For example, for the well-known flame particle model, with additional modeling component being added. For example, by providing the flame particles with thermal memory, developing strategies to include detailed modeling of the fuel entrainment into the pulsing kernel, and developing better empirical criteria for realistic jet fuels, the model can potentially be adjusted to simulate non-localized forced ignition problem in altitude relight. In this regard, such models should not be overlooked and studies that pursue further improving them can always be helpful.

5.4 Outlook

With growing computational power, one of the future direction is to apply numerical simulations of full-scale aircraft engine altitude relight to assist the engine design. With advancing artificial intelligence technology, conventional combustion models, not necessarily just for forced ignition modeling, could be replaced by AI models.

Meanwhile, there are still huge gaps between current numerical studies and the full-scale altitude relight engine test. For instance, forced ignition behavior is often studied under ground-conditions. Also, the interference of ignition processes following multiple spark discharges are rarely simulated. In a short-term view, these gaps are to be filled.

Before radical changes will be brought to the world of computational science, applying high-fidelity computational simulation using models developed based on fundamental physics will continue to serve as a mid-term resolution.

Publications in PhD Study

- **Journal papers**

    1. **Data-driven Analysis of Relight variability of Jet Fuels induced by Turbulence**, M. Hassanaly, Y. Tang, S. Barway, V. Raman, *Combustion and Flame*, 225, 453-467, 2021.
    2. **Numerical investigation of pressure effects on soot formation in laminar coflow ethylene/air diffusion flames**, J. Guo, Y. Tang, V. Raman, H. Im, *Fuel*, 2021 (Accepted).
    3. **Probabilistic Modeling of Forced Ignition of Alternative Jet Fuels**, Y. Tang, M. Hassanaly, V. Raman, B. Sforzo, J. Seitzman, *Proceedings of the Combustion Institute*, 2020, doi: 10.1016/j.proci.2020.06.309.

4. **A Comprehensive Modeling Procedure for Estimating Statistical Properties of Forced Ignition**, Y. Tang, M. Hassanaly, V. Raman, B. Sforzo, J. Seitzman, *Combustion and Flame*, 206, 158-176, 2019.

- **Conference papers**

1. **An analysis of soot formation pathways in laminar coflow ethylene flames at higher pressures**, J. Guo, P. Selvaraj, H. Im, Y. Tang, V. Raman, *AIAA SciTech Forum*, AIAA 2020-1660, 2020.
2. **Soot formation in toluene-doped ethylene laminar diffusion flames**, J. Guo, Y. Tang, P. Selvaraj, C. Shao, A. Bennett, V. Raman, W. L. Roberts, S. M. Sarathy, H. G. Im, *16th International Conference on Flow Dynamics*, 2019.
3. **Analysis of the effect of turbulence on aircraft engine ignition using multiple large eddy simulations (LES)**, M. Hassanaly, Y. Tang, S. Barway, V.Raman, *11th Mediterranean Combustion Symposium*, 2019.
4. **Numerical simulation of forced ignition of Jet-fuel/air using large eddy simulation (LES) and a tabulation-based ignition**, Y. Tang, M. Hassanaly, V. Raman, B. Sforzo, J. Seitzman, *AIAA SciTech Forum*, AIAA 2019-2242, 2019.
5. **Simulation of Gas Turbine Ignition Using Large Eddy Simulation Approach**, Y. Tang, M. Hassanaly, V. Raman, B. Sforzo, S. Wei, J. Seitzman, *ASME Turbo Expo 2018: Turbomachinery Technical Conference and Exposition*, 2018.
6. **Turbulent Mixing and Combustion of Supercritical Jets**, S. T. Chong, Y. Tang, M. Hassanaly, V. Raman, *AIAA SciTech Forum*, AIAA 2017-0141, 2017.

7. **Numerical Study on Flame Stabilization Mechanism of a Multi-jet Burner with LES Flamelet Approach**, Y. Tang, H. Koo, C. Leitz, V. Raman, *AIAA SciTech Forum*, AIAA 2016-1395, 2016.

- **In preparation**

1. **National Jet Fuel Combustion Program, Chapter XI: CFD Modeling of Lean Blowout and Ignition Fuel Sensitivity**, M.S. Anand, et al., *American Institute of Aeronautics and Astronautics Inc.*.
2. **LES flamelet approach for non-adiabatic, strained premixed combustion**, Y. Tang, V. Raman, *Combustion and Flame*.
3. **Early-stage Kernel Evolution of an Aircraft Spark Igniter Discharge**, Y. Tang, J. Kim, B. Sforzo, R Scarcelli, S. Som, V. Raman, *Journal of Propulsion and Power*
4. **Detailed Investigation of High-Swirl Stratified Flame Flashback using LES Non-Adiabatic Tabulated Chemistry Approach**, X. Jiang, Y. Tang, V. Raman, *Entropy*.

APPENDICES

APPENDIX A

Data-driven Analysis of Turbulent Induced Ignition Variability

A.1 Justifying the realization-to-realization approach

To begin with, detailed information on the turbulent properties of the cold flow (initial conditions) are provided in Tab. A.1. The values here are averaged over space and also over the ensemble of realizations. The turbulent dissipation rate is calculated as

$$\varepsilon = 2\nu\langle s_{ij}s_{ij}\rangle, \tag{A.1}$$

where, $s_{ij} = \frac{\partial\widetilde{U}_i}{\partial x_j}$, and $\widetilde{U}_i$ is the i component of the filtered velocity, and ν is the kinematic viscosity. The Kolmogorov timescale is defined as

$$\tau_\eta = \sqrt{\frac{\nu}{\varepsilon}}, \tag{A.2}$$

the integral timescale is defined as

$$\tau_{int} = \frac{k}{\varepsilon}, \tag{A.3}$$

and the Taylor microscale Reynolds number is approximated as

$$Re_\lambda = \sqrt{\frac{20}{3}\frac{k^2}{\varepsilon\nu}}. \tag{A.4}$$

Table A.1: Turbulent properties averaged over space and over the initial conditions. Error bounds indicate root mean square fluctuations over the realizations.

	k ($\mathrm{m}^2.\mathrm{s}^{-2}$)	ε ($\mathrm{m}^3.\mathrm{s}^{-2}$)	τ_η (ms)	τ_{int} (ms)	Re_λ
C1	0.448 ± 0.032	46.38 ± 3.19	2.31 ± 0.096	56.5 ± 4.9	52 ± 3.7
A2	0.446 ± 0.032	46.5 ± 3.1	2.33 ± 0.096	55 ± 4.9	50.6 ± 3.6

Due to the chaoticity of turbulence, the LES simulations cannot, in general, be used to investigate individual realizations [123]. Over time, any small scale errors including sub-filter scale approximations amplify until they dominate the flow field [150, 151]. The growth of sub-filter scale errors during an ignition realization is analyzed below.

First, the sub-filter errors grow in magnitude at a certain rate (the Lyapunov exponent) [152, 153], which should be compared to the simulation time of the forced ignition process. The rate of growth of perturbations is estimated using the method in [152], where a relationship between the perturbation growth rate and Re_λ is provided. It can found that the sub-filter errors would grow at the exponential rate of e^{42t} for both the C1 and A2 fuel. For the LES simulation time here, (3.5 ms, which is sufficient to distinguish between a successful and a failed ignition), the corresponding error would have grown by only 15%. By the end of the LES forced ignition simulation, the sub-filter error magnitudes have marginally grown. This partially justifies the realization-to-realization approach.

Second, the sub-filter errors tend to back-scatter over time, and it was found that the characteristic error wave number decreases at a rate defined by the integral time scale τ_{int} (listed in Tab. A.1) [151, 154]. For both C1 and A2, τ_{int} is larger than the simulation time. It can be therefore expected that sub-filter error will only marginally

back-scatter during the LES simulations. Regardless of how small or localized, if the error is localized at scales that matter for the ignition process, predictions based on the initial conditions cannot be achieved. In the case of A2, it is later found that the large vortical structures affected the ignition process (Sec. 4.1.4.1). These large structures are not affected by the back-scatter of sub-filter scales errors, which explains why it is possible to identify initial conditions that lead to ignition success or failure. In the case of C1, however, it is later concluded that small scales do affect the ignition process (Sec. 4.1.4.2). Since the classification of ignition success and failure based on initial conditions is not always possible, it can be concluded that scales smaller than the LES filter size matter, at least initially. At later stages, since the ignition modes are clearly separated (Sec. 4.1.5) until the end of the simulations, the analysis is unlikely to be influenced by the accumulation of errors over time.

A.2 Number of clusters

In order to characterize the ignition success and failure mechanism of both fuels, we use the K-means clustering. At each one of the 21 time instance samples during the simulations, clustering is done. Therefore the number of clusters can vary over time.

For the initialization of the clusters, the K-means++ version of the K-means algorithm [130] is used. The algorithm picks random snapshots as initial centroids of the clusters. This random initialization creates a variance in the silhouette score obtained with a fixed number of clusters. Therefore, the number of clusters is determined by running the silhouette score 21 times for cluster numbers between 2 and 10. The number of clusters selected is the one that gives, on average, the largest silhouette score. This process is repeated for each one of the 21 time instances saved between $t = 0$ ms and $t = 3.5$ ms, and for each fuel. Therefore, the optimal number of clusters varies over time.

As mentioned in Sec. 4.1.3.3, a second method is used to determine the optimal number of clusters: the X-means method [137]. This algorithm starts with a certain number of clusters (the parent clusters) and recursively refines them in subgroups (the child cluster). The refined clustering of the parent cluster is then evaluated using a certain criterion [138]. If the refined clustering of the parent cluster is deemed more appropriate by the criterion, it is adopted. The clustering initialization is also subject to randomness. Therefore, the optimal number of clusters is also computed 21 times. For each time instance, each field, and each fuel, the average optimal number of clusters is recorded. Note that the clustering is always done with K-means, and X-means is only used to decide on the number of clusters.

The optimal number of clusters obtained for progress variable over time, for both fuels, are plotted in Fig. A.1. It can be seen that both methods do not agree on the optimal number of clusters but highlight similar trends. At early times, both methods require a larger amount of clusters than at later times. Then, two or three clusters are deemed necessary. The clustering was done with X-means and the silhouette method to decide which method was the most appropriate. The centroid obtained with the X-means did not show different physical processes, which explains why the clustering obtained with the silhouette method was used.

A.3 LDA and Sensor Example

A toy dataset is created in a 2D space by sampling two Gaussian distributions with the following means: $[1, 0]$ for the "failure" set, and $[-1, 0]$ for the "success" set. The covariance matrices for both are set to the identity matrix scaled by 0.01. As shown in Fig. A.2 (left), once sampled, the resulting dataset by construction represents two distinct "blobs" separated along the x-axis. Through this trivial example, the goal is to elucidate the meaning of the LDA vector and the sensors.

Since the data here already exists in such a low-dimensional space (2D), the POD

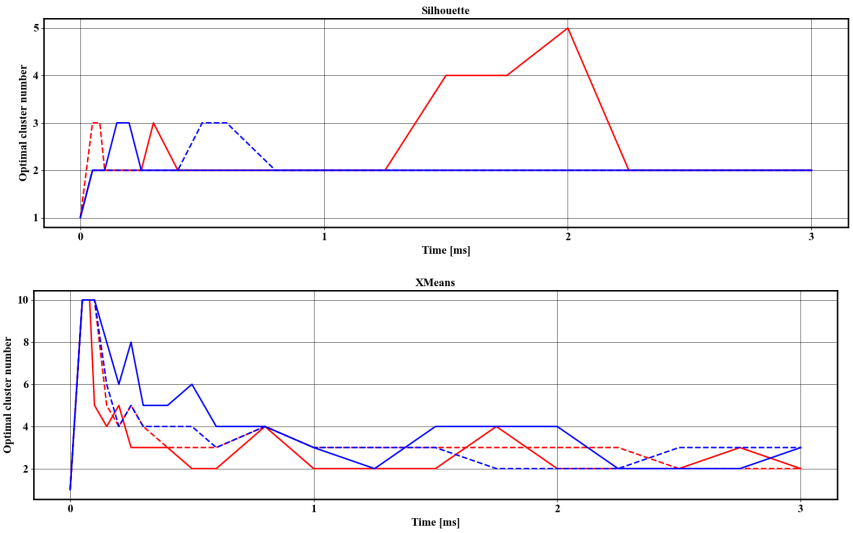

Figure A.1: Optimal number of clusters obtained at each time instance for A2 (blue) and C1 (red) for igniting (—) and failing cases (- -), using silhouette score (top), and X-means (bottom).

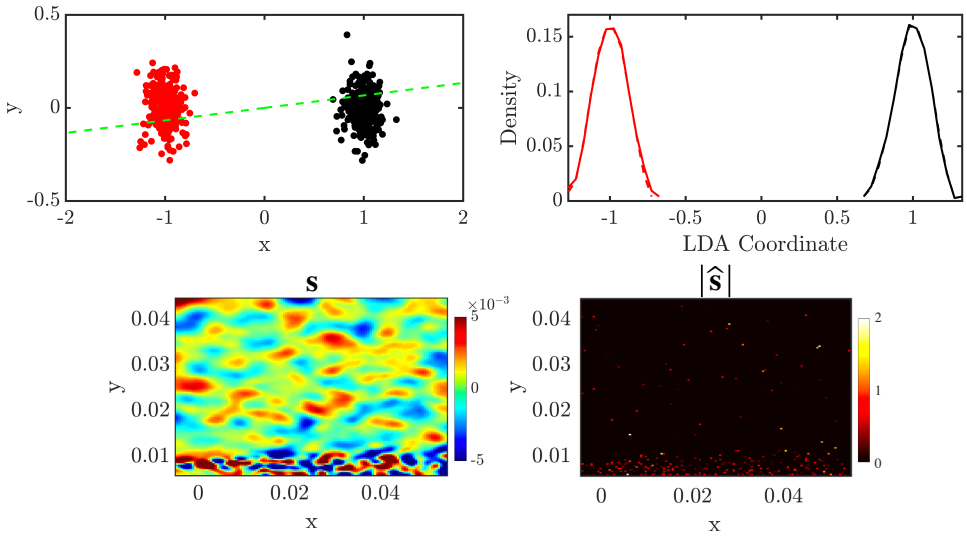

Figure A.2: Top left: toy dataset in 2D for success (black) and failure (red), with the LDA vector overlayed (dash-green). Top right: LDA densities for each class for the original data (solid lines) and sparse data (dashed lines). Bottom left: LDA vector in physical space, $\mathbf{s} = \phi\mathbf{w}$, from the Jet-A mixture fraction dataset. Bottom right: corresponding sparse sensors $\hat{\mathbf{s}}$ obtained from the optimization – the nonzero values are the sensor locations. Both images are X-Y planes obtained at the Z=0 section. As per Eq. 4.7, both $\mathbf{s}$ and $\hat{\mathbf{s}}$ produce the same vector $\mathbf{w}$ in POD space.

pre-processing step (step 2 in Fig. 4.2) is neglected (or, alternatively, the original data and the POD coefficients can be considered identical). Upon labeling the datasets in the same manner as with the LES simulations (Fig. A.2), the LDA can be carried out. The LDA vector was found to be $\mathbf{w} = [0.998, 0.067]^T$, and is also shown in Fig. A.2. As expected, most of the contribution to $\mathbf{w}$ comes along the x-axis, which is the direction that best discriminates the two classes. Through this simple example, we can see the significance of the LDA vector: it is a direction that encodes the separation between the two classes from the data given. The projection of the data onto the LDA vector is also illustrated in Fig. A.2, which shows the separation in the LDA coordinates for the two classes in the 1D LDA space.

We now proceed with recovering the sparse sensors. Recall that in Eq. 4.7, the optimization problem is defined such that the POD transformation of the sparse vector, $\phi^T\hat{\mathbf{s}}$, must reproduce the LDA vector $\mathbf{w}$, since in the actual implementation, the LDA is performed in the POD space. In this toy example, the original data space and POD space are identical, so the optimization of Eq. 4.7 is not purposeful ($\mathbf{w} = \mathbf{s}$).

Instead of running the optimization, we simply take the best sparse approximation to the already computed $\mathbf{w}$. In two dimensions, there are only two options: $[1, 0]^T$ or $[0, 1]^T$, corresponding to a single sensor in the x- or y-directions, respectively. Clearly, the ideal sensor approximation to $\mathbf{w} = [0.998, 0.067]^T$ is $\hat{\mathbf{s}} = [1, 0]^T$. Note that in this setting, we only have one sensor ($N_S = 1$), and this sensor indicates that only the first dimension (x-direction) is significant in determining the class discrimination. The dashed lines in Fig. A.2 (top right) show the LDA projection computed with the sparse data (same concept as in Fig. 4.3), where the sparse dataset was obtained by computing the element-wise product of the original dataset and $\hat{\mathbf{s}}$ – since $\hat{\mathbf{s}} = [1, 0]^T$, this amounts to considering only the x-direction and neglecting the y-direction from the original Gaussian data, and then projecting this modified "sparse" dataset onto the LDA vector $\mathbf{w}$. The densities almost exactly overlap, indicating the reliability of

the sensor approximation.

The same concept applies in higher dimensions as used in the ignition dataset, where each dimension in the M-dimensional phase space represents an (x,y,z) location in physical space. An example of an actual LDA vector obtained from the mixture fraction dataset juxtaposed with the corresponding sensors resulting from one optimization run in Eq. 4.7 is shown in Fig. A.2 (bottom). Each of these plots is analogous to the 2D toy problem counterparts. In the end, the sparse sensors can be regarded as a more interpretable proxy for the LDA vector $\mathbf{w}$.

It should be noted that in the bottom plots of Fig. 4.3, the *frequency* at which a sensor occupies a particular location in physical space is plotted. These frequencies are obtained by performing several runs of the optimization from the same dataset, as described in Sec. 4.1.3.1.

BIBLIOGRAPHY

BIBLIOGRAPHY

[1] Lefebvre, A. H. and Ballal, D. R., *Gas turbine combustion: alternative fuels and emissions*, CRC press, 2010.

[2] Mastorakos, E., "Ignition of turbulent non-premixed flames," *Progress in Energy and Combustion Science*, Vol. 35, No. 1, 2009, pp. 57–97.

[3] Sepulveda, D. and Striebel, E. E., "Starting means for a gas turbine engine," 1983, US Patent 4417439A.

[4] Neophytou, A., Richardson, E., and Mastorakos, E., "Spark ignition of turbulent recirculating non-premixed gas and spray flames: A model for predicting ignition probability," *Combustion and Flame*, Vol. 159, No. 4, 2012, pp. 1503–1522.

[5] Sforzo, B. A., *High energy spark ignition in non-premixed flowing combustors*, Ph.D. thesis, Georgia Institute of Technology, 2014.

[6] Sforzo, B., Dao, H., Wei, S., and Seitzman, J., "Liquid fuel composition effects on forced, nonpremixed ignition," *Journal of Engineering for Gas Turbines and Power*, Vol. 139, No. 3, 2017.

[7] Sau, R. and Mahesh, K., "Dynamics and mixing of vortex rings in crossflow," *Journal of fluid Mechanics*, Vol. 604, 2008, pp. 389.

[8] Rieth, M., Borghesi, G., and Chen, J. H., "DNS of Post-Discharge Plasma Ignition Evolution Relevant to High Altitude Relight." Tech. rep., Sandia National Lab., Livermore, CA, United States, 2018.

[9] Sforzo, B., Matusik, K., Kastengren, A., Powell, C., and Seitzman, J. M., "Aircraft Ignition Kernel Characterization by X-ray Radiography," *AIAA Scitech 2019 Forum*, 2019, p. 2246.

[10] Lefebvre, A. H., *Gas turbine combustion*, CRC press, 1998.

[11] Addy Jr, H. E. and Veres, J. P., "An overview of NASA engine ice-crystal icing research," *SAE Technical Paper*, SAE International, 2011.

[12] Wagner, T. C., O'Brien, W. F., Northam, G. B., and Eggers, J. M., "Plasma torch igniter for scramjets," *Journal of Propulsion and Power*, Vol. 5, No. 5, 1989, pp. 548–554.

[13] Repas, G. A., *Hydrogen-oxygen torch ignitor*, National Aeronautics and Space Administration, 1994.

[14] Saintsbury, J., "A Glow Plug Ignition System for the Gas Turbine," *SAE Technical Paper*, SAE International, 1967.

[15] Furuhama, S. and Fukuma, T., "High output power hydrogen engine with high pressure fuel injection, hot surface ignition and turbocharging," *International journal of hydrogen energy*, Vol. 11, No. 6, 1986, pp. 399–407.

[16] Colwell, J. D. and Reza, A., "Hot surface ignition of automotive and aviation fluids," *Fire Technology*, Vol. 41, No. 2, 2005, pp. 105–123.

[17] Boston, P., Bradley, D., Lung, F.-K., Vince, I., and Weinberg, F., "Flame initiation in lean, quiescent and turbulent mixtures with various igniters," *Symposium (International) on Combustion*, Vol. 20, Elsevier, 1985, pp. 141–149.

[18] Orrin, J., Vince, I., and Weinberg, F., "A study of plasma jet ignition mechanisms," *Symposium (International) on combustion*, Vol. 18, Elsevier, 1981, pp. 1755–1765.

[19] Maly, R. and Vogel, M., "Initiation and propagation of flame fronts in lean CH4-air mixtures by the three modes of the ignition spark," *Symposium (international) on combustion*, Vol. 17, Elsevier, 1979, pp. 821–831.

[20] Zhao, F., Asmus, T. N., Assanis, D. N., Dec, J. E., Eng, J. A., and Najt, P. M., "Homogeneous charge compression ignition (HCCI) engines," *SAE Technical Paper*, SAE International, 2003.

[21] Lewis, B. and Von Elbe, G., *Combustion, flames and explosions of gases*, Elsevier, 2012.

[22] Ballal, D. R. and Lefebvre, A. H., "The influence of flow parameters on minimum ignition energy and quenching distance," *Symposium (International) on Combustion*, Vol. 15, Elsevier, 1975, pp. 1473–1481.

[23] Ballal, D. and Lefebvre, A., "The influence of spark discharge characteristics on minimum ignition energy in flowing gases," *Combustion and Flame*, Vol. 24, 1975, pp. 99–108.

[24] Ko, Y., Anderson, R., and Arpaci, V. S., "Spark ignition of propane-air mixtures near the minimum ignition energy: Part I. An experimental study," *Combustion and flame*, Vol. 83, No. 1-2, 1991, pp. 75–87.

[25] Ko, Y., Arpaci, V. S., and Anderson, R., "Spark ignition of propane-air mixtures near the minimum ignition energy: Part II. A model development," *Combustion and flame*, Vol. 83, No. 1-2, 1991, pp. 88–105.

[26] Boudier, P., Henriot, S., Poinsot, T., and Baritaud, T., "A model for turbulent flame ignition and propagation in spark ignition engines," *Symposium (International) on Combustion*, Vol. 24, Elsevier, 1992, pp. 503–510.

[27] Boileau, M., Staffelbach, G., Cuenot, B., Poinsot, T., and Bérat, C., "LES of an ignition sequence in a gas turbine engine," *Combustion and Flame*, Vol. 154, No. 1-2, 2008, pp. 2–22.

[28] Tanov, S., Collin, R., Johansson, B., and Tuner, M., "Combustion stratification with partially premixed combustion, PPC, using NVO and split injection in a LD-diesel engine," *SAE international journal of engines*, Vol. 7, No. 4, 2014, pp. 1911–1919.

[29] Ruetsch, G., Vervisch, L., and Liñán, A., "Effects of heat release on triple flames," *Physics of Fluids*, Vol. 7, No. 6, 1995, pp. 1447–1454.

[30] Buckmaster, J., "Edge-flames," *Progress in Energy and Combustion Science*, Vol. 28, No. 5, 2002, pp. 435–475.

[31] West, H., "Development of High Energy Igniters for Gas Turbine Engines," *SAE Technical Paper*, SAE International, 1963.

[32] Read, R., Rogerson, J., and Hochgreb, S., "Flame imaging of gas-turbine relight," *AIAA journal*, Vol. 48, No. 9, 2010, pp. 1916–1927.

[33] Colket, M., Heyne, J., Rumizen, M., Gupta, M., Edwards, T., Roquemore, W. M., Andac, G., Boehm, R., Lovett, J., Williams, R., et al., "Overview of the national jet fuels combustion program," *AiAA Journal*, Vol. 55, No. 4, 2017, pp. 1087–1104.

[34] Opacich, K. C., Heyne, J. S., Peiffer, E., and Stouffer, S. D., "Analyzing the relative impact of spray and volatile fuel properties on gas turbine combustor ignition in multiple rig geometries," *AIAA Scitech 2019 Forum*, 2019, p. 1434.

[35] Tang, Y., Hassanaly, M., Raman, V., Sforzo, B., and Seitzman, J., "Probabilistic modeling of forced ignition of alternative jet fuels," *Proceedings of the Combustion Institute*, 2020.

[36] Wei, S., Sforzo, B., and Seitzman, J., "Fuel composition effects on forced ignition of liquid fuel sprays," *Turbo Expo: Power for Land, Sea, and Air*, Vol. 51067, American Society of Mechanical Engineers, 2018, pp. GT2018–77196.

[37] Maly, R., "Spark ignition: its physics and effect on the internal combustion engine," *Fuel economy*, Springer, 1984, pp. 91–148.

[38] Toulson, E., Schock, H. J., and Attard, W. P., "A review of pre-chamber initiated jet ignition combustion systems," *SAE Technical Paper*, SAE International, 2010.

[39] Morsy, M. H., "Review and recent developments of laser ignition for internal combustion engines applications," *Renewable and Sustainable Energy Reviews*, Vol. 16, No. 7, 2012, pp. 4849–4875.

[40] Reitz, R. D. and Duraisamy, G., "Review of high efficiency and clean reactivity controlled compression ignition (RCCI) combustion in internal combustion engines," *Progress in Energy and Combustion Science*, Vol. 46, 2015, pp. 12–71.

[41] Weinberg, F., Hom, K., Oppenheim, A., and Teichman, K., "Ignition by plasma jet," *Nature*, Vol. 272, No. 5651, 1978, pp. 341–343.

[42] Topham, D., Smy, P., and Clements, R., "An investigation of a coaxial spark igniter with emphasis on its practical use," *Combustion and Flame*, Vol. 25, 1975, pp. 187–195.

[43] Topham, D., Clements, R., and Smy, P., "Turbulent mixing in a pulsed plasma-jet exhaust," *Journal of Fluid Mechanics*, Vol. 148, 1984, pp. 207–224.

[44] Topham, D., Clements, R., Ridley, J., and Smy, P., "The initiation of combustion by a hot turbulent mixing element," *Combustion science and technology*, Vol. 50, No. 1-3, 1986, pp. 41–60.

[45] Pitt, P. L., Clements, R., and Topham, D., "The early phase of spark ignition," *Combustion science and technology*, Vol. 78, No. 4-6, 1991, pp. 289–314.

[46] Ahmed, S. and Mastorakos, E., "Spark ignition of lifted turbulent jet flames," *Combustion and Flame*, Vol. 146, No. 1-2, 2006, pp. 215–231.

[47] Birch, A., Brown, D., and Dodson, M., "Ignition probabilities in turbulent mixing flows," *Symposium (International) on Combustion*, Vol. 18, Elsevier, 1981, pp. 1775–1780.

[48] Smith, M., Birch, A., Brown, D., and Fairweather, M., "Studies of ignition and flame propagation in turbulent jets of natural gas, propane and a gas with a high hydrogen content," *Symposium (International) on Combustion*, Vol. 21, Elsevier, 1988, pp. 1403–1408.

[49] Ahmed, S. and Mastorakos, E., "Correlation of spark ignition with the local instantaneous mixture fraction in a turbulent nonpremixed methane jet," *Combustion science and technology*, Vol. 182, No. 9, 2010, pp. 1360–1368.

[50] Wei, S., Sforzo, B., and Seitzman, J., "High-Speed Imaging of Forced Ignition Kernels in Nonuniform Jet Fuel/Air Mixtures," *Journal of Engineering for Gas Turbines and Power*, Vol. 140, No. 7, 2018.

[51] Sforzo, B., Wei, S., and Seitzman, J. M., "Non-premixed Ignition of Alternative Jet Fuels," *55th AIAA Aerospace Sciences Meeting*, 2017, p. 0147.

[52] Raman, V. and Hassanaly, M., "Emerging trends in numerical simulations of combustion systems," *Proceedings of the Combustion Institute*, Vol. 37, No. 2, 2019, pp. 2073–2089.

[53] Pitsch, H., "Large-eddy simulation of turbulent combustion," *Annu. Rev. Fluid Mech.*, Vol. 38, 2006, pp. 453–482.

[54] Fan, L. and Reitz, R. D., "Development of an ignition and combustion model for spark-ignition engines," *SAE transactions*, 2000, pp. 1977–1989.

[55] Richard, S., Colin, O., Vermorel, O., Benkenida, A., Angelberger, C., and Veynante, D., "Towards large eddy simulation of combustion in spark ignition engines," *Proceedings of the combustion institute*, Vol. 31, No. 2, 2007, pp. 3059–3066.

[56] Tan, Z. and Reitz, R. D., "An ignition and combustion model based on the level-set method for spark ignition engine multidimensional modeling," *Combustion and flame*, Vol. 145, No. 1-2, 2006, pp. 1–15.

[57] Fan, L., Li, G., Han, Z., and Reitz, R. D., "Modeling fuel preparation and stratified combustion in a gasoline direct injection engine," *SAE transactions*, 1999, pp. 105–119.

[58] Triantafyllidis, A., Mastorakos, E., and Eggels, R., "Large Eddy Simulations of forced ignition of a non-premixed bluff-body methane flame with Conditional Moment Closure," *Combustion and Flame*, Vol. 156, No. 12, 2009, pp. 2328–2345.

[59] Subramanian, V., Domingo, P., and Vervisch, L., "Large eddy simulation of forced ignition of an annular bluff-body burner," *Combustion and Flame*, Vol. 157, No. 3, 2010, pp. 579–601.

[60] Pillai, S. V., *Numerical simulation of forced ignition using LES coupled with a tabulated detailed chemistry approach*, Ph.D. thesis, 2010.

[61] Jones, W. P. and Tyliszczak, A., "Large eddy simulation of spark ignition in a gas turbine combustor," *Flow, turbulence and combustion*, Vol. 85, No. 3-4, 2010, pp. 711–734.

[62] Bane, S. P. M., *Spark ignition: experimental and numerical investigation with application to aviation safety*, Ph.D. thesis, Citeseer, 2010.

[63] Richardson, E. and Mastorakos, E., "Numerical investigation of forced ignition in laminar counterflow non-premixed methane-air flames," *Combustion science and technology*, Vol. 179, No. 1-2, 2007, pp. 21–37.

[64] Weckering, J., Sadiki, A., Janicka, J., Mastorakos, E., and Eggels, R., "A forced ignition probability analysis method using LES and Lagrangian particle monitoring," *Proceedings of the Combustion Institute*, Vol. 33, No. 2, 2011, pp. 2919–2925.

[65] Esclapez, L., Riber, E., and Cuenot, B., "Ignition probability of a partially premixed burner using LES," *Proceedings of the Combustion Institute*, Vol. 35, No. 3, 2015, pp. 3133–3141.

[66] Capecelatro, J., Bodony, D. J., and Freund, J., "Adjoint-based sensitivity analysis of ignition in a turbulent reactive shear layer," *55th AIAA Aerospace Sciences Meeting*, 2017, p. 0846.

[67] Lacaze, G., Richardson, E., and Poinsot, T., "Large eddy simulation of spark ignition in a turbulent methane jet," *Combustion and Flame*, Vol. 156, No. 10, 2009, pp. 1993–2009.

[68] Eyssartier, A., Cuenot, B., Gicquel, L. Y., and Poinsot, T., "Using LES to predict ignition sequences and ignition probability of turbulent two-phase flames," *Combustion and Flame*, Vol. 160, No. 7, 2013, pp. 1191–1207.

[69] Richardson, E. S., *Ignition modelling for turbulent non-premixed flows*, Ph.D. thesis, University of Cambridge, 2007.

[70] Esclapez, L., *Numerical study of ignition and inter-sector flame propagation in gas turbine*, Ph.D. thesis, Institut National Polytechnique de Toulouse, 2015.

[71] de Oliveira, P. M., Sitte, M. P., and Mastorakos, E., "Polydispersity Effects in Low-order Ignition Modeling of Jet Fuel Sprays," *Combustion Science and Technology*, 2019, pp. 1–14.

[72] Ivancic, P., Luke, E., Hassan, E. A., Ombrello, T., and Peterson, D. M., "Predicting Ignition Probability Using a Backwards-Time Integration Scheme," *AIAA Scitech 2020 Forum*, 2020, p. 0649.

[73] Sforzo, B. and Seitzman, J., "Modeling ignition probability for stratified flows," *Journal of Propulsion and Power*, Vol. 33, No. 5, 2017, pp. 1294–1304.

[74] Luong, M. B., Pérez, F. E. H., and Im, H. G., "Prediction of ignition modes of NTC-fuel/air mixtures with temperature and concentration fluctuations," *Combustion and Flame*, Vol. 213, 2020, pp. 382–393.

[75] Bilger, R., Stårner, S., and Kee, R., "On reduced mechanisms for methane air combustion in nonpremixed flames," *Combustion and Flame*, Vol. 80, No. 2, 1990, pp. 135–149.

[76] Pera, C., Colin, O., and Jay, S., "Development of a FPI detailed chemistry tabulation methodology for internal combustion engines," *Oil & Gas Science and Technology-Revue de l'IFP*, Vol. 64, No. 3, 2009, pp. 243–258.

[77] Goodwin, D. G., Moffat, H. K., and Speth, R. L., "Cantera: An Object-oriented Software Toolkit for Chemical Kinetics, Thermodynamics, and Transport Processes," 2017, Version 2.3.0.

[78] D PIERCE, C. and Moin, P., "Progress-variable approach for large-eddy simulation of non-premixed turbulent combustion," *Journal of fluid Mechanics*, Vol. 504, 2004, pp. 73.

[79] Van Oijen, J., Donini, A., Bastiaans, R., ten Thije Boonkkamp, J., and De Goey, L., "State-of-the-art in premixed combustion modeling using flamelet generated manifolds," *Progress in Energy and Combustion Science*, Vol. 57, 2016, pp. 30–74.

[80] Pierce, C. D. and Moin, P., *Progress-variable approach for large-eddy simulation of turbulent combustion*, Ph.D. thesis, Citeseer, 2001.

[81] Ihme, M. and Pitsch, H., "Modeling of radiation and nitric oxide formation in turbulent nonpremixed flames using a flamelet/progress variable formulation," *Physics of Fluids*, Vol. 20, No. 5, 2008, pp. 055110.

[82] Mueller, M. E., *Large eddy simulation of soot evolution in turbulent reacting flows*, Ph.D. thesis, Stanford University, 2012.

[83] Fiorina, B., Baron, R., Gicquel, O., Thevenin, D., Carpentier, S., Darabiha, N., et al., "Modelling non-adiabatic partially premixed flames using flame-prolongation of ILDM," *Combustion Theory and Modelling*, Vol. 7, No. 3, 2003, pp. 449–470.

[84] Nunno, A. C., Grenga, T., and Mueller, M. E., "Comparative analysis of methods for heat losses in turbulent premixed flames using physically-derived reduced-order manifolds," *Combustion Theory and Modelling*, Vol. 23, No. 1, 2019, pp. 42–66.

[85] Darabiha, N. and Candel, S., "The influence of the temperature on extinction and ignition limits of strained hydrogen-air diffusion flames," *Combustion science and technology*, Vol. 86, No. 1-6, 1992, pp. 67–85.

[86] LIBBY, P. A. and WILLiAMS, F. A., "Strained premixed laminar flames under nonadiabatic conditions," *Combustion science and technology*, Vol. 31, No. 1-2, 1983, pp. 1–42.

[87] Coriton, B., Smooke, M. D., and Gomez, A., "Effect of the composition of the hot product stream in the quasi-steady extinction of strained premixed flames," *Combustion and flame*, Vol. 157, No. 11, 2010, pp. 2155–2164.

[88] Tang, Y. and Raman, V., "LES flamelet approach for non-adiabatic, strained premixed combustion," *Combustion and Flame (Submitted)*, 2021.

[89] Germano, M., "Turbulence: the filtering approach," *Journal of Fluid Mechanics*, Vol. 238, 1992, pp. 325–336.

[90] Pierce, C. D. and Moin, P., "A dynamic model for subgrid-scale variance and dissipation rate of a conserved scalar," *Physics of Fluids*, Vol. 10, No. 12, 1998, pp. 3041–3044.

[91] Branley, N. and Jones, W., "Large eddy simulation of a turbulent non-premixed flame," *Combustion and flame*, Vol. 127, No. 1-2, 2001, pp. 1914–1934.

[92] Pitsch, H., "Unsteady flamelet modeling of differential diffusion in turbulent jet diffusion flames," *Combustion and Flame*, Vol. 123, No. 3, 2000, pp. 358–374.

[93] Donini, A., Bastiaans, R., van Oijen, J., and De Goey, L., "Differential diffusion effects inclusion with flamelet generated manifold for the modeling of stratified premixed cooled flames," *Proceedings of the Combustion Institute*, Vol. 35, No. 1, 2015, pp. 831–837.

[94] Wang, K., Xu, R., Parise, T., Shao, J., Movaghar, A., Lee, D. J., Park, J.-W., Gao, Y., Lu, T., Egolfopoulos, F. N., et al., "A physics-based approach to modeling real-fuel combustion chemistry–IV. HyChem modeling of combustion kinetics of a bio-derived jet fuel and its blends with a conventional Jet A," *Combustion and Flame*, Vol. 198, 2018, pp. 477–489.

[95] Mueller, M. E. and Pitsch, H., "LES model for sooting turbulent nonpremixed flames," *Combustion and flame*, Vol. 159, No. 6, 2012, pp. 2166–2180.

[96] Rodrigues, P., Franzelli, B., Vicquelin, R., Gicquel, O., and Darabiha, N., "Coupling an LES approach and a soot sectional model for the study of sooting turbulent non-premixed flames," *Combustion and Flame*, Vol. 190, 2018, pp. 477–499.

[97] Mercier, R., Auzillon, P., Moureau, V., Darabiha, N., Gicquel, O., Veynante, D., and Fiorina, B., "LES modeling of the Impact of Heat Losses and Differential Diffusion on Turbulent Stratified Flame Propagation: Application to the TU Darmstadt Stratified Flame," *Flow, turbulence and combustion*, Vol. 93, No. 2, 2014, pp. 349–381.

[98] Hassanaly, M., Koo, H., Lietz, C. F., Chong, S. T., and Raman, V., "A minimally-dissipative low-Mach number solver for complex reacting flows in OpenFOAM," *Computers & Fluids*, Vol. 162, 2018, pp. 11–25.

[99] Issa, R. I., "Solution of the implicitly discretised fluid flow equations by operator-splitting," *Journal of computational physics*, Vol. 62, No. 1, 1986, pp. 40–65.

[100] Scarcelli, R., Zhang, A., Wallner, T., Som, S., Huang, J., Wijeyakulasuriya, S., Mao, Y., Zhu, X., and Lee, S.-Y., "Development of a Hybrid Lagrangian–Eulerian Model to Describe Spark-Ignition Processes at Engine-Like Turbulent Flow Conditions," *Journal of Engineering for Gas Turbines and Power*, Vol. 141, No. 9, 2019.

[101] Sforzo, B., Lambert, A., Kim, J., Jagoda, J., Menon, S., and Seitzman, J., "Post discharge evolution of a spark igniter kernel," *Combustion and Flame*, Vol. 162, No. 1, 2015, pp. 181–190.

[102] Jaravel, T., Labahn, J., Sforzo, B., Seitzman, J., and Ihme, M., "Numerical study of the ignition behavior of a post-discharge kernel in a turbulent stratified crossflow," *Proceedings of the Combustion Institute*, Vol. 37, No. 4, 2019, pp. 5065–5072.

[103] Najm, H. N., "Uncertainty quantification and polynomial chaos techniques in computational fluid dynamics," *Annual review of fluid mechanics*, Vol. 41, 2009, pp. 35–52.

[104] Braman, K., Oliver, T. A., and Raman, V., "Bayesian analysis of syngas chemistry models," *Combustion Theory and Modelling*, Vol. 17, No. 5, 2013, pp. 858–887.

[105] Constantin, P., Foias, C., Manley, O. P., and Temam, R., "Determining modes and fractal dimension of turbulent flows," *Journal of Fluid Mechanics*, Vol. 150, 1985, pp. 427–440.

[106] Hassanaly, M. and Raman, V., "Ensemble-LES analysis of perturbation response of turbulent partially-premixed flames," *Proceedings of the Combustion Institute*, Vol. 37, No. 2, 2019, pp. 2249–2257.

[107] Krengel, U., *Ergodic theorems*, Vol. 6, Walter de Gruyter, 2011.

[108] Ghanem, R. G. and Spanos, P. D., "Stochastic finite element method: Response statistics," *Stochastic finite elements: a spectral approach*, Springer, 1991, pp. 101–119.

[109] Hosder, S., Walters, R., and Perez, R., "A non-intrusive polynomial chaos method for uncertainty propagation in CFD simulations," *44th AIAA aerospace sciences meeting and exhibit*, 2006, p. 891.

[110] Nagy, Z. and Braatz, R. D., "Distributional uncertainty analysis using power series and polynomial chaos expansions," *Journal of Process Control*, Vol. 17, No. 3, 2007, pp. 229–240.

[111] Hosder, S., Walters, R., and Balch, M., "Efficient sampling for non-intrusive polynomial chaos applications with multiple uncertain input variables," *48th AIAA/ASME/ASCE/AHS/ASC Structures, Structural Dynamics, and Materials Conference*, 2007, p. 1939.

[112] Cooper, M., Wu, W., and Mccue, L., "Non-intrusive polynomial chaos for efficient uncertainty analysis in parametric roll simulations," *Journal of Marine Science and Technology*, Vol. 21, No. 2, 2016, pp. 282–296.

[113] Hosder, S., Walters, R. W., and Balch, M., "Point-collocation nonintrusive polynomial chaos method for stochastic computational fluid dynamics," *AIAA journal*, Vol. 48, No. 12, 2010, pp. 2721–2730.

[114] Tang, Y., Hassanaly, M., Raman, V., Sforzo, B., and Seitzman, J., "A comprehensive modeling procedure for estimating statistical properties of forced ignition," *Combustion and Flame*, Vol. 206, 2019, pp. 158–176.

[115] Tang, Y., Hassanaly, M., Raman, V., Sforzo, B. A., Wei, S., and Seitzman, J. M., "Simulation of gas turbine ignition using Large eddy simulation approach," *Turbo Expo: Power for Land, Sea, and Air*, Vol. 51067, American Society of Mechanical Engineers, 2018, pp. GT2018–76216.

[116] Tang, Y., Hassanaly, M., Raman, V., Sforzo, B., and Seitzman, J. M., "Numerical simulation of forced ignition of Jet-fuel/air using large eddy simulation (LES) and a tabulation-based ignition," *AIAA Scitech 2019 Forum*, 2019, p. 2242.

[117] Smith, G. P., Golden, D. M., Frenklach, M., Moriarty, N. W., Eiteneer, B., Goldenberg, M., Bowman, C. T., Hanson, R. K., Song, S., Gardiner Jr, W. C., et al., "GRI 3.0 Mechanism," *Gas Research Institute (http://www. me. berkeley. edu/gri_mech)*, 1999.

[118] Wang, H., Xu, R., Wang, K., Bowman, C. T., Hanson, R. K., Davidson, D. F., Brezinsky, K., and Egolfopoulos, F. N., "A physics-based approach to modeling real-fuel combustion chemistry-I. Evidence from experiments, and thermodynamic, chemical kinetic and statistical considerations," *Combustion and Flame*, Vol. 193, 2018, pp. 502–519.

[119] Xu, R., Wang, K., Banerjee, S., Shao, J., Parise, T., Zhu, Y., Wang, S., Movaghar, A., Lee, D. J., Zhao, R., et al., "A physics-based approach to modeling real-fuel combustion chemistry–II. Reaction kinetic models of jet and rocket fuels," *Combustion and Flame*, Vol. 193, 2018, pp. 520–537.

[120] Wang, K., Xu, R., Parise, T., Shao, J., Movaghar, A., Lee, D. J., Park, J.-W., Gao, Y., Lu, T., Egolfopoulos, F. N., et al., "A physics-based approach to modeling real-fuel combustion chemistry–IV. HyChem modeling of combustion kinetics of a bio-derived jet fuel and its blends with a conventional Jet A," *Combustion and Flame*, Vol. 198, 2018, pp. 477–489.

[121] Gao, Y. and Lu, T., "Reduced HyChem models for jet fuel combustion," *10th US National Combustion Meeting*, 2017, pp. 23–26.

[122] Hassanaly, M., Tang, Y., Barwey, S., and Raman, V., "Data-driven Analysis of Relight variability of Jet Fuels induced by Turbulence," *Combustion and Flame*, Vol. 225, 2021, pp. 453–467.

[123] Langford, J. A. and Moser, R. D., "Optimal LES formulations for isotropic turbulence," *Journal of Fluid Mechanics*, Vol. 398, 1999, pp. 321.

[124] Brunton, B. W., Brunton, S. L., Proctor, J. L., and Kutz, J. N., "Sparse sensor placement optimization for classification," *SIAM Journal on Applied Mathematics*, Vol. 76, No. 5, 2016, pp. 2099–2122.

[125] Bai, Z., Brunton, S. L., Brunton, B. W., Kutz, J. N., Kaiser, E., Spohn, A., and Noack, B. R., "Data-driven methods in fluid dynamics: Sparse classification from experimental data," *Whither Turbulence and Big Data in the 21st Century*, Springer, 2017, pp. 323–342.

[126] Sirovich, L., "Turbulence and the dynamics of coherent structures. I. Coherent structures," *Quarterly of appl. math.*, Vol. 45, No. 3, 1987, pp. 561–571.

[127] Izenman, A. J., "Multivariate regression," *Modern Multivariate Statistical Techniques*, Springer, 2013, pp. 159–194.

[128] Roth, V. and Steinhage, V., "Nonlinear discriminant analysis using kernel functions," *Advances in neural information processing systems*, 2000, pp. 568–574.

[129] Lorensen, W. E. and Cline, H. E., "Marching cubes: A high resolution 3D surface construction algorithm," *ACM siggraph computer graphics*, Vol. 21, No. 4, 1987, pp. 163–169.

[130] Arthur, D. and Vassilvitskii, S., "k-means++: The advantages of careful seeding," *Proceedings of the 18th Annual ACM-SIAM Symposium on Discrete Algorithms*, SIAM, 2007, pp. 1027–1035.

[131] Steinley, D., "K-means clustering: a half-century synthesis," *British Journal of Mathematical and Statistical Psychology*, Vol. 59, No. 1, 2006, pp. 1–34.

[132] Barwey, S., Hassanaly, M., An, Q., Raman, V., and Steinberg, A., "Experimental data-based reduced-order model for analysis and prediction of flame transition in gas turbine combustors," *Combustion Theory and Modelling*, 2019, pp. 1–27.

[133] Barwey, S., Ganesh, H., Hassanaly, M., Raman, V., and Ceccio, S., "Data-based analysis of multimodal partial cavity shedding dynamics," *Experiments in Fluids*, Vol. 61, No. 4, 2020, pp. 1–21.

[134] Kaiser, E., Noack, B. R., Cordier, L., Spohn, A., Segond, M., Abel, M., Daviller, G., Östh, J., Krajnović, S., and Niven, R. K., "Cluster-based reduced-order modelling of a mixing layer," *Journal of Fluid Mechanics*, Vol. 754, 2014, pp. 365–414.

[135] Dare, T. P., Berger, Z. P., Meehan, M., and O'Connor, J., "Cluster-based reduced-order modeling to capture intermittent dynamics of interacting wakes," *AIAA journal*, 2019, pp. 2819–2827.

[136] Rousseeuw, P. J., "Silhouettes: a graphical aid to the interpretation and validation of cluster analysis," *Journal of computational and applied mathematics*, Vol. 20, 1987, pp. 53–65.

[137] Pelleg, D., Moore, A. W., et al., "X-means: Extending k-means with efficient estimation of the number of clusters." *Icml*, Vol. 1, 2000, pp. 727–734.

[138] Kass, R. E. and Wasserman, L., "A reference Bayesian test for nested hypotheses and its relationship to the Schwarz criterion," *Journal of the american statistical association*, Vol. 90, No. 431, 1995, pp. 928–934.

[139] Novikov, A., "PyClustering: data mining library," *Journal of Open Source Software*, Vol. 4, No. 36, 2019, pp. 1230.

[140] Pedregosa, F., Varoquaux, G., Gramfort, A., Michel, V., Thirion, B., Grisel, O., Blondel, M., Prettenhofer, P., Weiss, R., Dubourg, V., Vanderplas, J., Passos, A., Cournapeau, D., Brucher, M., Perrot, M., and Duchesnay, E., "Scikit-learn: Machine Learning in Python ," *Journal of Machine Learning Research*, Vol. 12, 2011, pp. 2825–2830.

[141] Zhang, R., Isola, P., Efros, A. A., Shechtman, E., and Wang, O., "The unreasonable effectiveness of deep features as a perceptual metric," *Proceedings of the IEEE Conference on Computer Vision and Pattern Recognition*, 2018, pp. 586–595.

[142] Barré, D., Esclapez, L., Cordier, M., Riber, E., Cuenot, B., Staffelbach, G., Renou, B., Vandel, A., Gicquel, L. Y., and Cabot, G., "Flame propagation in aeronautical swirled multi-burners: Experimental and numerical investigation," *Combustion and Flame*, Vol. 161, No. 9, 2014, pp. 2387–2405.

[143] Yoo, C. S., Lu, T., Chen, J. H., and Law, C. K., "Direct numerical simulations of ignition of a lean n-heptane/air mixture with temperature inhomogeneities at constant volume: Parametric study," *Combustion and Flame*, Vol. 158, No. 9, 2011, pp. 1727–1741.

[144] Chakraborty, N., Mastorakos, E., and Cant, R., "Effects of turbulence on spark ignition in inhomogeneous mixtures: a direct numerical simulation (DNS) study," *Combustion Science and Technology*, Vol. 179, No. 1-2, 2007, pp. 293–317.

[145] Als-Nielsen, J. and McMorrow, D., *Elements of modern X-ray physics*, John Wiley & Sons, 2011.

[146] Richards, K., Senecal, P., and Pomraning, E., "CONVERGE (Version 2.4.0), Convergent Science," *Inc., Madison, WI*, 2018.

[147] Van Leer, B., "Towards the ultimate conservative difference scheme. V. A second-order sequel to Godunov's method," *Journal of computational Physics*, Vol. 32, No. 1, 1979, pp. 101–136.

[148] Pal, P., Xu, C., Kumar, G., Drennan, S. A., Rankin, B. A., and Som, S., "Large-Eddy Simulation and Chemical Explosive Mode Analysis of Non-Ideal Combustion in a Non-Premixed Rotating Detonation Engine," *AIAA Scitech 2020 Forum*, 2020, p. 2161.

[149] McBride, B. J., *NASA Glenn coefficients for calculating thermodynamic properties of individual species*, National Aeronautics and Space Administration, John H. Glenn Research Center at Lewis Field, 2002.

[150] Senoner, J.-M., García, M., Mendez, S., Staffelbach, G., Vermorel, O., and Poinsot, T., "Growth of rounding errors and repetitivity of large eddy simulations," *AIAA journal*, Vol. 46, No. 7, 2008, pp. 1773–1781.

[151] Métais, O. and Lesieur, M., "Statistical predictability of decaying turbulence," *Journal of the Atmospheric Sciences*, Vol. 43, 1986, pp. 857–870.

[152] Mohan, P., Fitzsimmons, N., and Moser, R. D., "Scaling of Lyapunov exponents in homogeneous isotropic turbulence," *Physical Review Fluids*, Vol. 2, No. 11, 2017, pp. 114606.

[153] Hassanaly, M. and Raman, V., "Lyapunov spectrum of forced homogeneous isotropic turbulent flows," *Physical Review Fluids*, Vol. 4, No. 11, 2019, pp. 114608.

[154] Leith, C. and Kraichnan, R., "Predictability of turbulent flows," *Journal of the Atmospheric Sciences*, Vol. 29, No. 6, 1972, pp. 1041–1058.